

**Ph. D. Dissertation**

**Dense Estimation of Surface Reflectance Properties  
Based on Inverse Rendering**

**TAKASHI MACHIDA**

March 17, 2005

Department of Information Systems  
Graduate School of Information Science  
Nara Institute of Science and Technology

Ph. D. Dissertation  
submitted to Graduate School of Information Science,  
Nara Institute of Science and Technology  
in partial fulfillment of the requirements for the degree of  
DOCTOR of ENGINEERING

TAKASHI MACHIDA

Thesis committee: Naokazu Yokoya, Professor  
Kunihiro Chihara, Professor  
Yoshitsugu Manabe, Associate Professor

# Dense Estimation of Surface Reflectance Properties Based on Inverse Rendering\*

TAKASHI MACHIDA

## Abstract

In computer graphics (CG), making photorealistic images using a computer is now commonplace. As a result, directors can create convincing, imaginary worlds, and designers can virtually prototype, visualize, and evaluate potential products and spaces. In order to achieve these purposes, rendering methods such as ray tracing and radiosity rendering methods have been developed. However, the rendering of more photorealistic images requires both accurate object surface reflectance parameters and object surface geometries to be obtained. Therefore, in augmented virtuality, it is important to estimate surface reflectometry and surface geometry from real objects or scenes. In particular, object surface reflectometry estimation is of primary importance because, unlike object surface geometry, which can be measured using a range finder, no device has been developed to measure the variation of object surface reflectance properties.

The present study investigates the problem of object surface reflectance estimation, which is sometimes referred to as *inverse reflectometry*, for photorealistic rendering and effective multimedia applications. A number of methods have been developed for estimating object surface reflectance properties in order to render real objects under arbitrary illumination conditions. However, it is difficult to densely estimate surface reflectance properties faithfully for complex objects with interreflections. This thesis describes three new methods for densely estimating the non-uniform surface reflectance properties of real objects constructed of convex and concave surfaces. Specifically, we use registered range and surface color texture images obtained by a laser rangefinder. The proposed methods determine the positions of light sources in order to capture color

---

\*Ph. D. Dissertation, Department of Information Systems, Graduate School of Information Science, Nara Institute of Science and Technology, March 17, 2005.

images to be used in discriminating diffuse and specular reflection components of surface reflection. The first method involves densely estimating local surface reflectance properties based on the calculation of an inverse local illumination rendering. This method is useful only for objects without surface interreflections. The second and third methods densely estimate the reflectance parameters of objects with diffuse and specular interreflections based on an inverse global illumination rendering. Experiments are conducted in order to demonstrate the usefulness and the advantages and disadvantages of the proposed methods through comparative study.

**Keywords:**

Inverse Rendering, Surface Reflectometry, Interreflections, Mixed Reality, Augmented Virtuality

# Acknowledgements

This work was completed under the supervision of Professor Naokazu Yokoya of the Graduate School of Information Science at the Nara Institute of Science and Technology and Professor Haruo Takemura of the Cybermedia Center at Osaka University.

I would especially like to thank my advisor, Professor Naokazu Yokoya, who has been a great source of support and guidance throughout my Ph.D. study. Without the continuous encouragement and advice of Professor Yokoya, I could never have completed this thesis. I would also like to thank Professor Haruo Takemura, who has also been a wonderful source of support and guidance throughout the preparation of this thesis.

I am grateful to Professor Kunihiro Chihara and Associate Professor Yoshitsugu Manabe, as members of the thesis committee, for their insightful comments on this research and for accommodating a tight thesis defense schedule.

I have also benefited greatly through being able to meet and work with a number of people during my doctoral work at the Nara Institute of Science and Technology. Associate Professor Kazumasa Yamazawa and Assistant Professors Hidehiko Iwasa (now Net Systems Inc.), Masayuki Kanbara and Tomokazu Sato of the Graduate School of Information Science at the Nara Institute of Science and Technology provided helpful comments and invaluable discussions. I would also like to acknowledge the help and support that I received from the members of the Vision and Media Computing Laboratory of the Graduate School of Information Science at the Nara Institute of Science and Technology, especially my colleagues, Mr. Soichi Ebisuno, Mr. Jun Shimamura, Mr. Hirofumi Fujii, and Mr. Koichiro Yamaguchi, for making life more pleasant and work more fun during my Ph.D. study.

Finally, I would like to acknowledge the enormous support from my family and to express my sincere thanks to my parents for their understanding and support.



# Contents

<b>Abstract</b>	<b>i</b>
<b>Acknowledgements</b>	<b>iii</b>
<b>List of Figures</b>	<b>ix</b>
<b>List of Tables</b>	<b>xiii</b>
<b>List of Symbols</b>	<b>xv</b>
<b>1 Introduction</b>	<b>1</b>
<b>2 Dense Observation of Reflection Components</b>	<b>11</b>
2.1. Introduction . . . . .	11
2.2. 3D measurement of an object . . . . .	13
2.3. Preprocessing . . . . .	15
2.4. Selection of light source positions based on the reflectance model . . .	17
2.4.1 Torrance-Sparrow model . . . . .	18
2.4.2 Measurability of light reflection . . . . .	22
2.4.3 Measurability of diffuse reflection only . . . . .	24
2.4.4 Measurability of strong specular reflection . . . . .	24
2.5. Experimental results . . . . .	26
2.6. Conclusions . . . . .	32
<b>3 Inverse Local Rendering for Dense Reflectometry Estimation</b>	<b>33</b>
3.1. Introduction . . . . .	33
3.2. Estimation of surface reflectance parameters . . . . .	34

3.2.1	Estimation of diffuse reflectance parameter . . . . .	35
3.2.2	Estimation of specular reflectance and surface roughness parameters . . . . .	36
3.3.	Experimental results . . . . .	38
3.3.1	Estimated reflectance parameters . . . . .	38
3.3.2	Rendering results with the Torrance-Sparrow model . . . . .	43
3.4.	Discussion . . . . .	44
3.5.	Conclusions . . . . .	48
<b>4</b>	<b>Inverse Radiosity for Dense Reflectometry Estimation</b>	<b>49</b>
4.1.	Introduction . . . . .	49
4.2.	Radiosity rendering method . . . . .	50
4.3.	Estimation of surface reflectance parameters considering diffuse interreflections . . . . .	54
4.3.1	Estimation of diffuse reflectance parameter based on radiosity . . . . .	54
4.3.2	Estimation of specular reflectance and surface roughness parameters based on the Torrance-Sparrow model . . . . .	56
4.4.	Experimental results . . . . .	58
4.4.1	Estimated reflectance parameters . . . . .	61
4.4.2	Rendering results using the radiosity method and the Torrance-Sparrow model . . . . .	62
4.5.	Discussion . . . . .	65
4.6.	Conclusions . . . . .	66
<b>5</b>	<b>Inverse Photon Mapping for Dense Reflectometry Estimation</b>	<b>67</b>
5.1.	Introduction . . . . .	67
5.2.	Photon mapping . . . . .	68
5.3.	Estimation of surface reflectance parameters considering both diffuse and specular interreflections . . . . .	71
5.4.	Experimental results . . . . .	75
5.4.1	Preliminary experiments . . . . .	75
5.4.2	Estimated reflectance parameters . . . . .	78
5.4.3	Rendering results obtained using the photon mapping method . . . . .	85
5.5.	Discussion . . . . .	87

5.6. Conclusions . . . . .	87
<b>6 Conclusions</b>	<b>89</b>
<b>References</b>	<b>93</b>
<b>List of Publications</b>	<b>101</b>



# List of Figures

1.1	Inverse local rendering. . . . .	3
1.2	Inverse global rendering. . . . .	5
2.1	General flow diagram of surface reflectance modeling examined herein.	12
2.2	3D-digitizer and object range and texture images. . . . .	13
2.3	Direction of the camera in the laser rangefinder. . . . .	14
2.4	Coordinate system of the Cyberware laser rangefinder. . . . .	14
2.5	Local surface fitting using possible windows. . . . .	16
2.6	Multiple possible light source positions. . . . .	18
2.7	Diffuse and Specular reflection on an object surface. . . . .	21
2.8	Detection of a self-shadow. . . . .	23
2.9	Observation of only the diffuse reflection component. . . . .	25
2.10	Observation of only the specular reflection component. . . . .	25
2.11	Four objects used in the experiment. . . . .	26
2.12	Measurability of both reflection components for Object A. . . . .	28
2.13	Measurability of both reflection components for Object B. . . . .	29
2.14	Measurability of both reflection components for Object C. . . . .	30
2.15	Measurability of both reflection components for Object D. . . . .	31
3.1	Flow diagram of inverse local rendering for surface reflectance modeling.	35
3.2	Point on the Object in multiple texture images. . . . .	36
3.3	A window for linearly interpolating undetermined pixels. . . . .	37
3.4	Estimated reflectance parameters for Object A. . . . .	39
3.5	Estimated reflectance parameters for Object B. . . . .	40
3.6	Estimated reflectance parameters for Object C. . . . .	41
3.7	Estimated reflectance parameters for Object D. . . . .	42

3.8	Rendering results for Object A with the Torrance-Sparrow model. . .	43
3.9	Rendering results for Object B with the Torrance-Sparrow model. . .	43
3.10	Rendering results for Object C with the Torrance-Sparrow model. . .	44
3.11	Rendering results for Object D with the Torrance-Sparrow model. . .	44
3.12	An object with interreflections (Object E). . . . .	45
3.13	Position of Object E in the experiment. . . . .	45
3.14	Estimated diffuse reflectance parameter in Experimental Setup 1. . . .	46
3.15	Estimated diffuse reflectance parameter in Experimental Setup 2. . . .	47
4.1	Computing the form factor between a patch and a differential area. . .	51
4.2	Hemisphere method for efficient calculation of form factor. . . . .	53
4.3	Hemicube method improving the hemisphere method. . . . .	53
4.4	Flow diagram of estimating surface reflectance properties based on in- verse radiosity rendering. . . . .	55
4.5	Calculation of radiosity. . . . .	56
4.6	Comparison with previous results for Object E with diffuse surfaces. .	59
4.7	Comparison with previous results for Object E with glossy surfaces. .	60
4.8	Difference between diffuse reflectance parameters estimated with in- verse radiosity and those estimated with the method in Chapter 3. . . .	61
4.9	Rendering results for Object A with the Torrance-Sparrow model. . .	63
4.10	Rendering results for Object B with the Torrance-Sparrow model. . .	63
4.11	Rendering results for Object C with the Torrance-Sparrow model. . .	63
4.12	Rendering results for Object D with the Torrance-Sparrow model. . .	63
4.13	Difference between rendering results based on the inverse radiosity rendering and the inverse local rendering in Chapter 3. . . . .	64
5.1	Geometrical arrangement for photon mapping rendering. . . . .	69
5.2	Rendering results of photon mapping. . . . .	70
5.3	Flow diagram for the estimation of surface reflectance properties based on inverse photon mapping. . . . .	72
5.4	Detail of reflectance estimation process based on inverse photon map- ping. . . . .	73
5.5	Comparison of the three proposed methods for Object E with diffuse surfaces. . . . .	76

5.6	Comparison of the three proposed methods for Object E with glossy surfaces. . . . .	77
5.7	Differences between real and synthetic cylindrical images for Object A.	80
5.8	Differences between real and synthetic cylindrical images for Object B.	81
5.9	Differences between real and synthetic cylindrical images for Object C.	82
5.10	Differences between real and synthetic cylindrical images for Object D.	83
5.11	Relationship between the number of iterations and difference between real and synthetic images for Objects A ~ D. . . . .	84
5.12	Rendering results for Object A ~ D under arbitrary illumination conditions. . . . .	86



# List of Tables

2.1	Specifications of the Cyberware laser rangefinder. . . . .	14
2.2	Measurability of both reflection components and the number of selected light sources for estimating the reflectance parameters of Objects A, B, C and D. . . . .	32
5.1	Comparison of computational costs of the three proposed methods. . .	78
5.2	Average and variance of differences between real and synthetic images.	79



# List of Symbols

$j$	: undetermined parameter.
$k$	: undetermined parameter.
$u$	: undetermined parameter.
$v$	: undetermined parameter.
$s$	: undetermined parameter.
$t$	: undetermined parameter.
$n$	: undetermined parameter.
$x$	: 3D position of an object surface.
$o$	: 3D position of an object surface.
$o_x$	: $x$ component of object surface point $o$ .
$o_y$	: $y$ component of object surface point $o$ .
$o_z$	: $z$ component of object surface point $o$ .
$r(s, t)$	: range value at (s,t) in a cylindrical image.
$S(s, t)$	: 3D position at (s,t) in a cylindrical image.
$S_s$	: gradient component of the 3D position (s,t).
$S_t$	: gradient component of the 3D position (s,t).
$r_s$	: gradient component of the cylindrical image $r(s,t)$ .
$r_t$	: gradient component of the cylindrical image $r(s,t)$ .
$\mathbf{N}$	: unit vector of a surface normal.
$n_x$	: $x$ component of unit normal vector $\mathbf{N}$ .
$n_y$	: $y$ component of unit normal vector $\mathbf{N}$ .
$n_z$	: $z$ component of unit normal vector $\mathbf{N}$ .
$\hat{r}(s, t)$	: range value at (s,t) on a quadratic surface.
$\hat{r}_s$	: gradient component of the quadratic surface $\hat{r}(s, t)$ .
$\hat{r}_t$	: gradient component of the quadratic surface $\hat{r}(s, t)$ .

$a$	:	coefficient of the quadratic surface.
$b$	:	coefficient of the quadratic surface.
$c$	:	coefficient of the quadratic surface.
$d$	:	coefficient of the quadratic surface.
$e$	:	coefficient of the quadratic surface.
$f$	:	coefficient of the quadratic surface.
$err(s,t)$	:	error function between real data and model data.
$i$	:	image intensity.
$\hat{i}$	:	image intensity.
$p$	:	index of a light source.
$q$	:	index of a light source.
$p_x$	:	$x$ coordinate of light source at $p$ .
$p_y$	:	$y$ coordinate of light source at $p$ .
$p_z$	:	$z$ coordinate of light source at $p$ .
$I_p$	:	color image obtained with light position $p$ .
$I_{p,diff}$	:	color image consists of only the diffuse reflection component with light position $p$ .
$I_{p,spec}$	:	color image consists of only the specular reflection component with light position $p$ .
$I_{p,both}$	:	color image including strong specular reflection component with light position $p$ .
$\gamma$	:	number of pixels or patches.
$i_x$	:	image intensity corresponding to the surface point $x$ .
$i_{p,x}$	:	image intensity in image $I_p$ corresponding to surface point $x$ .
$D_p$	:	number of pixels that include only the diffuse reflection component with light source $p$ .
$S_p$	:	number of pixels that include only the specular reflection component with light source $p$ .
$th_1$	:	threshold used in the light selection method.
$i_{dx}$	:	diffuse reflection component of image intensity $i$ .
$i_{sx}$	:	specular reflection component of image intensity $i$ .
$i_{p,dx}$	:	image intensity in image $I_{p,diff}$ corresponding to

	surface point $x$ .
$i_{p,sx}$	: image intensity in image $I_{p,spec}$ corresponding to surface point $x$ .
$i_{p,bx}$	: image intensity in image $I_{p,both}$ corresponding to surface point $x$ .
$Y$	: strength of a light source.
$C$	: distance between a light source and an object surface point.
$P_{dx}$	: diffuse reflectance parameter at surface point $x$ .
$P_{sx}$	: specular reflectance parameter at surface point $x$ .
$\sigma_x$	: surface roughness parameter at surface point $x$ .
$\mathbf{L}_x$	: unit vector of a light source at surface point $x$ .
$\mathbf{V}_x$	: unit viewing vector at surface point $x$ .
$\mathbf{R}_x$	: unit half vector between $\mathbf{L}_x$ and $\mathbf{N}_x$ at surface point $x$ .
$\theta_{dx}$	: angle between $\mathbf{L}$ and $\mathbf{N}$ at surface point $x$ .
$\theta_{vx}$	: angle between $\mathbf{V}$ and $\mathbf{N}$ at surface point $x$ .
$\theta_{rx}$	: angle between $\mathbf{V}$ and $\mathbf{R}$ at surface point $x$ .
$M$	: number of possible light positions.
$m$	: number of selected light positions.
$T_{diff}$	: pixel containing only the diffuse reflection component.
$T_{spec}$	: pixel containing the strong specular reflection component.
$T_{none}$	: pixel classified as neither $T_{diff}$ nor $T_{spec}$ .
$\mathbf{L}_{px}$	: unit light source vector at surface point $x$ in image $I_p$ .
$\mathbf{R}_{px}$	: unit half vector between $\mathbf{L}_{px}$ and $\mathbf{N}_{px}$ at surface point $x$ in image $I_p$ .
$\theta_{th1}$	: threshold angle between $\mathbf{V}_x$ and $\mathbf{R}_{px}$ .
$\theta_{th2}$	: threshold angle between $\mathbf{V}_x$ and $\mathbf{R}_{px}$ .
$W$	: window size for linear interpolation.
$B_u$	: radiosity of patch $u$ .
$E_u$	: heat rate at which light is emitted from patch $u$ .
$P_{du}$	: diffuse reflectance parameter of patch $u$ .
$A_u$	: area of patch $u$ .
$F_{uv}$	: form factor between patch $u$ and patch $v$ .
$\vec{\omega}$	: direction of outgoing radiance.

$\vec{\omega}'$	: direction of incoming radiance.
$d\vec{\omega}$	: differential solid angle.
$\Omega$	: hemisphere of directions.
$L(x, \vec{\omega})$	: radiance at surface point $x$ in direction $\vec{\omega}$ .
$L(x, \vec{\omega}')$	: incident radiance at surface point $x$ from direction $\vec{\omega}'$ .
$L^e$	: emitted radiance.
$L^r$	: reflected radiance.
$f(x, \vec{\omega}', \vec{\omega})$	: BRDF.
$f_d$	: diffuse BRDF.
$f_s$	: specular BRDF.
$th_2$	: threshold used in the inverse photon mapping.

# Chapter 1

## Introduction

Computer graphics (CG) is being increasingly used to visualize real objects and environments. Applications for entertainment, architecture, interior design, virtual reality, and digital museums often require aspects of the real world to be rendered realistically from novel viewpoints and/or under novel illumination conditions. For example, it might be necessary to show how a room in a house would look under different lighting conditions or how a statue would look at various times of day in a different wing of a museum. Another example is the realistic rendering a film location under different lighting conditions, while adding in digital props and characters, with the expectation that the rendered results would accurately and realistically portray the desired scene. Moreover, augmented reality (AR) technologies have been developed. Augmented reality techniques require a virtualized object to be seamlessly merged into the real world [Azu97].

There are two approaches to the problem of virtualizing real objects photo-realistically. The first approach is image based rendering (IBR), which has often been used to reproduce real objects in CG. Generally, IBR methods require a large number of real images in order to represent the virtualized object under arbitrary illumination conditions and from an arbitrary viewing direction. Research in image-based modeling and rendering [Che95, DYB98, DM96, LF94, MB95, LH96, SS97] has shown that the photographs of a scene can be used together with geometry to produce realistic renderings of diffuse scenes under the original lighting conditions. However, challenges remain with respect to making modifications to such scenes. Whether the modifications involve changing the geometry or changing the lighting, the generation of a

new rendering requires re-computation of the interaction of light with the surfaces in the scene. Computing this interaction requires knowledge of the reflectance properties (diffuse, color, shininess, etc.) of each surface. Unfortunately, such reflectance property information is not directly available from the scene geometry or from photographs. Mukaigawa et al. [MMMS01] have proposed a photometric IBR in which a virtualized object is represented with a few real images. However, the use of a limited number of images causes a problem, whereby the appearance of the object is not faithfully reproduced because some parts of the object are interpolated linearly.

The second approach is *inverse rendering*. Producing a photorealistic image requires the object geometry, reflectance properties and lighting effect in a scene to be known. Several studies have been performed in the fields of computer vision and computer graphics in order to estimate various types of information from images in scene or objects. For example, for the estimation of object geometry from a sparse set of images, the photometric stereo method has been developed [BH85, Hor90, LR85, Pen82, DM03], and many approaches have been developed for estimating the lighting effect in a scene [HA93, RH01a, RH01b, RH02, SSI03]. In each of these methods, the environmental lighting condition in the scene is estimated for merging the virtual object into the real world. Recent studies have focused on scene lighting estimation based on spherical harmonics [RH01b, RH02], and the results of these studies have proven that lighting condition estimation is useful for representing virtual objects in the real world. Finally, approaches have also been proposed that can estimate object reflectance properties [MTY01b, MTY01a, MTY02]. The present study focuses on the estimation of object reflectance properties based on *inverse rendering*. This approach, which is sometimes referred to as *inverse reflectometry*, reproduces the object shape and surface reflectance properties. If the object surface reflectance properties are estimated simultaneously, then the virtualized object can be rendered appropriately under virtualized illumination conditions estimated from real environments [YDMH99, SSI99, BRG92, IS91, KC94, LL99b, LL99a, LL95, SWI97, MTY01b, MTY01a, MTY02]. Such methods employ surface reflectance models with several parameters, and the shape and color information of the object are used to estimate the reflectance parameters. The present study focuses on the estimation of object surface reflection in an *inverse rendering* framework.

Generally, when light encounters an obstacle, it is either scattered or absorbed. The

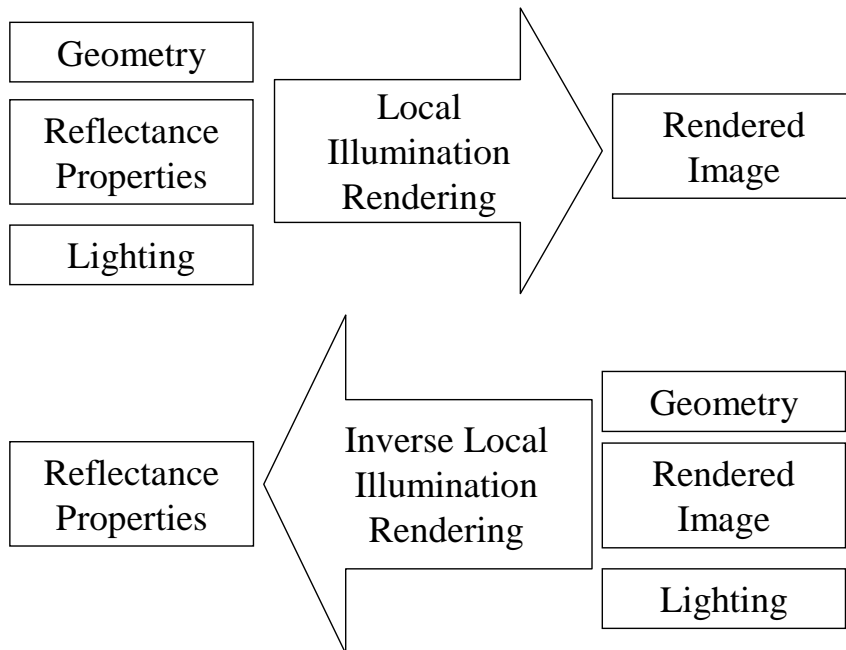


Figure 1.1. Inverse local rendering.

surface of the obstacle can be made up of different materials or media. In CG, such an effect is referred to as *local surface rendering*. Object surface reflection consists of both diffuse and specular components. The diffuse reflection component is easily observed due to the omni-directional nature of this reflection. In contrast, the specular reflection component can be observed only within a fixed range of angles with respect to viewing position, light source, and object surface normal vector. In other words, if the object geometry, object surface reflectance, light source direction, and viewing direction are known, then the object surface can be photorealistically rendered using a local illumination model. Therefore, in the case of estimating reflectance properties, if the final rendered image, object geometry, viewing direction, and light source direction are known, then the object reflectance properties can be obtained. This is referred to as *Inverse Local Rendering*(Figure 1.1).

In a number of studies [BRG92, IS91, LL95] on *Inverse Local Rendering*, objects are assumed to have a uniform reflectance property over the entire surface. Reflectance parameters are estimated using the standard least-squares method to fit a reflectance

model to a given color image. Due to the above assumption, such methods cannot be applied to objects that consist of several different materials and have non-uniform reflectance properties. On the other hand, in order to treat non-uniform surface objects, some studies have used multiple images of an object under different lighting conditions and have estimated reflectance parameters by solving simultaneous equations [KC94, LL99b, LL99a]. However, such methods still have a problem in that the results are not stable, especially when the specular reflection component is very small. Sato et al. [SWI97] developed a method by which to estimate non-uniform reflectance properties. In their method, an object was placed on a robot arm, and was then measured with a CCD camera and a rangefinder from a large number of viewpoints by rotating the robot arm. Reflectance parameters were stably acquired by decomposing the surface reflection into two components based on the singular value decomposition (SVD) technique. Although the method can be applied to objects with non-uniform reflectance properties, the shape of object should be limited because it is difficult to observe the specular reflection component over the entire surface. This is because the lighting conditions for each pose of the object with respect to the camera cannot be changed in this method.

The studies mentioned above focus on the local illumination framework which deals with only the direct illumination. In the real world, surfaces usually exhibit mutual illumination. Thus, the light that any particular surface receives may originate from not only the light sources, but also from the rest of the environment, through indirect illumination. For example, a wall in a room receives lighting effects from other walls that are illuminated by the light sources. Therefore, when object surface reflectance parameters are estimated, it is important to consider interreflections. As a result, the incident radiance of an observed surface is a complex function of the light sources, the geometry of the scene, and the undetermined reflectance properties of all of the surfaces in the scene. Therefore, the incident radiances of the surfaces must be estimated. This allows the reflectance properties of the surfaces in the scene to be estimated via an iterative optimization procedure, which allows the incident radiances to be re-estimated. This is referred to as *Inverse Global Rendering*(Figure 1.2).

In order to consider interreflections, it is important to employ a global illumination model. The physically-based simulation of all light scattering in a synthetic model is referred to as global illumination. The goal of global illumination is to simulate all of

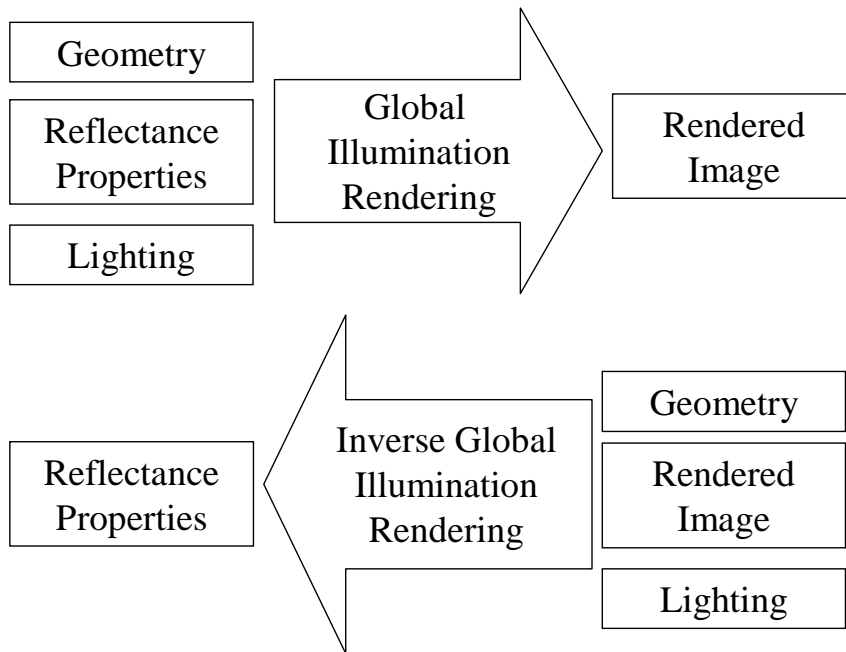


Figure 1.2. Inverse global rendering.

the reflections of light in a model and enable an accurate prediction of the intensity of the light at any point in the model. The input to a global illumination simulation is a description of the geometry and the materials, as well as the light sources. The global illumination algorithm is used to compute how light leaving the light sources interacts with the scene. Several global illumination algorithms have been developed[Kaj86, ICG86, WCG87, Jen01], most of which are based on two major techniques:

- Point sampling (ray tracing)
- Finite elements (radiosity)

In addition, hybrid techniques exist that combine radiosity and ray tracing.

The ray tracing method is a point-sampling technique that traces infinitesimal beams of light through a model. This approach can only handle mirror reflections/refractions and direct illumination. Important effects, such as depth of field, motion blur, caustics, indirect illumination, and glossy reflection cannot be computed. In order to simulate these effects, ray tracing has been extended with Monte Carlo methods[Coo86,

CPC84, Kaj86], in which rays are distributed stochastically to account for all of the light paths. However, Monte Carlo ray-tracing has a problem in that rendered images include some noise, and eliminating this noise requires a large number of sample rays[Jen95, LW95, Shi91, VG95, VG97].

On the other hand, finite element radiosity techniques are an alternative to ray-tracing methods, in which the equilibrium of the light exchange between surfaces in a model is computed. This is done by subdividing the model into small patches that can form a basis for the final light distribution. The lighting distribution is found by solving a set of linear equations for the light exchange between all of the patches. This technique can represent indirect illumination (interreflections). Recently, radiosity is extended to handle more complex reflection models[ICG86, WCG87, SAW91, SCH93, CSSD96, SSS00], but simple curved specular surfaces are still not handled properly.

The photon mapping method has also been recently developed. Photon mapping changes the representation of the illumination. Instead of tightly coupling lighting information with the geometry, the information is stored in a separate independent data structure, the *photon map*[Jen01]. The photon map is constructed from photons that are emitted from the light sources and are traced through the model. The photon map contains information about all photon hits, and this information can be used to efficiently render the model in a manner similar to that in which radiosity is used in hybrid techniques. The decoupling of the photon map from the geometry is a significant advantage that not only simplifies the representation but also makes it possible to use the structure to represent lighting in very complex models. The combination of photon mapping and a Monte Carlo ray-tracing algorithm result in an algorithm that is as general as pure Monte Carlo ray tracing, but that is significantly more efficient.

For the reflectance estimation problem, Fournier et al. [FGR93] originally developed a method for estimating surface reflectance properties using the radiosity method in an indoor scene. This method assumes uniform reflectance on an object surface and determines only the diffuse reflectance parameter. There have been a number of attempts to estimate both the diffuse and specular reflectance properties of a room [BG01, LDR00]. In these studies, however, all objects are also assumed to have uniform reflectance properties in the segmented region. Therefore, these algorithm cannot be applied to an objects that have non-uniform surface reflectance properties. Yu et al. [YDMH99] estimated the surface reflectance properties of a room from color and ge-

ometry data considering both diffuse and specular interreflections based on inverse global illumination rendering. They employed a hybrid rendering method that combines radiosity and the Monte Carlo ray tracing method. Boivin et al. [BG01] have also attempted to estimate the surface reflectance properties considering diffuse interreflections. These methods assume that the surface of interest has uniform reflectance properties. Therefore their algorithms cannot be applied to a non-uniform surface reflectance object.

The present study focuses on the estimation of non-uniform surface reflectance properties based on the *inverse rendering* framework, as mentioned previously. First, a method for estimating local surface reflectance properties is proposed. For this purpose, optimum light positions are selected in order to observe both diffuse and specular reflection on the object surfaces. By this process, both diffuse and specular components at each surface point can be decomposed. Then, the object surface reflectance properties are densely estimated based on *Inverse Local Rendering*. Specifically, the Torrance-Sparrow model, which is the most popular local object surface reflectance model and can represent physical phenomena, is employed. The proposed method can estimate the object surface reflectance parameters at each point on the object with results that are comparable to those of conventional methods[MTY01b, MTY01a, MTY02].

*Inverse Local Rendering* can estimate the object surface reflectance properties based only on the direct illumination effect. However, in the real world, objects have interreflections. Therefore, the reflectance properties must be estimated considering interreflections on the surface. In order to solve this problem, two estimation methods are proposed. One is based on the radiosity rendering method and the Torrance-Sparrow reflectance model, and the other is based on the photon mapping rendering method. The former method can estimate diffuse reflectance parameter by calculating the inverse radiosity algorithm and the specular and surface roughness parameters by calculating the inverse local reflectance model. The advantage of this method is that diffuse interreflections can be considered[MY02b, MY02a, MYT03]. In the inverse radiosity method, the influence of the specular interreflections remains. As a result, this method cannot be applied to objects that have complex geometry and specular reflection. Moreover, although the diffuse reflectance parameter can be estimated based on global illumination rendering, the specular reflectance and the surface roughness

parameter can only be estimated by local illumination rendering. Therefore, in order to address the shortcomings of the inverse radiosity estimation method, the photon mapping rendering method, which can also estimate diffuse reflectance, specular reflectance and the surface roughness parameters, was proposed. In this method, since both diffuse and specular interreflections can be considered, the inverse photon mapping method is a more efficient estimation method compared to the conventional methods. In addition, because the photon mapping rendering method has recently been implemented on graphics hardware (GPU)[PDC<sup>+</sup>03, PBMH02], real-time estimation of the object reflectance parameters is desired.

Finally, in experiments, the three proposed methods are qualitatively and quantitatively evaluated with reflectance parameter estimation and virtual relighting. These three methods are compared, and *Inverse Global Rendering* is also shown to be useful for estimating object surface reflectance properties. The radiosity method and the photon mapping method can usually be applied to a closed environment. However, the inverse radiosity and the inverse photon mapping are experimentally verified to be applicable to an open environment, in which the influence of environmental light is negligible.

The remainder of this thesis is structured as follows. Chapter 2 proposes a method for effective observation of surface reflections. As described above, the object surface reflection consists of two components: the diffuse reflection component, which is reflected by the light source omni-directionally, and the specular reflection component. The specular reflection component can be observed only at a fixed angle according to the object geometry, the light source direction, and the viewing direction. Due to their nature, the specular reflectance properties of an object are difficult to densely estimate, and thus usually require the assumption of uniform properties. In Chapter 2, the problem of *how to observe* both diffuse and specular reflection components at each surface point is described.

The latter part of this thesis discusses *how to estimate* the object surface reflectance properties. A previously obtained image, which consists of both diffuse and specular reflection components densely, is used for estimating surface reflectance properties. The object geometry is also obtained using a laser rangefinder. Basically, if the object geometry, object texture, light source direction and viewing direction are known, then the *Inverse Rendering* method can be used to find unknown surface reflectance

parameters. For this purpose, three reflectance estimation methods are proposed.

Chapter 3 proposes a method for automatically estimating object surface reflectance properties based on *Inverse Local Rendering*. The application of inverse rendering has recently become widespread. In CG, a photorealistic image is rendered using a surface reflectance model that can represent physical phenomena in the real world. In particular, color determination of object surface is calculated by *local illumination model*, which can represent the influence of direct illumination. In Chapter 3, local surface reflectance properties are estimated using the Torrance-Sparrow model as a local illumination model without the assumption of uniform surface reflectance properties. The effectiveness of this method is verified experimentally using a number of objects with non-uniform surface reflectance properties.

Chapters 4 and 5 focus on *Inverse Global Rendering*. Inverse local rendering can deal with only the influence of direct illumination. Due to this limitation, if an object has interreflections, then the estimated reflectance parameters have some errors and rendering the object photorealistically is difficult. In order to solve this problem, the global illumination model, which can represent interreflections in the real world, is employed. In Chapter 4, a radiosity rendering method is employed that can represent diffuse interreflections. Using this method, inverse radiosity rendering can be used to estimate non-uniform surface reflectance properties with interreflections. However, radiosity rendering can represent only diffuse interreflections. Due to their nature, specular interreflections cause some errors in estimated results. In Chapter 5, in order to solve the problem of the inverse radiosity rendering method, a photon mapping rendering method is employed. This rendering model can efficiently treat all influences of lighting effects in the real world. Finally, experimental results are discussed using uniform or non-uniform objects that have both diffuse and specular interreflections.

Finally, Chapter 6 presents the conclusions of primary importance obtained in this study and discusses possible subjects for future research.



# Chapter 2

## Dense Observation of Reflection Components

### 2.1. Introduction

In this chapter, the optimum light positions are selected for observing both diffuse and specular reflection components over the entire surface of an object. Because the diffuse reflection component is observed omni-directionally on the surface, it is easy to observe. On the other hand, the specular reflection component can be observed on only a certain fixed area on the object surface. Therefore, several light sources located at different positions are needed in order to observe the specular reflection component. In other words, if the specular reflection component is not observed, the specular reflectance parameters cannot be estimated. Furthermore, the greater the number of light sources used, the more images should be acquired. This results in a large computational cost. Therefore, it is important to determine the optimum light position so that both diffuse and specular reflection components are observed densely with the minimum cost.

Figure 2.1 shows a flow diagram of the light selection (A, B, C) and object surface reflectance estimation (D) processes. This chapter focuses on the light selection process. A laser rangefinder was used to obtain range and surface color images, and optimum light positions were then selected based on the object range image. The surface reflectance estimation process (D) is described in the next chapter. The light selection process consists of two processes: measurement of an object (A, C) and selection of

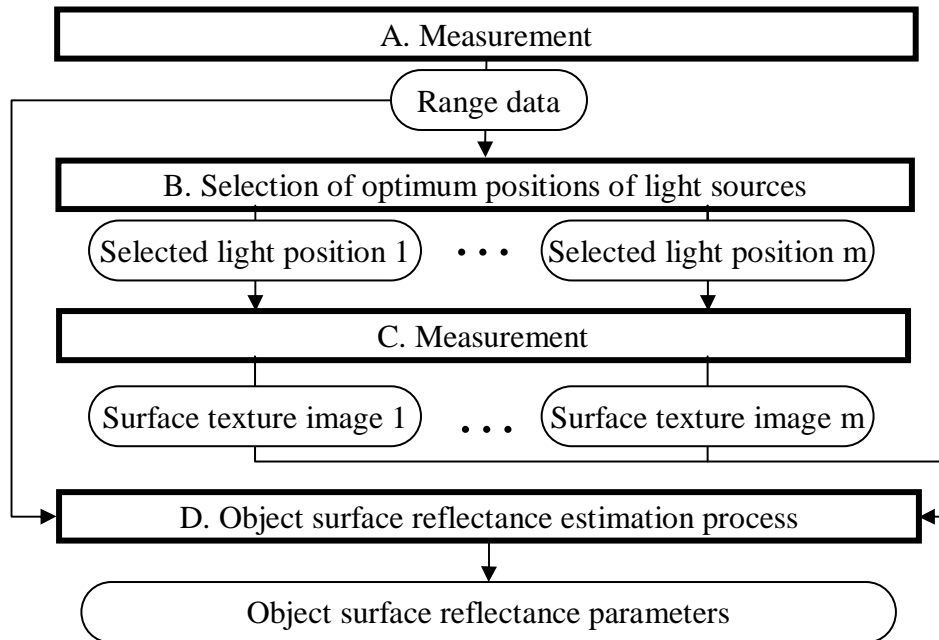


Figure 2.1. General flow diagram of surface reflectance modeling examined herein.

light sources (B). The following presents an overview of the light selection process.

1. Measurement of 3D geometry and surface texture

The object shape is acquired using a laser rangefinder in a dark room. Multiple surface texture images are also obtained under different light sources, the positions of which are selected in process (B).

2. Preprocessing

Generally, a range image acquired by laser rangefinder contains some noises, including quantization errors. Moreover, a normal vector cannot be correctly calculated in the vicinity of discontinuities. Therefore, noises are removed and quadratic surfaces are fit locally to the range image in order to acquire the normal vector correctly.

3. Selection of light source

According to the object shape and the position of the camera, multiple light

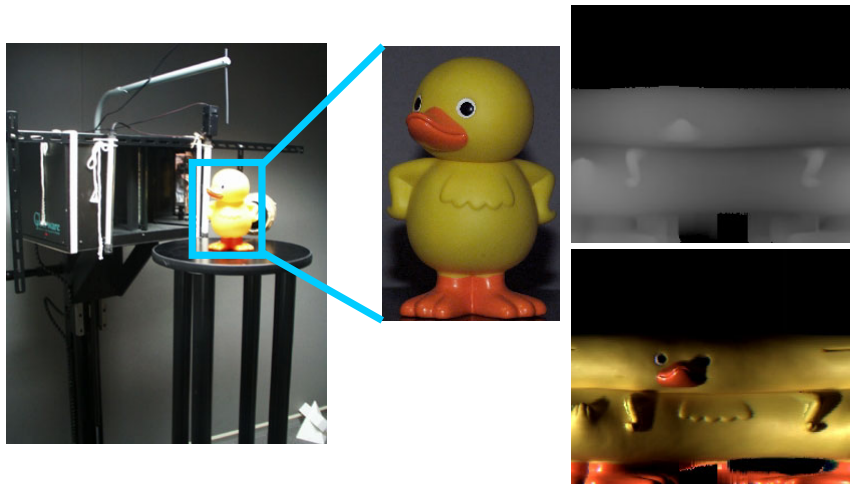


Figure 2.2. 3D-digitizer and object range and texture images.

positions are selected from among a number of possible light source positions in order to measure both diffuse and specular reflection components densely on the object surface.

The following sections describe the optimum light position selection method in detail.

## 2.2. 3D measurement of an object

A laser rangefinder (Cyberware 3030RGB) with point light sources at known positions and a camera were used to acquire range and surface color images of an object located in a dark room, as shown in Figure 2.2. This system can simultaneously obtain registered range and surface color texture images by rotating the rangefinder and the camera around the object. Figure 2.3 shows a the device as viewed from above. The camera is located at  $X1$  and a texture image is acquired through mirrors located at  $X2$  and  $X3$ . Thus, the camera is assumed to be virtually located at  $X4$ . The camera is directed toward the center of rotation.

The specifications of the rangefinder are listed in Table 2.2. The coordinates system of the texture and the range image are also shown in Figure 2.4. Here,  $R$  is the distance from the center of rotation to the object surface. The vertical axis  $h$  indicates the object height, and the horizontal axis  $\theta$  indicates the rotation angle from the original position.

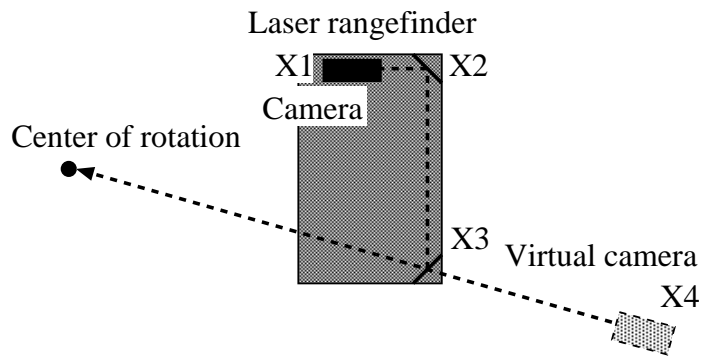


Figure 2.3. Direction of the camera in the laser rangefinder.

Table 2.1. Specifications of the Cyberware laser rangefinder.

Image size (W×H)	512×450
Vertical resolution (mm)	0.56
Horizontal resolution (degrees)	0.7
Color resolution	8-bit
Range resolution	8-bit

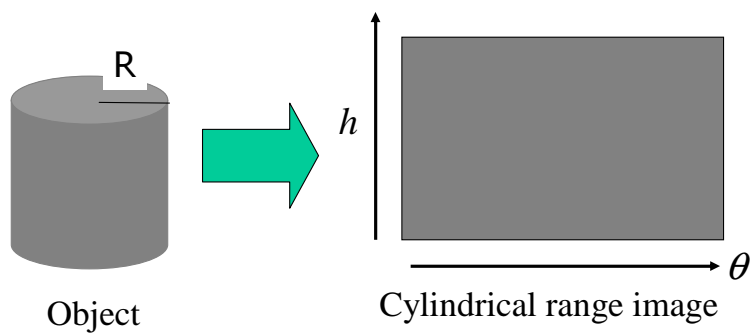


Figure 2.4. Coordinate system of the Cyberware laser rangefinder.

## 2.3. Preprocessing

Generally, the noise and quantization errors are included in the range image acquired using the laser rangefinder. Another problem is that the surface normal is not calculated accurately around the discontinuity in the range image. Therefore, an adaptive local quadratic surface fitting [YL89] is employed as a preprocessing.

First, a  $5 \times 5$  median filter is applied to the range image to remove the noise (outliers). Second, the quadratic surface is locally fitted with the range image. The range image obtained using the Cyberware laser rangefinder is expressed in cylindrical coordinates, as mentioned earlier. The 3D position  $(o_x, o_y, o_z)$  at each point of the range image is given as:

$$(o_x, o_y, o_z) = \{-r(s, t) \sin(s), -t, -r(s, t) \cos(s)\} \quad (2.1)$$

$$= \mathbf{S}(s, t), \quad (2.2)$$

where  $r$ ,  $s$ , and  $t$  are the distance from the center of rotation, the angle of rotation, and the height along the rotation axis, respectively.

The unit normal vector is given as follows:

$$\mathbf{N} = \frac{\mathbf{S}_s \times \mathbf{S}_t}{\|\mathbf{S}_s \times \mathbf{S}_t\|} \quad (2.3)$$

$$= \frac{1}{\sqrt{r_s^2 + r^2 + r^2 r_t^2}} \{-r_s \sin(s) - r \cos(s), -r_t r, -r_s \cos(s) + r \sin(s)\}, \quad (2.4)$$

where  $r_s$  and  $r_t$  are gradient components of the range image  $r(s, t)$ . This gradient is analytically computed using the following local quadratic surface fit:

$$\hat{r}(s, t) = as^2 + bt^2 + cst + ds + et + f, \quad (2.5)$$

$$\hat{r}_s = 2as + ct + d, \quad (2.6)$$

$$\hat{r}_t = 2bt + cs + e. \quad (2.7)$$

Coefficients  $a \sim f$  are determined by minimizing the following equation using the range data  $r(s, t)$  and Equation (2.5):

$$err(s, t) = \sum_{u=-2}^2 \sum_{v=-2}^2 \{r(s+u, t+v) - \hat{r}(s+u, t+v)\}^2, \quad (2.8)$$

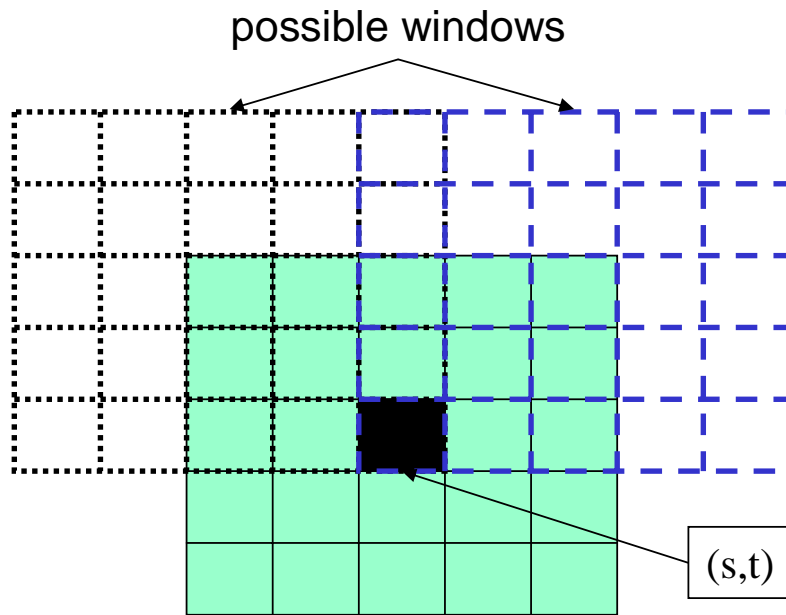


Figure 2.5. Local surface fitting using possible windows.

where  $u$  and  $v$  are local coordinates in a  $5 \times 5$  window. In the present approach, selected local quadratic surface fit is achieved using the Yokoya-Levine operator [YL89]. Using a  $5 \times 5$  window, the best window is selected from among 25 possible windows that include the point  $(s, t)$  in order to estimate the coefficients  $a \sim f$  at  $(s, t)$  (See Figure 2.5). The best window provides the minimum fitting error in Equation (2.8).

## 2.4. Selection of light source positions based on the reflectance model

Here, the problem of determining the light source positions for effectively observing both the diffuse and specular reflection components on an object surface is addressed. In the present experimental setup, multiple positions of a light source are determined among 60 possible positions prepared around the laser rangefinder. These positions are arranged two-dimensionally at 5-cm intervals, as shown in Figure 2.6. After optimum light positions are selected, a single light source is attached at the selected positions in turn so that brightness calibration among multiple lights is not needed. Note that the camera position is calibrated in advance by measuring a calibration box of known size. The position of a light source is also calibrated based on the distance from the center of rotation in global coordinates. In addition, the influence of environmental light can be ignored because the object is measured in a dark room.

Let  $I_p$  be a color image that is to be obtained with a possible light position  $p$  ( $p = 1, \dots, 60$ ) and that consists of  $\gamma$  pixels  $(i_{p1}, \dots, i_{p\gamma})$ , where  $i_{px}$  is a color intensity corresponding to the surface point  $x$ . Also, let  $D_p$  be the number of pixels that include only the diffuse reflection component in  $I_p$ , and let  $S_p$  be the number of pixels that include the strong specular reflection in  $I_p$ .

First, the following conditions are examined for each pixel in the object surface texture under each light position  $p$ :

- **Measurability of light reflection**
- **Measurability of only diffuse reflection**
- **Measurability of strong specular reflection**

Second, light positions  $p$  and  $q$  that satisfy  $D_p = \text{Max}(D_1, \dots, D_{60})$  and  $S_q = \text{Max}(S_1, \dots, S_{60})$  are selected. In the next light source position selection, a position that satisfies the same conditions is selected from among the remaining possible positions. Then,  $m$  light positions are selected to densely estimate reflectance parameters. The selection of light positions is repeated until almost all of the pixels have been observed once for the diffuse reflection component only and twice for the strong specular reflection component.

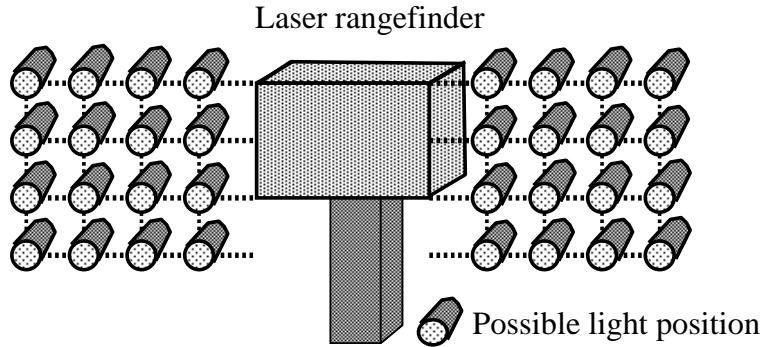


Figure 2.6. Multiple possible light source positions.

Next, the threshold  $th_1$ , i.e., the ratio of the measurability of the diffuse reflection component to that of the strong specular reflection component, is introduced as a means of determining when to stop the process of selecting light positions. With respect to determining the threshold  $th_1$ , the ratio of measurability of the specular reflection is judged at all possible positions. This ratio indicates the limit for measuring the specular reflection component. Using this threshold, the light selection process can be terminated in the case that the ratio of measurability of the specular reflection component cannot be increased further, even if the number of light source positions is increased. Thus, the reflectance parameters can be estimated efficiently for almost the entire object surface using a limited number of texture images. In the following, after presenting the surface reflection model used in the present study, the three measurability conditions mentioned above are described in detail.

### 2.4.1 Torrance-Sparrow model

Selecting the optimum light positions from among the possible light positions requires judgment as to whether a pixel in the image taken by a laser rangefinder has each reflection component. This requires a surface reflection model that represents the properties of both diffuse and specular reflection components. The reflection model describes the direction of reflection from a light source based on object geometry, viewing direction and light source direction. If these parameters are known, each pixel in the image can be judged as to whether it has both reflection components. In this chap-

ter, the Torrance-Sparrow model [TS67] is used to represent local surface reflections physically. The Torrance-Sparrow model is given as:

$$i_x = \frac{Y}{C^2} \left\{ P_{dx} \cos \theta_{dx} + \frac{P_{sx}}{\cos \theta_{vx}} \exp\left(-\frac{\theta_{rx}^2}{2\sigma_x^2}\right) \right\}, \quad (2.9)$$

$$= \frac{Y}{C^2} (i_{dx} + i_{sx}), \quad (2.10)$$

$$i_{dx} = P_{dx} \cos \theta_{dx}, \quad (2.11)$$

$$i_{sx} = \frac{P_{sx}}{\cos \theta_{vx}} \exp\left(-\frac{\theta_{rx}^2}{2\sigma_x^2}\right), \quad (2.12)$$

$$\cos \theta_{dx} = (\mathbf{N}_x \cdot \mathbf{L}_x), \quad (2.13)$$

$$\cos \theta_{vx} = (\mathbf{N}_x \cdot \mathbf{V}_x), \quad (2.14)$$

$$\theta_{rx} = \cos^{-1}(\mathbf{N}_x \cdot \mathbf{R}_x), \quad (2.15)$$

$$\mathbf{R}_x = \frac{(\mathbf{V}_x + \mathbf{L}_x)}{|\mathbf{V}_x + \mathbf{L}_x|}, \quad (2.16)$$

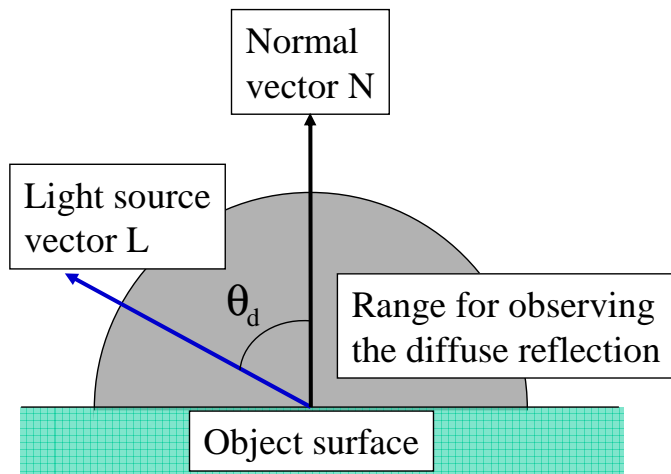
where  $i_x$  represents an observed intensity corresponding to the surface point  $x$ ,  $i_{dx}$  and  $i_{sx}$  denote the diffuse and specular reflection components, respectively,  $C$  is an attenuation coefficient related to the distance between a point light source and an object surface point, and  $Y$  represents the strength of a light source. In addition,  $P_{dx}$ ,  $P_{sx}$  and  $\sigma_x$  are the diffuse reflectance parameter, specular reflectance parameter, and surface roughness parameter, respectively, which is the standard deviation of a Gaussian distribution, respectively,  $\theta_{dx}$  is the angle between light source vector  $\mathbf{L}_x$  and surface normal vector  $\mathbf{N}_x$ ,  $\theta_{vx}$  is the angle between viewing vector  $\mathbf{V}_x$  and surface normal vector  $\mathbf{N}_x$ , and  $\theta_{rx}$  is the angle between surface normal vector  $\mathbf{N}_x$  and half vector  $\mathbf{R}_x$ . Note that half vector  $\mathbf{R}_x$  is the vector located halfway between light vector  $\mathbf{L}_x$  and viewing vector  $\mathbf{V}_x$ , and is given by Equation (2.16). All vectors are unit vectors. Figure 2.7 illustrates the geometry for this model. The angle  $\theta_{rx}$  is used to judge whether the specular reflection occurs.

In the case of using a color image,  $i_x$ ,  $i_{dx}$ ,  $i_{sx}$ ,  $P_{dx}$  and  $P_{sx}$  consist of RGB channels, and the model is applied to each channel independently. In order to estimate reflectance parameters  $P_{dx}$ ,  $P_{sx}$  and  $\sigma_x$  using this model, it is necessary to obtain the other parameters, i.e.,  $i_x$ ,  $C$ ,  $Y$ ,  $\mathbf{L}_x$ ,  $\mathbf{V}_x$  and  $\mathbf{N}_x$ , at each point on the object surface.

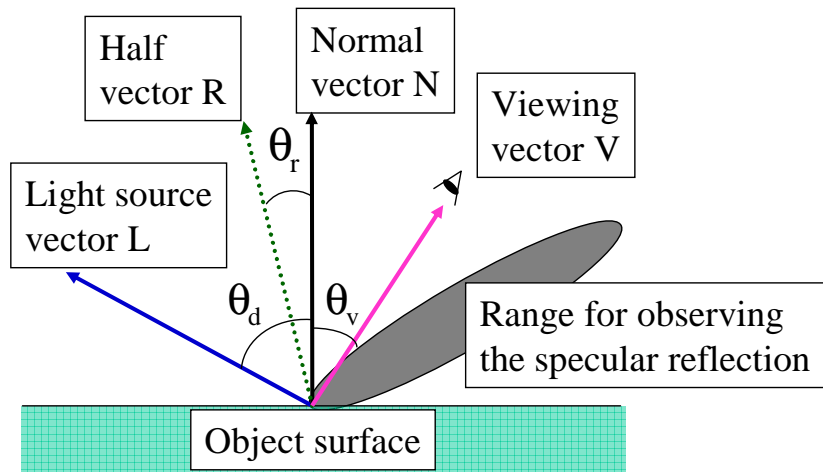
Dense and independent estimation for non-uniform surface reflectance parameters requires observation of each surface point  $x$  under at least three different lighting conditions: one lighting condition for determining the unknown parameter  $P_{dx}$ , and

the other two lighting conditions for acquiring the remaining two unknown parameters  $P_{sx}$  and  $\sigma_x$ . The selection of the optimum positions of the light source in Figure 2.1(B) is repeated until almost all of the pixels satisfy the three different lighting conditions[MTY01b]. As a result of this process, a certain number of light positions, say  $m$  (as described previously), are selected in order to densely observe both diffuse and specular reflection components.

A texture image is obtained with a selected light position  $p$  ( $p = 1, \dots, m$ ) and consists of  $\gamma$  pixels  $(i_{p1}, \dots, i_{p\gamma})$ , where  $i_{px}$  is the color intensity of surface point  $x$ .



(a) Diffuse reflection



(b) Specular reflection

Figure 2.7. Diffuse and Specular reflection on an object surface.

## 2.4.2 Measurability of light reflection

In order to measure the light reflection at a specific point  $x$  on the object surface, the surface point must be observable from the camera position and the light must illuminate the surface point. Thus, the positional relationship among the camera, the point and the light source must satisfy the following conditions.

$$(\mathbf{V}_x \cdot \mathbf{N}_x) > 0, (\mathbf{L}_{px} \cdot \mathbf{N}_x) > 0, \quad (2.17)$$

where  $\mathbf{V}_x$ ,  $\mathbf{L}_{px}$ , and  $\mathbf{N}_x$  are the viewing direction, the light source direction, and the surface normal corresponding to the surface point  $x$ , respectively. Note that the viewing direction  $\mathbf{V}_x$  and the surface normal  $\mathbf{N}_x$  are independent of the light source position  $p$ .

Even when the above equations are both satisfied, the possibility exists that a shadow is cast on the pixel. Figure 2.8 illustrates such a case. In this case, the pixel must not be used for estimating reflectance parameters. Whether a surface point  $x$  is covered by a shadow cast by light source  $p$  can be judged as follows:

Let  $(o_x, o_y, o_z)$  be the coordinates of the point  $o$  on the object surface, and let  $(p_x, p_y, p_z)$  be the coordinates of the possible light position  $p$ . Then, there exists a bounding box that is surrounded by the maximum and minimum values on each of the  $x$ ,  $y$ , and  $z$  axes of positions  $p$  and  $o$ , as shown in Figure 2.8. Here, all polygons that make up the object surface are assumed to be small enough to be covered by the bounding box. Then, determining whether or not a shadow is cast over  $o$  requires an examination to determine whether any polygon that contains a vertex inside the bounding box intersects with the line segment that connects  $o$  and  $p$ . Therefore, for all the points inside of the bounding box, the following test is performed [FvDFH93].

Let  $u$  be a point that is found to be included in the bounding box, and let  $(u_x, u_y, u_z)$  be the coordinates of this point. If  $u$  lies on a surface polygon of which the normal vector is  $(n_x, n_y, n_z)$ , then the polygon and the line segment that connects  $p$  and  $o$  are given, respectively, by the following equations:

$$\begin{cases} n_x(x - u_x) + n_y(y - u_y) + n_z(z - u_z) = 0, \\ k = \frac{x - o_x}{p_x - o_x} = \frac{y - o_y}{p_y - o_y} = \frac{z - o_z}{p_z - o_z}. \end{cases} \quad (2.18)$$

The intersection of the plane and the light segment, i.e., the point  $r$ , can be obtained

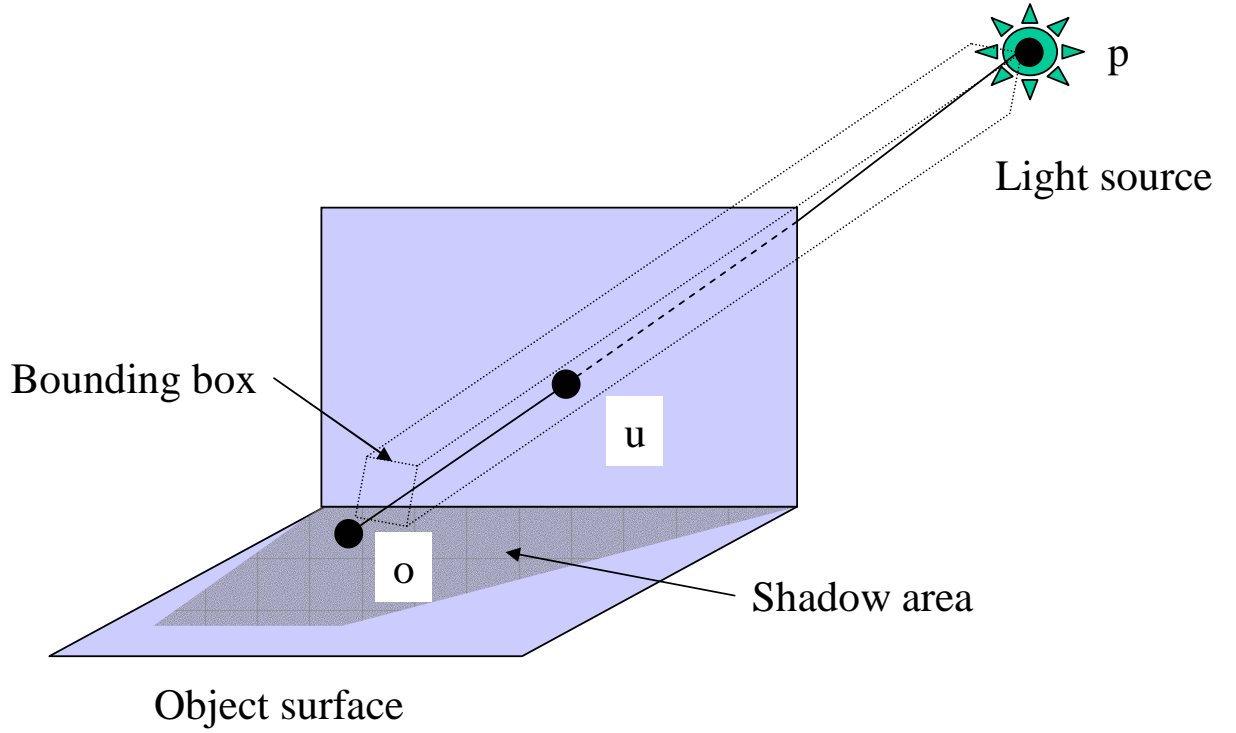


Figure 2.8. Detection of a self-shadow.

by solving Equation (2.18) for  $k$ , where  $k$  is defined as follows:

$$\begin{aligned}
 k &= \frac{n_x(u_x - v_x) + n_y(u_y - v_y) + n_z(u_z - v_z)}{n_x(p_x - v_x) + n_y(p_y - v_y) + n_z(p_z - v_z)} \\
 &= \frac{\mathbf{N}_u \cdot \mathbf{U}_o}{\mathbf{N}_u \cdot \mathbf{P}_o},
 \end{aligned} \tag{2.19}$$

where  $\mathbf{U}_o$  is the vector from the point  $u$  to the surface point  $o$ , and  $\mathbf{P}_o$  is the vector from the light position  $p$  to the surface point  $o$ . If  $t$  satisfies  $0 \leq k \leq 1$  and the point  $r$  lies on the polygon that includes  $u$ , the line segment of Equation (2.18) is judged to cross the object.

### 2.4.3 Measurability of diffuse reflection only

When the pixel at surface point  $x$  exhibits only diffuse reflection, the half vector  $\mathbf{R}_{px}$  satisfies the following equation:

$$\theta_{rx} = \cos^{-1}(\mathbf{N}_x \cdot \mathbf{R}_{px}) > \theta_{th1}, \quad (2.20)$$

where  $\theta_{th1}$  is the threshold angle between  $\mathbf{N}_x$  and  $\mathbf{R}_{px}$ . Equation (2.20) implies that only the diffuse reflection component is observed if  $\theta_{rx}$  is greater than  $\theta_{th1}$  as illustrated in Figure 4.13. When this condition stands and the pixel is not in a shadow, then the pixel is judged to have diffuse reflection only and is counted in  $D_p$ .

### 2.4.4 Measurability of strong specular reflection

When the pixel at surface point  $x$  exhibits strong specular reflection, the half vector  $\mathbf{R}_{px}$  satisfies the following equation:

$$\theta_{rx} = \cos^{-1}(\mathbf{N}_x \cdot \mathbf{R}_{px}) \leq \theta_{th2}, \quad (2.21)$$

where  $\theta_{th2}$  is the threshold angle between  $\mathbf{N}_x$  and  $\mathbf{R}_{px}$ . Equation (2.21) implies that both the diffuse and specular reflection components are observed if  $\theta_{rx}$  is smaller than  $\theta_{th2}$ , as illustrated in Figure 2.10. The above condition is based on the fact that specular reflection is observed strongly in a limited viewing angle range. When this condition stands and the pixel is not in a shadow, then the pixel is judged to have strong specular reflection and is counted in  $S_p$ .

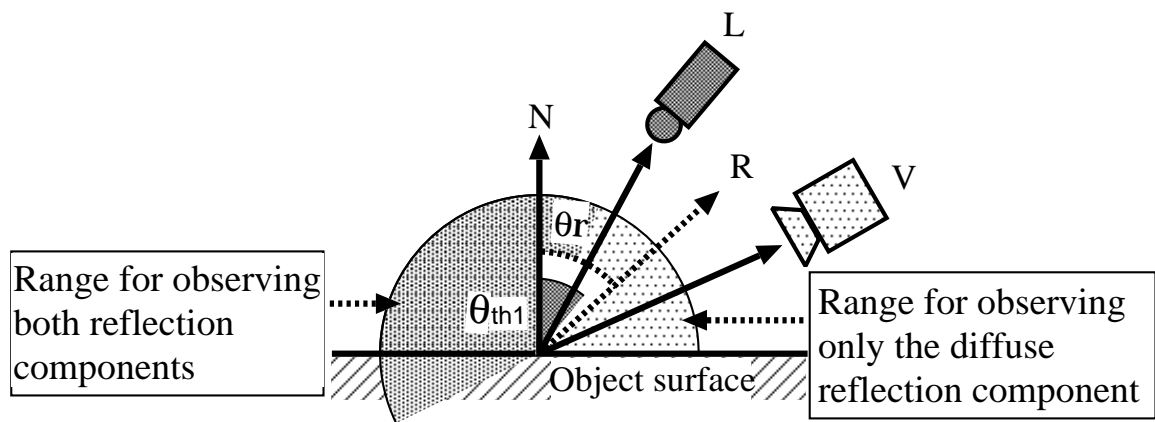


Figure 2.9. Observation of only the diffuse reflection component.

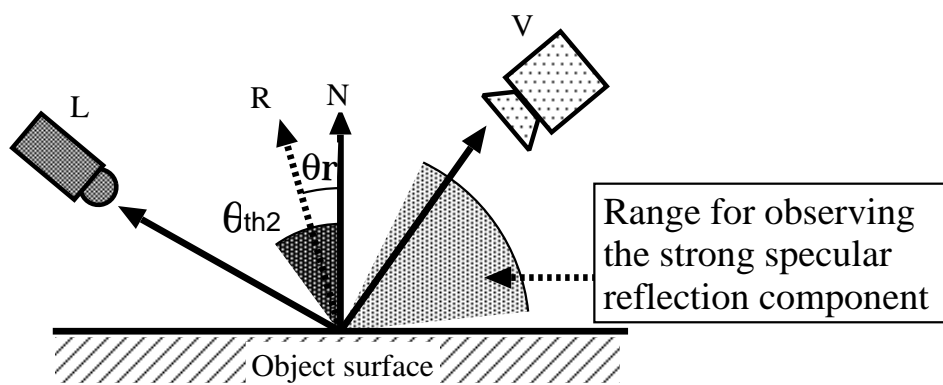


Figure 2.10. Observation of only the specular reflection component.



(a) Object A



(b) Object B



(c) Object C



(d) Object D

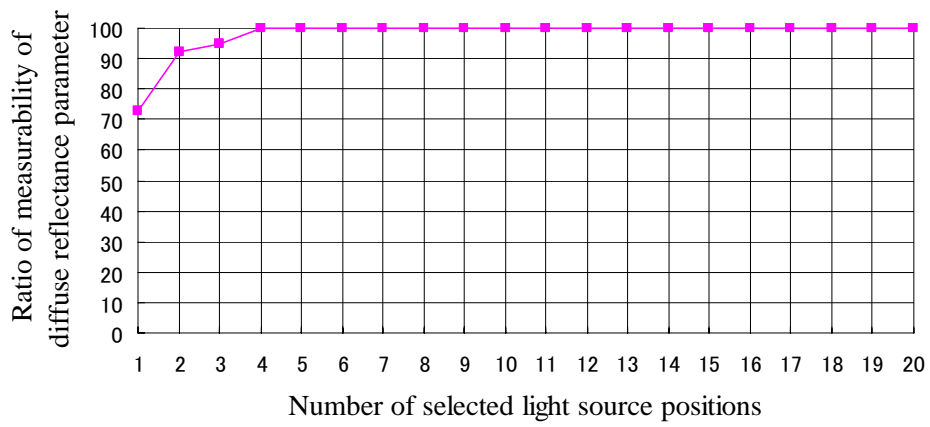
Figure 2.11. Four objects used in the experiment.

## 2.5. Experimental results

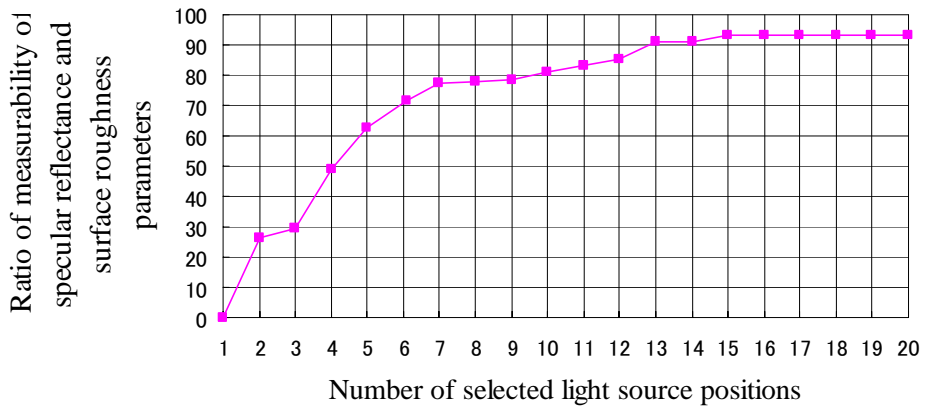
Next, the efficient selection of optimum light positions from a dense set of possible light positions is demonstrated experimentally. The actual measurability of both diffuse and specular reflection components on test objects are shown. Four objects are used in these experiments (Figure 2.11). Objects A and B have non-uniform reflectance properties with respect to both diffuse and specular reflection and have comparatively complicated geometries. These objects are mainly used to verify that the proposed methods can estimate an object with non-uniform reflectance properties (Chapter 3) and can eliminate the influence of interreflections (Chapter 4). Objects C and D have non-uniform diffuse reflectance and uniform specular reflectance properties. These objects are also mainly used to verify that the proposed methods can eliminate both diffuse and specular interreflections (Chapter 5). According to Ward et al. [War92], the

strong specular component can be observed within 20 degrees around the half vector  $\mathbf{R}$ . Therefore, the thresholds  $\theta_{th1} = 60^\circ$ ,  $\theta_{th2} = 20^\circ$ , and  $th_1 = 80\%$  are fixed. In addition, a PC (CPU: 3.06 GHz, Memory: 1 GB) is used in all of the experiments.

Figures 2.12 ~ 2.15 illustrate the measurability of both reflection components with respect to the number of light sources for Objects A ~ D. The vertical axis indicates the measurability of the diffuse or specular reflection component, and the horizontal axis indicates the number of selected light sources in the proposed light selection algorithm. Note that the horizontal axis only extends to 20 because these graphs do not change even if all 60 possible positions are used. In each of these figures, (a) shows the relationship between the number of selected light positions and the ratio of measurability of the diffuse reflection component. For example, in Figure 2.12(a), when the number of selected light source positions is five, the ratio of measurability of the diffuse reflection component is 100%. Moreover, (b) in each of these figure shows the relationship between the number of selected light positions and the ratio of measurability of the specular reflection component. For example, even when Object A is measured at all possible positions, the ratio of measurability of the specular reflection component is 83.53%. In the proposed method, the ratio of measurability of the specular reflection component is 83.46% with 12 automatically selected light source positions. The measurability of both reflection components and the number of selected light sources for estimating the reflectance parameters of Objects A, B, C and D are summarized in Table 2.2. The number in brackets indicates the number of selected light source positions required to estimate the diffuse reflectance parameter. This table also compares the proposed light selection method and the case of using all possible positions with respect to the measurability of the specular reflection component. The specular reflection component is shown to be observed in all objects by efficiently using a limited number of light source positions compared to using all 60 possible positions.

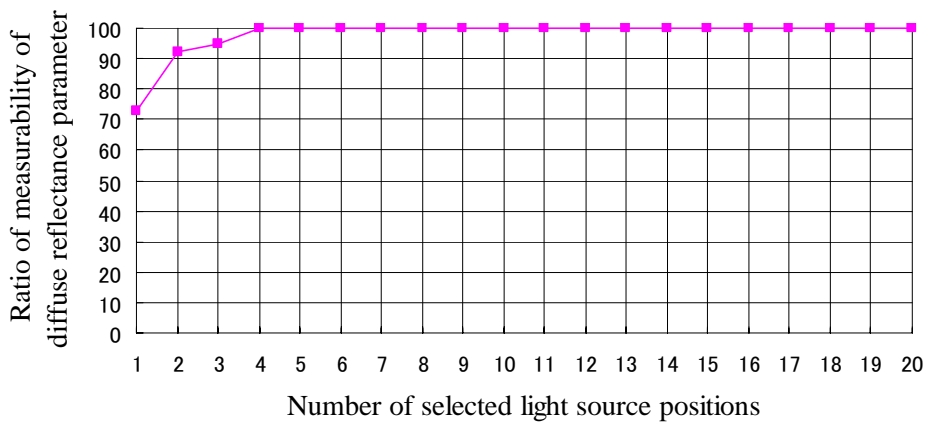


(a) Possibility of estimating the diffuse reflectance parameter

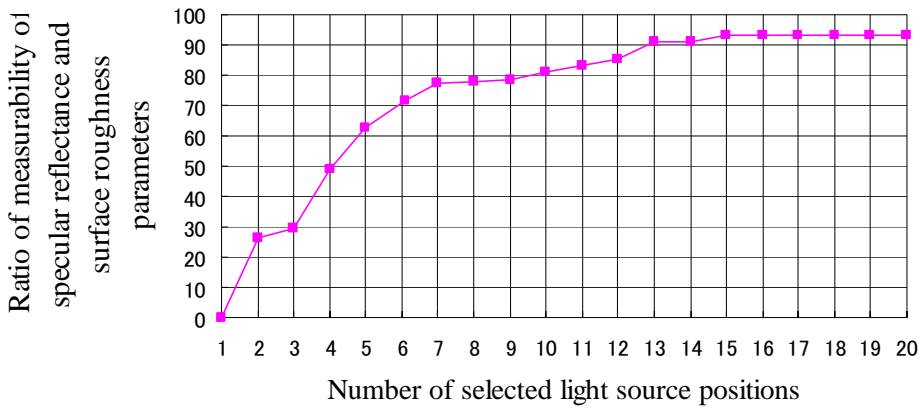


(b) Possibility of estimating the specular reflectance and the surface roughness parameters

Figure 2.12. Measurability of both reflection components for Object A.

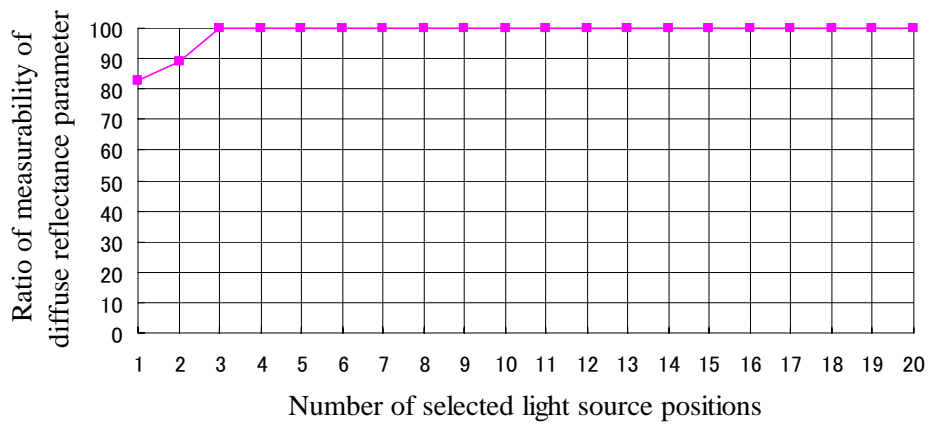


(a) Possibility of estimating the diffuse reflectance parameter

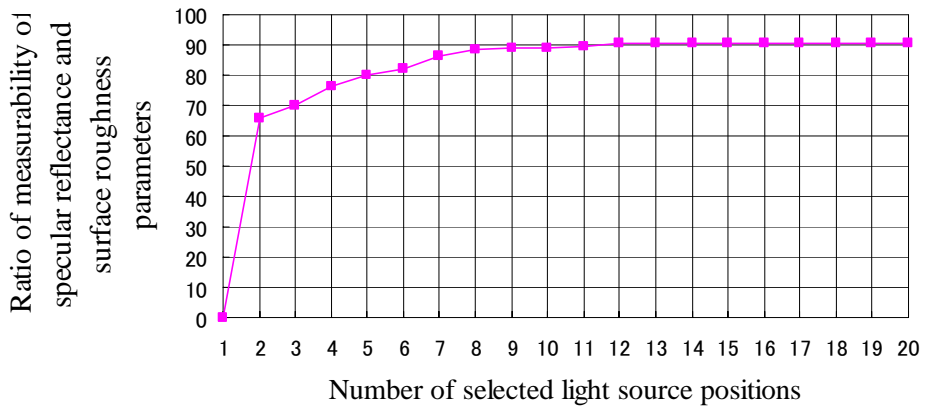


(b) Possibility of estimating the specular reflectance and the surface roughness parameters

Figure 2.13. Measurability of both reflection components for Object B.

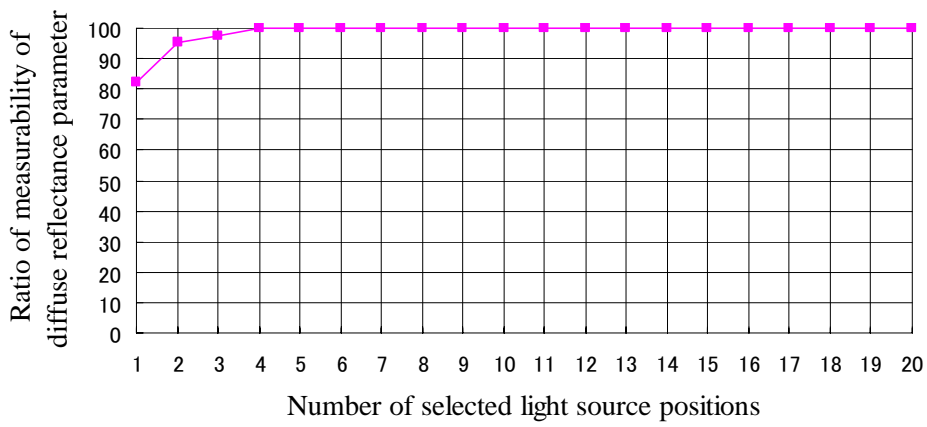


(a) Possibility of estimating the diffuse reflectance parameter

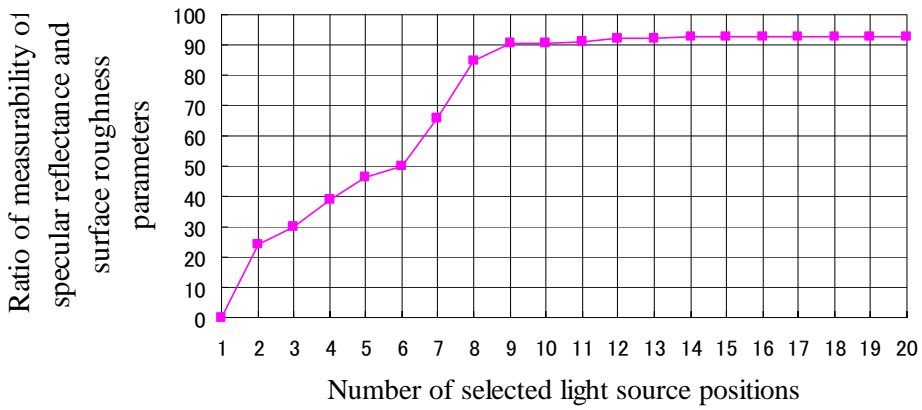


(b) Possibility of estimating the specular reflectance and the surface roughness parameters

Figure 2.14. Measurability of both reflection components for Object C.



(a) Possibility of estimating the diffuse reflectance parameter



(b) Possibility of estimating the specular reflectance and the surface roughness parameters

Figure 2.15. Measurability of both reflection components for Object D.

Table 2.2. Measurability of both reflection components and the number of selected light sources for estimating the reflectance parameters of Objects A, B, C and D.

Measurement object	Object A	Object B	Object C	Object D
Number of selected light positions	12(5)	14(4)	10(3)	9(4)
Diffuse reflection component	100.0%	100.0%	100.0%	100%
Specular reflection component (present method)	83.46%	91.02%	89.17%	91.72%
Specular reflection component (with 60 light positions)	83.52%	93.56%	91.27%	94.90%

## 2.6. Conclusions

In this chapter, an optimum light position selection method for densely observing both diffuse and specular reflection components on an object surface was proposed. In the present approach, multiple light source positions around the laser rangefinder are automatically selected based on the object geometry, so that diffuse and specular reflection components are observed densely. Since both reflection components must be observed at each object point for non-uniform surface reflectance estimation, the proposed method can be used for this purpose. Experiments have shown that the proposed method is useful for observing both reflection components densely. Dense observation of both diffuse and specular reflection components was verified for the four objects used in the experiments. However, specular reflection components can not be observed over the entire surface of an object, through either the proposed method or using all possible light positions. In order to address this problem, in the future, the proposed method will be improved by employing a light planning operation, such as those described in [WF91, LLSS03]. The following chapter describes the estimation of object surface reflectance properties based on the proposed optimum light selection method.

# Chapter 3

## Inverse Local Rendering for Dense Reflectometry Estimation

### 3.1. Introduction

In this chapter, the estimation of surface reflectance properties is described based on the registered range and color images taken by a laser rangefinder with selected light positions in the previous chapter. In the previous chapter, color images are obtained that include both diffuse and specular reflection components densely on the object surface. The surface reflectance properties are estimated using these color images and the object geometry, and these properties are specifically fit to the local rendering model. The Torrance-Sparrow model [TS67] described in Chapter 2 is used as the local rendering model. In other words, *inverse local rendering* is performed for the data obtained in previous chapter. Recall that the Torrance-Sparrow model is given as:

$$i_x = \frac{Y}{C^2} \left\{ P_{dx} \cos \theta_{dx} + \frac{P_{sx}}{\cos \theta_{vx}} \exp\left(-\frac{\theta_{vx}^2}{2\sigma_x^2}\right) \right\}, \quad (3.1)$$

where  $x$  denotes the surface point,  $i_x$  represents an observed intensity,  $C$  is an attenuation coefficient concerning the distance between a point light source and an object surface point, and  $Y$  represents the strength of a light source. In addition,  $P_{dx}$ ,  $P_{sx}$  and  $\sigma_x$  are the diffuse reflectance, the specular reflectance and the surface roughness parameters, respectively, and  $\theta_{dx}$  is the angle between a light source vector and a surface normal vector,  $\theta_{vx}$  is the angle between a viewing vector and a surface normal

vector, and  $\theta_{rx}$  is the angle between a surface normal vector and a half vector. Note that the half vector is located halfway between the light vector and the viewing vector. Here,  $\theta_{rx}$  is used to judge whether or not specular reflection occurs. The following section describes *how to estimate* the object surface reflectance properties densely using the Torrance-Sparrow model. Note that the Torrance-Sparrow model supports both non-metal and heterogeneous dielectric materials, and cannot be used to estimate the object surface reflectance properties for metallic materials. In addition, although the Torrance-Sparrow model supports the Fresnel component, the Fresnel component is ignored because the object is assumed to be opaque. Moreover, mirror-finish material is not supported. Thus, the proposed estimation method using the Torrance-Sparrow model cannot deal with metallic materials, opaque materials, or mirror-finish materials.

## 3.2. Estimation of surface reflectance parameters

After the positions of the light sources are determined as described in Chapter 2, multiple color images are taken under different lighting conditions. Figure 3.1 shows a flow diagram of surface reflectance modeling. The proposed process consists of the four parts in Figure 2.1: measurement of an object and preprocessing (A, C), selection of a light source (B) (as described in Chapter 2), and estimation of reflectance parameters (D). In the estimation process (D), non-uniform reflectance parameters are estimated by substituting the object shape and textures under selected illumination conditions into the surface color reflection model. Throughout this chapter, it is assumed that there are no interreflections on the object surface.

Let  $I_{p,diff}$  be a set of pixels that include only the diffuse reflection component with possible light position  $p$ , as well as  $\gamma$  pixels  $(i_{p,d1}, \dots, i_{p,d\gamma})$ , where  $i_{p,dx}$  denotes the color intensity corresponding to the surface point  $x$ . If it is judged that  $i_{p,dx}$  does not consist of only the diffuse reflection component, then  $i_{p,dx} = 0$ . Let  $I_{p,both}$  be a set of pixels that include the specular reflection component strongly, as well as  $\gamma$  pixels  $(i_{p,b1}, \dots, i_{p,b\gamma})$ , where  $i_{p,bx}$  denotes the color intensity on the object surface point  $x$ . If it is judged that  $i_{p,bx}$  does not include the strong specular reflection component, then  $i_{p,bx} = 0$ . In addition,  $T_{diff}$  denotes a pixel containing only the diffuse reflection component, and  $T_{spec}$  denotes a pixel that contains a strong specular reflection component. Moreover,  $T_{none}$  denotes a pixel that is classified as being neither  $T_{diff}$  nor  $T_{spec}$ . Each

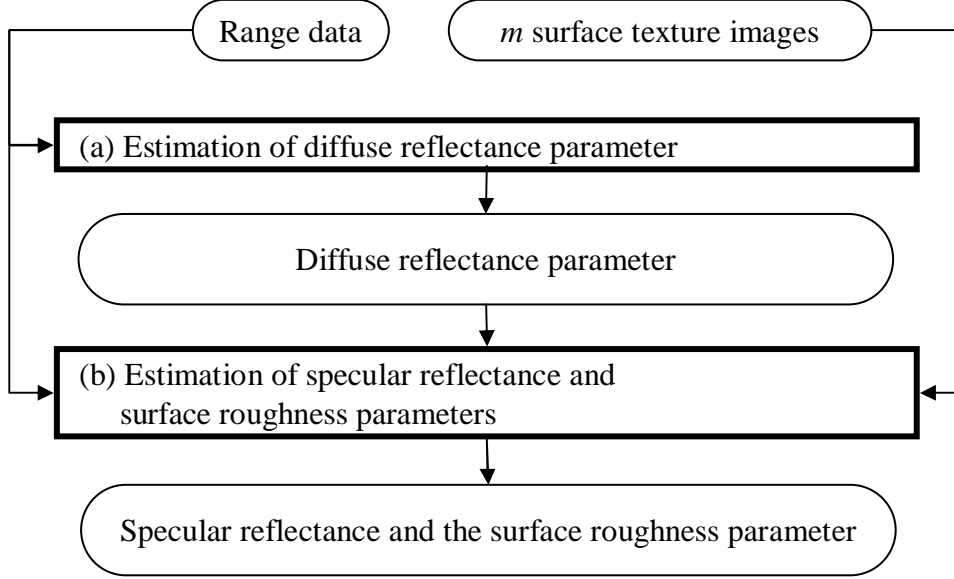


Figure 3.1. Flow diagram of inverse local rendering for surface reflectance modeling.

pixel is classified as belonging to either  $T_{diff}$ ,  $T_{spec}$  or  $T_{none}$ .

### 3.2.1 Estimation of diffuse reflectance parameter

The estimation process is performed at each point on the object surface. Pixels in multiple images corresponding to the object surface are used, as shown in Figure 3.2. The diffuse reflectance parameter  $P_{dx}$  at surface point  $x$  is estimated by solving the following equation from Equation (2.11).

$$i_{p,dx} = \frac{Y}{C^2} P_{dx} \cos \theta_{dx}, \quad (3.2)$$

$$P_{dx} = \frac{C^2 i_{p,dx}}{Y \cos \theta_{dx}}, \quad (3.3)$$

where  $i_{p,dx}$  is the value of the pixel at surface point  $x$  in the image  $i_{p,dx}$ , and  $\cos \theta_{dx}$  is calculated from surface normal vector  $\mathbf{N}_x$  and light source vector  $\mathbf{L}_{px}$ . In order to obtain the most reliable estimation, the pixel having the smallest angle  $\theta_{rx}$  that is greater than  $\theta_{th1}$  is selected.

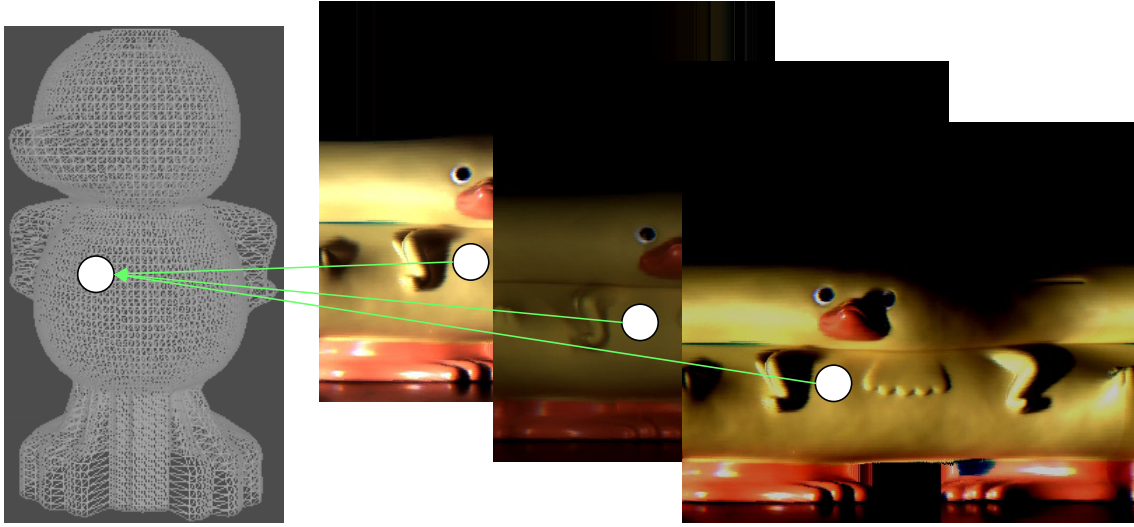


Figure 3.2. Point on the Object in multiple texture images.

### 3.2.2 Estimation of specular reflectance and surface roughness parameters

The specular reflectance parameter  $P_{sx}$  and the surface roughness parameter  $\sigma_x$  at surface point  $x$  are also estimated by solving Equation (2.12) with  $\mathbf{N}_x$ ,  $\mathbf{L}_{px}$ ,  $\mathbf{V}_x$  and the value of the specular reflection component that is extracted from pixels  $i_{p,bx}$  and  $i_{q,bx}$  in images  $I_{p,both}$  and  $I_{q,both}$ . In order to obtain the most reliable estimation, either the pixels having the smallest angle  $\theta_{rx}$ , or those having the second smallest angle  $\theta_{rx}$  that are smaller than  $\theta_{th2}$ , are selected.

First, the diffuse reflection component is computed with the diffuse reflectance parameter  $P_{dx}$ , estimated above, and Equation (2.11). Next, the specular reflection component is extracted by subtracting the diffuse reflection component from Equation (2.10).

$$\begin{cases} i_{p,sx} &= i_{p,bx} - i_{p,dx} \\ i_{q,sx} &= i_{q,bx} - i_{q,dx} \end{cases} \quad (3.4)$$

Finally, the specular reflectance and surface roughness parameters are obtained by

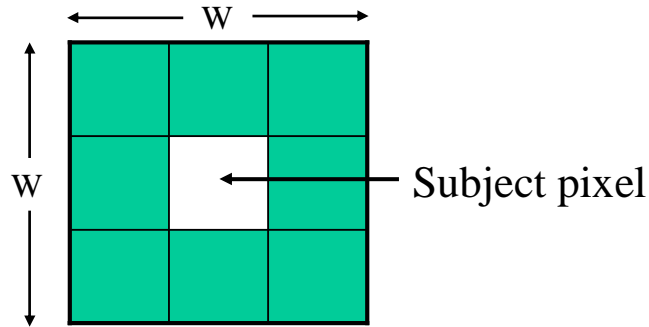


Figure 3.3. A window for linearly interpolating undetermined pixels.

solving Equation (2.12).

$$\begin{cases} i_{p,sx} \cos \theta_{vx} = P_{sx} \cdot \exp(-\theta_{rx1}^2/2\sigma_x^2) \\ i_{q,sx} \cos \theta_{vx} = P_{sx} \cdot \exp(-\theta_{r2}^2/2\sigma_x^2) \end{cases} \quad (3.5)$$

Equation (2.12) cannot be solved for pixels at which strong specular reflection is observed less than twice. In such cases, the specular reflectance and surface roughness parameters are obtained using a linear-interpolation method within a  $W \times W$  window (Figure 3.3).

### 3.3. Experimental results

In order to verify the proposed method, experiments were carried out to densely estimate the reflectance parameters of Objects A ~ D, shown in Figure 2.11. Note that with respect to the window size used in interpolation method,  $W = 5$  is fixed.

#### 3.3.1 Estimated reflectance parameters

Estimated parameters for the objects are shown in Figures 3.4~3.7, where the parameter values are represented by color or intensity in cylindrical coordinates. The diffuse reflectance parameter estimated over the object surface is shown in (a) in each figure. The specular reflectance and surface roughness parameters are shown in (b) and (c), respectively, in each figure. Note that in each figure (c) is illustrated in gray scale, in which the largest value is represented as white. This image indicates that the smaller the value, the smoother the object surface. In addition, (d) in each figure illustrates the ratio of pixels at which the specular reflectance and surface roughness parameters can be computed. The black area indicates the area in which neither parameter can be directly estimated.

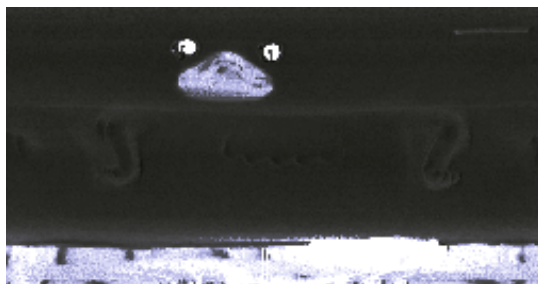
In Figure 3.4, the specular reflectance and surface roughness parameters of the beak and leg of the object clearly differ from those of the other areas. Actually, the beak and legs are highly reflective, as can be seen in Figure 2.11(a). In Figure 3.5, the reflectance parameters of Object B, having a more complex geometry, are estimated. This figure shows that some parts have the diffuse reflection component and other parts have the specular reflection component, as is the case for Object A. These results verify that non-uniform surface reflectance properties can be observed efficiently using the proposed light selection method.

Objects C and D also have specular reflection components. These objects actually have uniform specular reflectance and surface roughness parameters, as can be observed in Figure 2.11(c) and (d). These observations can be confirmed from Figures 3.6 (b) and (c) and 3.7 (b) and (c).

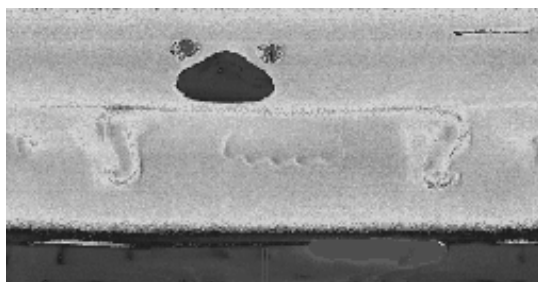
These results also show that uniform or non-uniform specular reflectance and surface roughness parameters are estimated without interpolation for more than nearly 90% of the surface.



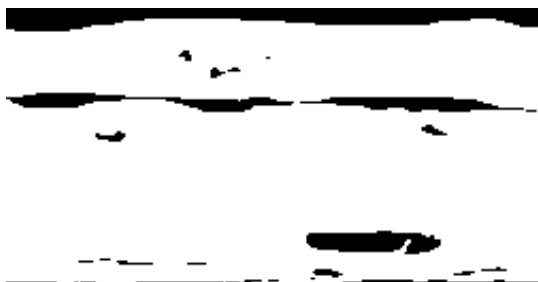
(a) Diffuse reflectance parameter ( $P_d$ )



(b) Specular reflectance parameter ( $P_s$ )



(c) Surface roughness parameter ( $\sigma_d$ )



(d) Observation area for specular reflection

Figure 3.4. Estimated reflectance parameters for Object A.



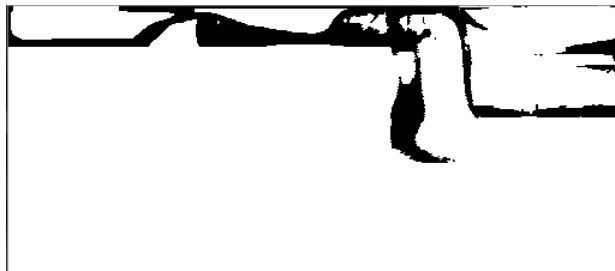
(a) Diffuse reflectance parameter ( $P_d$ )



(b) Specular reflectance parameter ( $P_s$ )

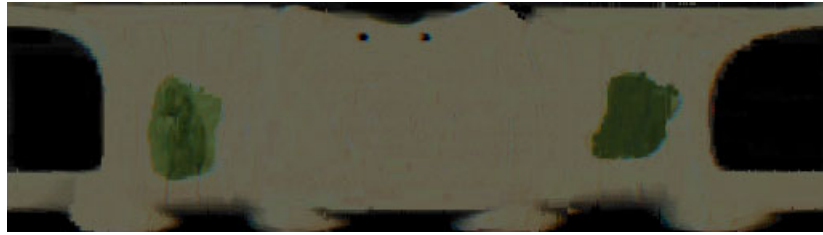


(c) Surface roughness parameter ( $\sigma_d$ )

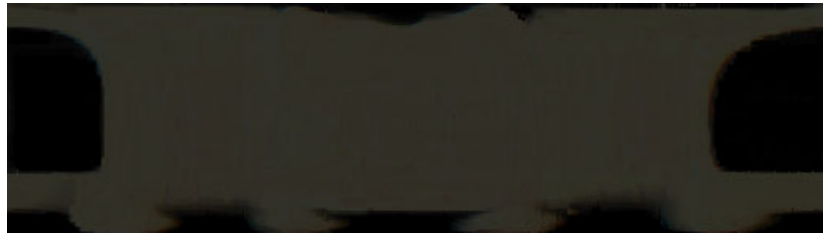


(d) Observation area for specular reflection

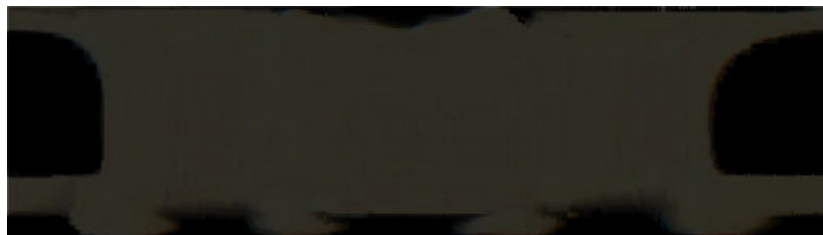
Figure 3.5. Estimated reflectance parameters for Object B.



(a) Diffuse reflectance parameter ( $P_d$ )



(b) Specular reflectance parameter ( $P_s$ )



(c) Surface roughness parameter ( $\sigma_d$ )



(d) Observation area for specular reflection

Figure 3.6. Estimated reflectance parameters for Object C.



(a) Diffuse reflectance parameter ( $P_d$ )



(b) Specular reflectance parameter ( $P_s$ )



(c) Surface roughness parameter ( $\sigma_d$ )



(d) Observation area for specular reflection

Figure 3.7. Estimated reflectance parameters for Object D.



Figure 3.8. Rendering results for Object A with the Torrance-Sparrow model.



Figure 3.9. Rendering results for Object B with the Torrance-Sparrow model.

### 3.3.2 Rendering results with the Torrance-Sparrow model

Finally, the virtual re-lighting of virtualized objects is demonstrated. Figures 3.8 ~ 3.11 show the rendering of virtualized Objects A, B, C and D under a virtual lighting condition. A virtual light source is fixed at  $(0.0, 0.0, 300.0)$ , and the origin of the coordinate system is located at the center of the object. Rotation is around the vertical axis of each object. Figure 3.8 ~ 3.11 contains six views around the virtualized objects. Each result shows the potential usefulness of the proposed method, although some spike noises are present due to sensor error in the range data. These results qualitatively show the effectiveness of the proposed surface reflectance modeling method.

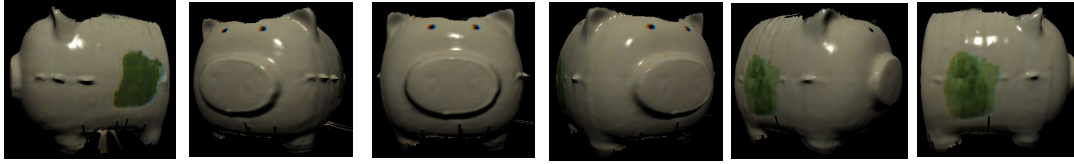


Figure 3.10. Rendering results for Object C with the Torrance-Sparrow model.

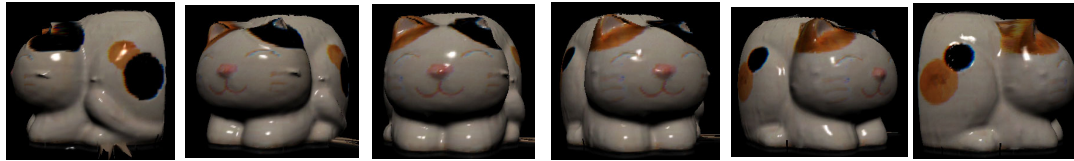


Figure 3.11. Rendering results for Object D with the Torrance-Sparrow model.

### 3.4. Discussion

In this chapter, non-uniform object surface reflectance properties were densely estimated using a local illumination model (Torrance-Sparrow model). As described in Chapter 2, because the local illumination model considers only the direct illumination effect on the object surface, errors may exist if interreflections occur. In this section, the degree to which errors due to the influence of interreflections affect the proposed method.

In this experiment, Object E, shown in Figure 3.12, which is separated into Regions I and II, was used. Two setups were examined. In the first setup, the same white paper having a uniform diffuse reflectance surface is pasted to both regions (Setup 1). In the second setup, the same glossy paper having a uniform reflectance surface is pasted up to both regions (Setup 2). In both setups, Object E was placed on the table obliquely, as shown in Figure 3.13, so that the influence of interreflections could be observed. If interreflections occur, it is expected that the estimated value in the inverse local rendering method will exhibit incorrect results in this area. The results for diffuse (Setup 1) and specular (Setup 2) surfaces are shown in Figures 3.14 and 3.15, respectively. Each graph represents the RGB channels of the diffuse reflectance parameter estimated in both setups. The horizontal axis in the graphs indicates the position of the surface point in the vertical direction of Object E, and the vertical axis indicates the average diffuse reflectance parameter in the horizontal direction of the

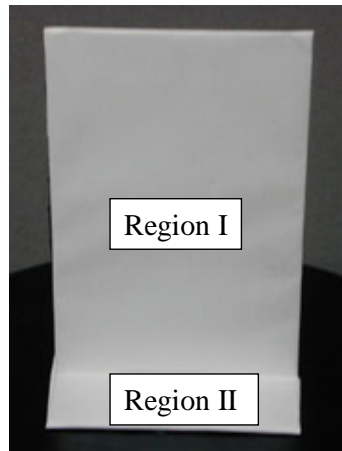


Figure 3.12. An object with interreflections (Object E).

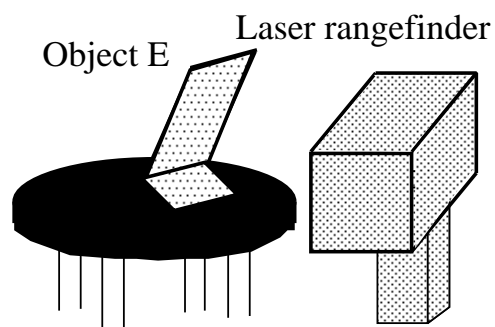
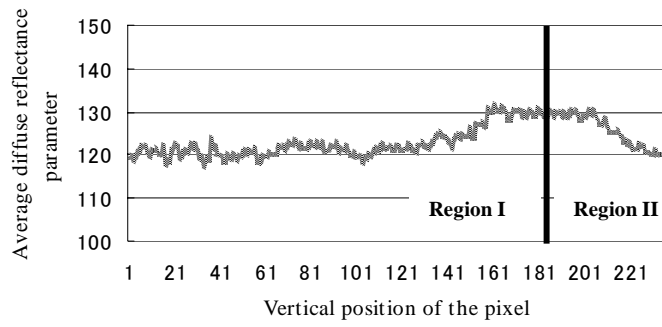
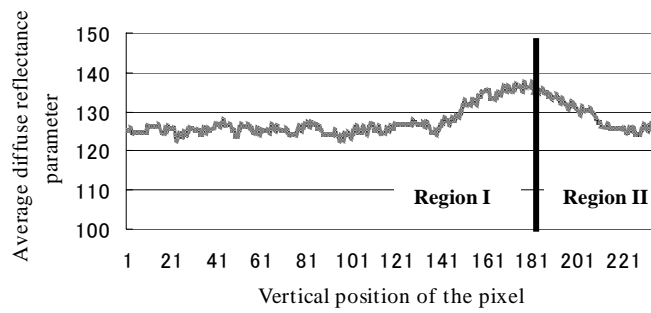


Figure 3.13. Position of Object E in the experiment.

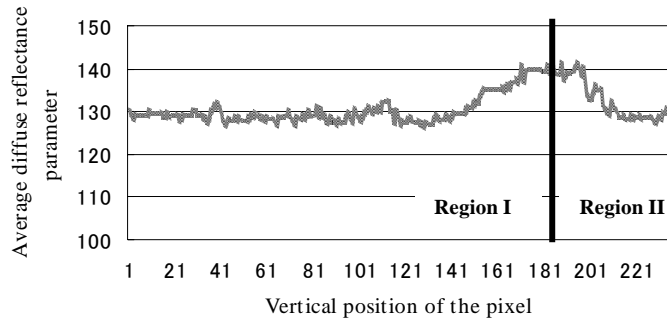
object. As shown in Figure 3.14, the diffuse reflectance parameters estimated using the present method are large around the boundary between regions  $\alpha$  and  $\beta$ . Moreover, the influence of interreflections also remains in the glossy surface, as is noticeable in Figure 3.15, because interreflections due to the specular reflection also occur at the boundary between Regions I and II in the second setup. In this experiment, the influence of interreflections is actually observed to cause errors in estimation of the object surface reflectance properties.



(a) R channel

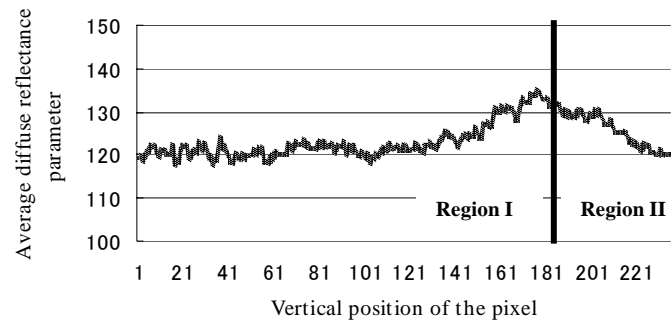


(b) G channel

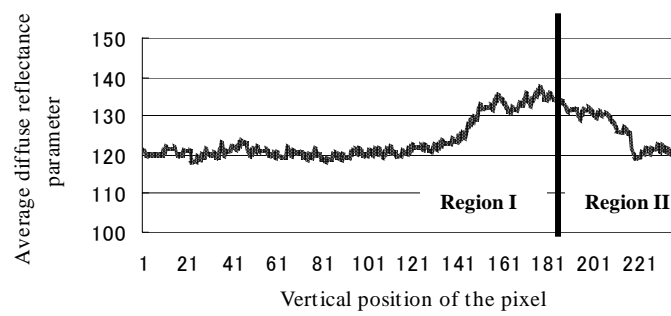


(c) B channel

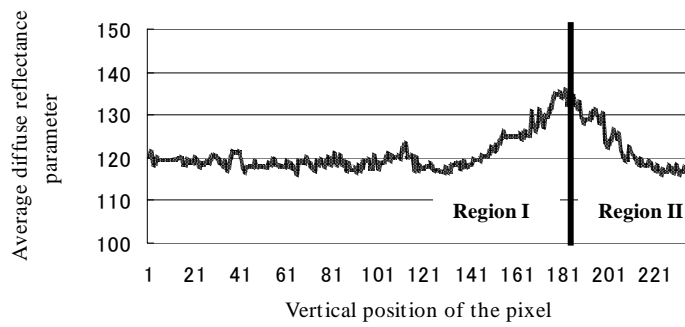
Figure 3.14. Estimated diffuse reflectance parameter in Experimental Setup 1.



(a) R channel



(b) G channel



(c) B channel

Figure 3.15. Estimated diffuse reflectance parameter in Experimental Setup 2.

## **3.5. Conclusions**

In this chapter, a method was proposed for densely estimating non-uniform reflectance properties for almost the entire object surface using the laser rangefinder for virtualizing real objects. In the proposed approach, multiple light source positions around the laser rangefinder were automatically selected, as described in Chapter 2, so that the diffuse and specular reflection components are observed densely. The experiments revealed that the proposed method is useful for estimating the reflectance parameters of objects that exhibit non-uniform surface reflectance. However, some errors remain due to both diffuse and specular interreflections. The following chapters will address this problem by employing global illumination models.

## Chapter 4

# Inverse Radiosity for Dense Reflectometry Estimation

### 4.1. Introduction

Most real object surfaces exhibit specular as well as diffuse reflection. Recovering both diffuse and specular reflectance models simultaneously in a mutual illumination environment is complicated. This chapter describes the reflectance estimation method using radiosity [ICG86] in order to consider interreflections. The radiosity rendering method considers and renders the effect of diffuse interreflections. Hence, *inverse radiosity rendering* can estimate surface reflectance parameters without the influence of diffuse interreflections. Note that, in this chapter, interreflections are assumed to be influenced by only the diffuse reflection component, and not by the specular reflection component. In the proposed method, pixels that were judged in Chapter 2 to have only the diffuse reflection component are used in the estimation of the diffuse reflectance parameter considering diffuse interreflections. In other words, the situation can be simplified such that the surface has only diffuse reflection components. In this case, the global illumination problem is simplified considerably and can be treated in the radiosity framework.

## 4.2. Radiosity rendering method

In most shading algorithms (i.e. the Torrance-Sparrow model), light sources have always been treated separately from the surfaces they illuminate. In contrast, radiosity methods [ICG86] allow any surface to emit light, and so all light sources are modeled inherently as having area. In the radiosity method, the environment is broken up into a finite number  $\gamma$  of discrete patches, each of which is assumed to be of finite size, emitting and reflecting light uniformly over its entire area. If each patch is considered to be an opaque Lambertian diffuse emitter and reflector, then, for surface  $u$ ,

$$B_u = E_u + P_{du} \sum_{v=1}^{\alpha} B_v F_{vu} \frac{A_v}{A_u}, \quad (4.1)$$

$$F_{uv} = \frac{1}{A_u} \int_{A_u} \int_{A_v} \frac{\cos \theta_u \cos \theta_v}{\pi r^2} H_{uv} dA_u dA_v, \quad (4.2)$$

where  $B_u$  and  $B_v$  ( $1 \leq u, v \leq \gamma$ ) are the radiosities of patches  $u$  and  $v$ , respectively, measured in energy/unit time/unit area (i.e.,  $W/m^2$ ). Note that  $\gamma$  is the number of object patches.  $E_u$  is the rate at which light is emitted from patch  $u$  and has the same units as radiosity.  $P_{du}$  is the reflectivity of patch  $u$  and is dimensionless.

In addition,  $F_{uv}$  is called the dimensionless *form factor*, which specifies the fraction of energy leaving the entirety of patch  $v$  that arrives at the entirety of patch  $u$ , taking into account the shape and relative orientation of both patches and the presence of any obstructing patches (See, Figure 4.1),  $A_u$  and  $A_v$  are the areas of patches  $u$  and  $v$ , respectively,  $\theta_u$  is the angle that the ray makes with the normal  $N_u$  of  $A_u$ ,  $\theta_v$  is the angle that the ray makes with the normal  $N_v$  of  $A_v$ , and  $r$  is the length of the ray. Moreover,  $H_{uv}$  is either 1 or 0, depending on whether  $dA_u$  is visible from  $dA_v$ .

Figure 4.1 shows that the form factor from differential area  $dA_u$  to differential area  $dA_v$  is

$$dF_{uv} = \frac{\cos \theta_u \cos \theta_v}{\pi r^2} H_{uv} dA_v. \quad (4.3)$$

Determining  $F_{uv}$ , the form factor from differential area  $dA_u$  to finite area  $A_v$ , requires integration over the area of patch  $v$  as follows:

$$dF_{uv} = \int_{A_v} \frac{\cos \theta_u \cos \theta_v}{\pi r^2} H_{uv} dA_v. \quad (4.4)$$

Finally, the form factor represented as Equation (4.2) from  $A_u$  to  $A_v$  is the area average of Equation (4.4).

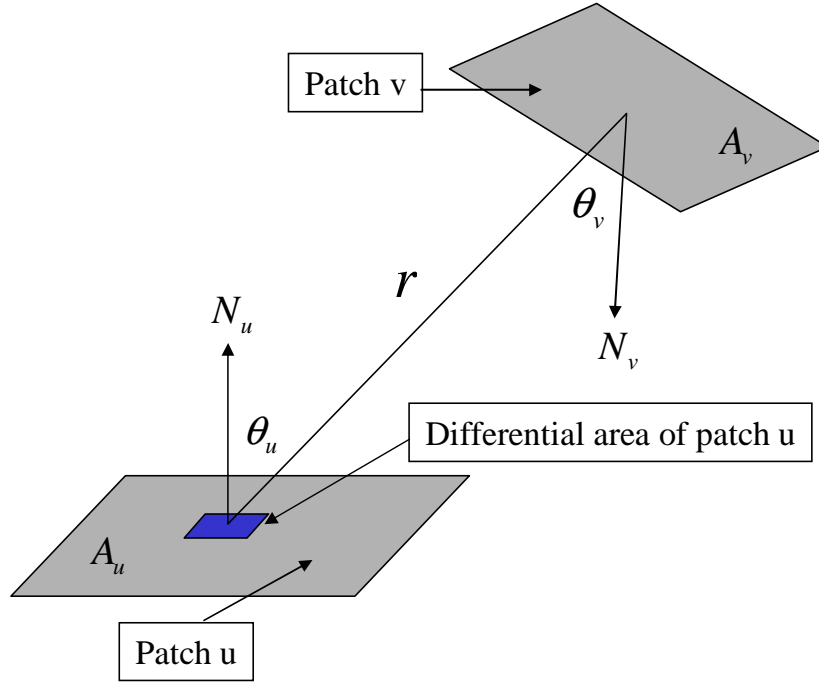


Figure 4.1. Computing the form factor between a patch and a differential area.

Equation (4.1) states that the energy leaving a unit area of surface is the sum of the light emitted plus the light reflected. The reflected light is computed by scaling the sum of the incident light by the reflectivity. The incident light is in turn the sum of the light leaving the entirety of each patch in the environment scaled by the fraction of that light reaching a unit area of the receiving patch. Here,  $B_v F_{uv}$  represents the amount of light leaving a unit area of  $A_u$  that reaches all of  $A_v$ . Therefore, multiplication by the area ratio  $A_v/A_u$  is necessary in order to determine the light leaving all of  $A_v$  that reaches a unit area of  $A_u$ .

Conveniently, the following simple reciprocity relationship holds between form factors in diffuse environments:

$$A_u F_{uv} = A_v F_{vu}. \quad (4.5)$$

Thus, Equation (4.1) can be simplified to yield

$$B_u = E_u + P_{du} \sum_{v=1}^{\alpha} B_v F_{uv}. \quad (4.6)$$

This equation is referred to as the radiosity equation. In this equation, the form factor  $F_{uv}$  is required. A number of studies have been developed for calculating form factor. Cohen et al. [CG85] adapted an image-precision visible-surface algorithm to efficiently approximate form factors for occluded surfaces. Nusselt [SH81] has shown that computing a form factor  $F_{uv}$  is equivalent to projecting those parts of  $A_v$  that are visible from  $dA_u$  onto a unit *hemisphere* centered about  $dA_u$ , projecting this projected area orthographically down onto the unit circle base of the hemisphere, and dividing by the area of the circle (See, Figure 4.2). Projection onto the unit hemisphere accounts for  $\cos \theta_v / r^2$  in Equation (4.4). Projection down onto the base corresponds to multiplication by  $\cos \theta_u$ . Finally, division by the area of the unit circle accounts for  $\pi$  in the denominator. Cohen et al.[CGIB86] also developed an efficient image-precision algorithm that projects patch  $v$  onto the upper half of a cube centered about  $dA_u$ , with the top of the cube being parallel to the surface (Figure 4.3). Each face of this *hemicube* is divided into a number of equal-sized square cells. All of the other patches are clipped to the view-volume frusta defined by the center of the cube and each of its upper five faces, and each of the clipped patches is then projected onto the appropriate face of the hemicube.

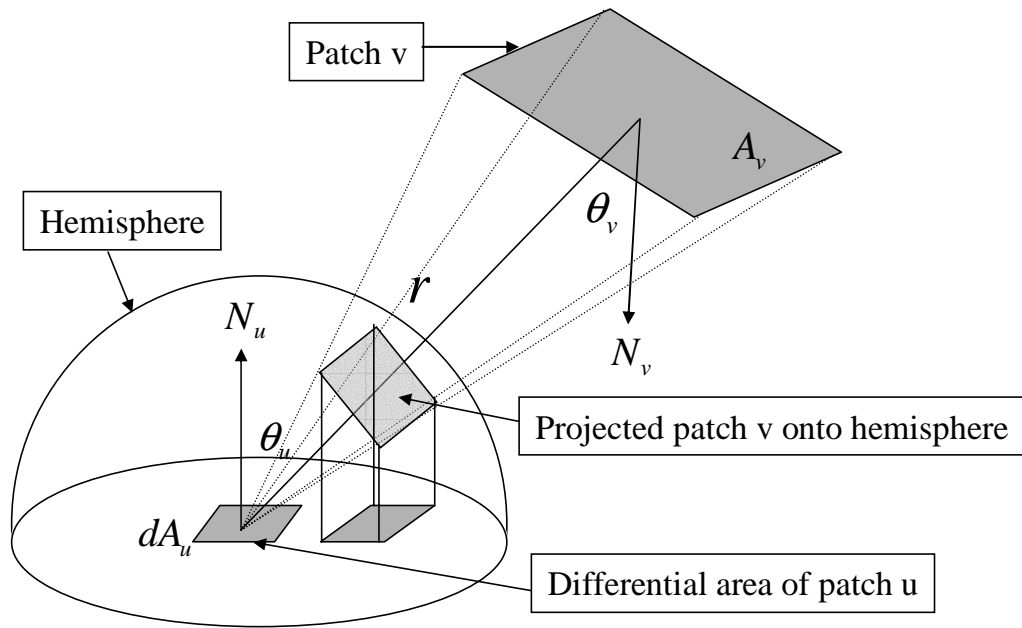


Figure 4.2. Hemisphere method for efficient calculation of form factor.

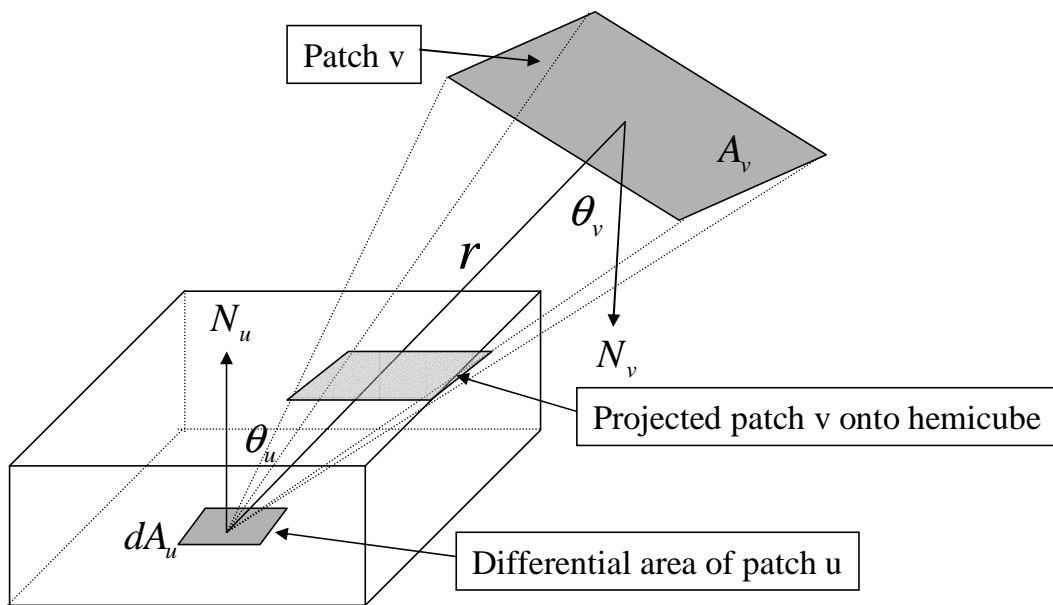


Figure 4.3. Hemicube method improving the hemisphere method.

### 4.3. Estimation of surface reflectance parameters considering diffuse interreflections

Since in the present study, the object is measured in a dark room, the influence of environmental light can be ignored. In other words, the form factor between each patch of the object and the wall of the dark room need not be calculated.

Recall that Figure 2.1 shows a general flow diagram of the estimation of surface reflectance properties by the proposed method. The proposed method consists of four parts. The first three processes (A, B and C) have already been described in Chapter 2, and involve the measurement of an object (A and C), and the selection of a light source (B), respectively. In this chapter, process (D) involves *inverse radiosity rendering* for estimating the diffuse reflectance parameter and the estimation of the specular reflectance and surface roughness parameters using the Torrance-Sparrow model.

Multiple texture images are obtained with selected optimum light positions as described in Chapter 2. Each pixel is also classified into one of three types:  $T_{diff}$ ,  $T_{spec}$  or  $T_{none}$ .  $T_{diff}$  indicates a pixel containing only the diffuse reflection component, and  $T_{spec}$  indicates a pixel containing a strong specular reflection component. In addition,  $T_{none}$  indicates a pixel that is classified as neither  $T_{diff}$  nor  $T_{spec}$  and that is not used to estimate reflectance parameters.

#### 4.3.1 Estimation of diffuse reflectance parameter based on radiosity

Figure 4.4 shows the details of the inverse radiosity rendering method. The proposed method has three processes. In the proposed method, the hemicube method [CGIB86] can be used for calculating the form factor  $F_{uv}$  because the object shape has already been measured by laser rangefinder. Since the range and texture images are registered at each pixel, the radiosity  $B_u$  of patch  $u$  is calculated based on the sum of the values of the pixels that correspond to patch  $u$ . Here,  $P_{du}$  represents the diffuse reflectance parameter on patch  $u$ . Then, the diffuse reflectance parameter  $P_{du}$  is determined as follows:

$$P_{du} = \frac{B_u - E_u}{\sum_{v=1}^{\alpha} B_v F_{uv}}, \quad (4.7)$$

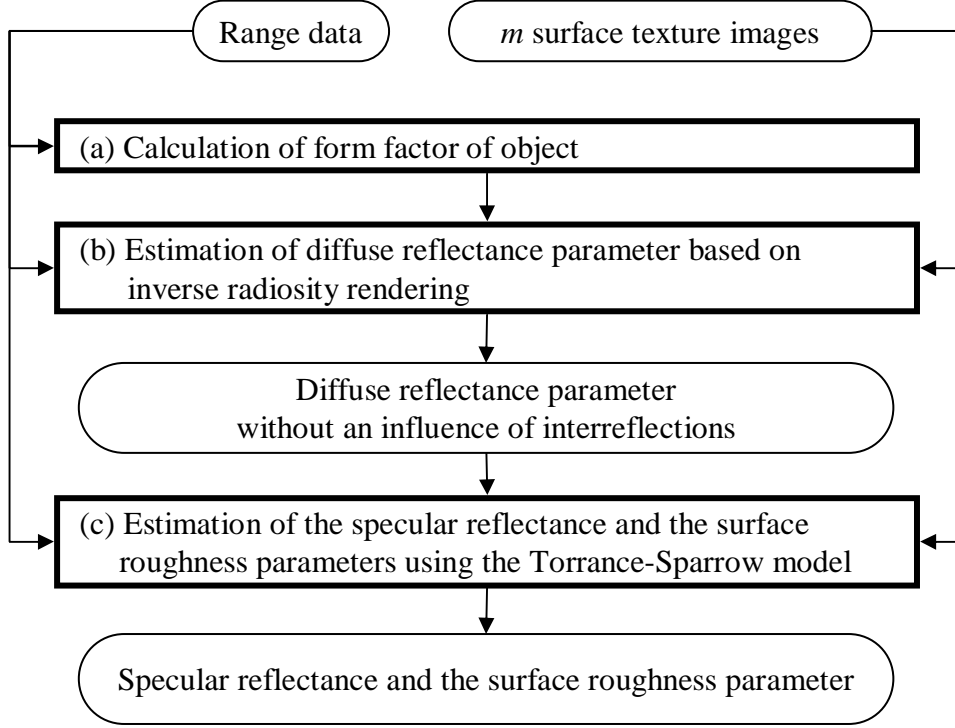


Figure 4.4. Flow diagram of estimating surface reflectance properties based on inverse radiosity rendering.

where  $E_u$  is 0, because there is no emission at patch  $u$  on the object. Finally, the diffuse reflectance parameter at each surface point is estimated by calculating the average among neighboring patches that share the point.

Here, the calculation of the radiosity  $B_u$  of patch  $u$  is described in further detail. Each patch consists of four points, and  $B_u$  is represented as the sum of the color values of the pixels that correspond to these points. Let us suppose that the patch  $u$  contains pixels  $s$  and  $t$ . It should be noted that the pixel values  $e_s$  and  $e_t$  of  $s$  and  $t$  in  $T_{diff}$  are obtained with different light positions,  $p(s)$  and  $p(t)$ , respectively, because the light source attached to the rangefinder moves during measurement. The calculation of  $B_u$  requires the use of the color value  $\hat{e}_t$  of the pixel  $t$  with the light position  $p(s)$ . From Lambert's law, the color value  $\hat{e}_t$  can be obtained by:

$$\hat{e}_t = \frac{\mathbf{N}_t \cdot \mathbf{L}_{p(s)t}}{\mathbf{N}_s \cdot \mathbf{L}_{p(s)s}} e_s, \quad (4.8)$$

where  $\mathbf{N}_s$  and  $\mathbf{N}_t$  are normal vectors at pixels  $s$  and  $t$ .  $\mathbf{L}_{p(s)s}$  and  $\mathbf{L}_{p(s)t}$  are light vectors

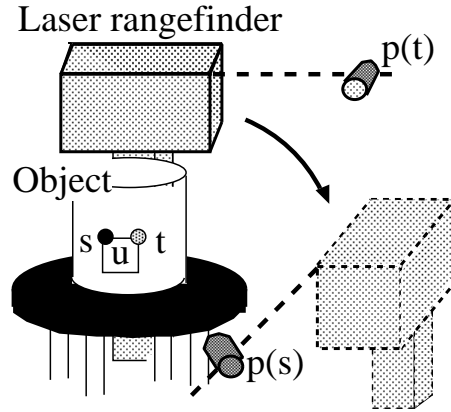


Figure 4.5. Calculation of radiosity.

with the light position  $p(s)$  at pixels  $s$  and  $t$ . Note that in the case of  $\mathbf{N} \cdot \mathbf{L} \leq 0$ , the color value  $\hat{e}_t$  should be 0 in order to consider the measurability of light reflection.

### 4.3.2 Estimation of specular reflectance and surface roughness parameters based on the Torrance-Sparrow model

The specular reflectance and the surface roughness parameters are estimated using the Torrance-Sparrow model as:

$$i_x = \frac{Y}{C^2} \left\{ P_{dx} \cos \theta_{dx} + \frac{P_{sx}}{\cos \theta_{vx}} \exp\left(-\frac{\theta_{rx}^2}{2\sigma_x^2}\right) \right\}. \quad (4.9)$$

The specular reflectance parameter  $P_{sx}$  and the surface roughness parameter  $\sigma_x$  at the surface point  $x$  are estimated by solving the simultaneous equations of Equation (4.9). In this case, the pixel values of the specular reflection components extracted from the two images taken under two different illumination conditions and the previously estimated  $P_{dx}$  were used.

$$\begin{cases} i_{p,sx} &= i_{p,bx} - i_{p,dx} \\ i_{q,sx} &= i_{q,bx} - i_{q,dx} \end{cases} \quad (4.10)$$

With respect to the attenuation coefficient of a point light source  $Y/D^2$ , the attenuation by the distance between a certain object surface point and the point light source is set

as unity, and the attenuation with respect to the rest of the surface points is calculated. Note that the  $P_{dx}$  estimated above should be scaled to Equation (4.9) before computing the specular and surface roughness parameters.

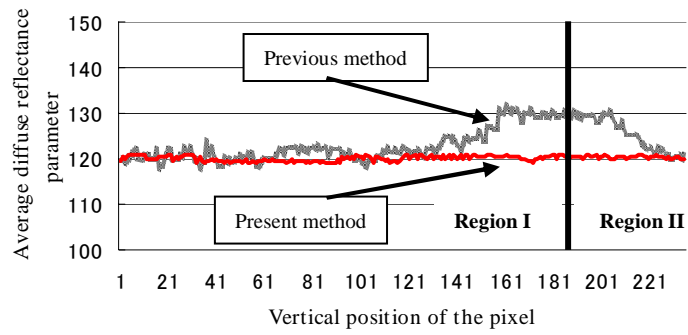
$$\begin{cases} i_{p,sx} \cos \theta_{vx} & = P_{sx} \cdot \exp(-\theta_{rx1}^2/2\sigma_x^2) \\ i_{q,sx} \cos \theta_{vx} & = P_{sx} \cdot \exp(-\theta_{r2}^2/2\sigma_x^2) \end{cases} \quad (4.11)$$

When strong specular reflection is observed less than twice, the specular reflectance and surface roughness parameters cannot be determined, and thus are obtained using a linear interpolation method within a  $W \times W$  window, as described in Chapter 3. If the window is small compared with the area that includes the undetermined reflectance parameters, then the values of the reflectance parameters are interpolated linearly by scanning the texture image horizontally.

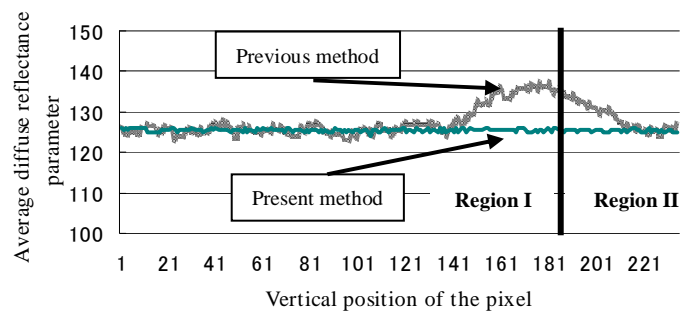
## 4.4. Experimental results

Objects A ~ E, which were used in the previous experiments, are used again for the present experiment. Here, Object E is used in a preliminary experiment to demonstrate that the proposed inverse radiosity method can eliminate the influence of diffuse interreflections. Note that with respect to the window size used in interpolation method,  $W = 5$  is fixed.

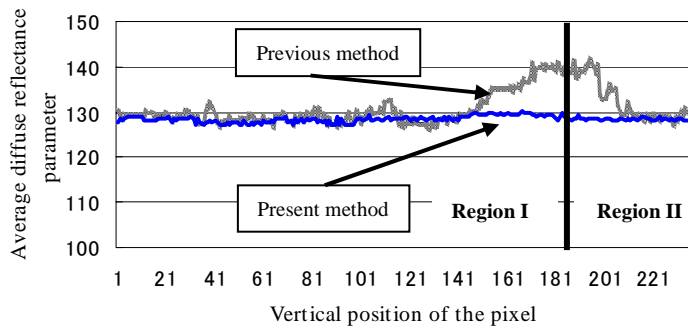
This experiment is conducted in order to confirm the effect of eliminating the influence of interreflections. Object E, having a right-angle fold, is separated into two regions, Regions I and II, as shown in Figure 2.11(a). For this experiment, the two setups described in Section 3.4 were used. The proposed inverse radiosity method was then compared to the previous method [MTY01b, MTY01a, MTY02], described in the Chapter 3, which does not consider interreflections in estimating reflectance parameters. If interreflections occur, when the value estimated by the previous method should be incorrect in that area. The results for diffuse (Setup 1) and specular (Setup 2) surfaces are shown in Figures 4.6 and 4.7, respectively. Each graph represents the RGB channels of the diffuse reflectance parameter estimated by the respective methods. The horizontal axis indicates the position of the surface point in the vertical direction of Object E, and the vertical axis indicates the average diffuse reflectance parameter in the horizontal direction. Figure 4.6 shows that the diffuse reflectance parameters estimated by the previous method are large around the boundary between Regions I and II. In contrast, the diffuse reflectance parameters estimated by the present method are reduced in this area, indicating the effectiveness of the inverse radiosity method. However, a slight influence of interreflections remains for the glossy surface, as can be observed in Figure 4.7, because interreflections due to the specular reflection also occur at the boundary between Regions I and II in Setup 2. The diffuse reflectance parameter obtained by the present method looks smoother than that obtained by the previous method because the diffuse reflectance parameter of a point on the object is calculated as the average of the diffuse reflectance parameters of four patches that share the point.



(a) R channel

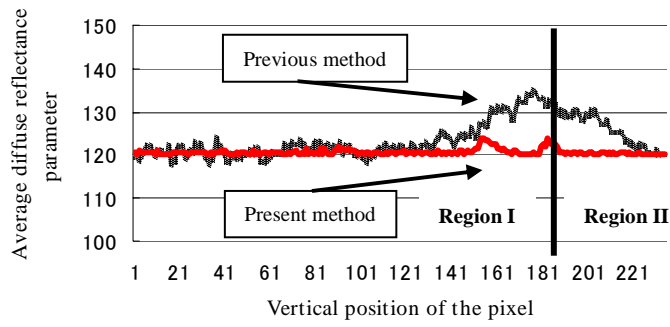


(b) G channel

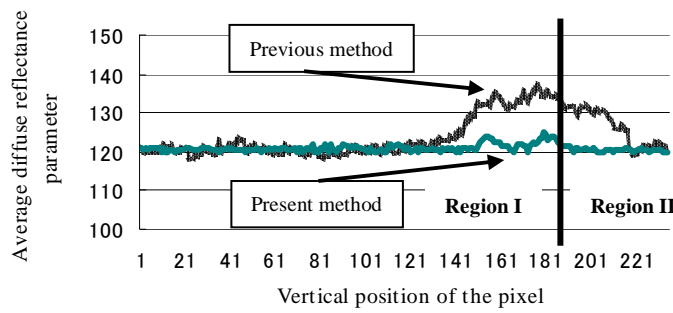


(c) B channel

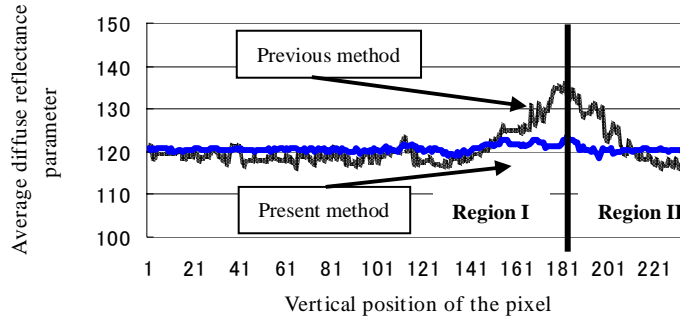
Figure 4.6. Comparison with previous results for Object E with diffuse surfaces.



(a) R channel



(b) G channel



(c) B channel

Figure 4.7. Comparison with previous results for Object E with glossy surfaces.

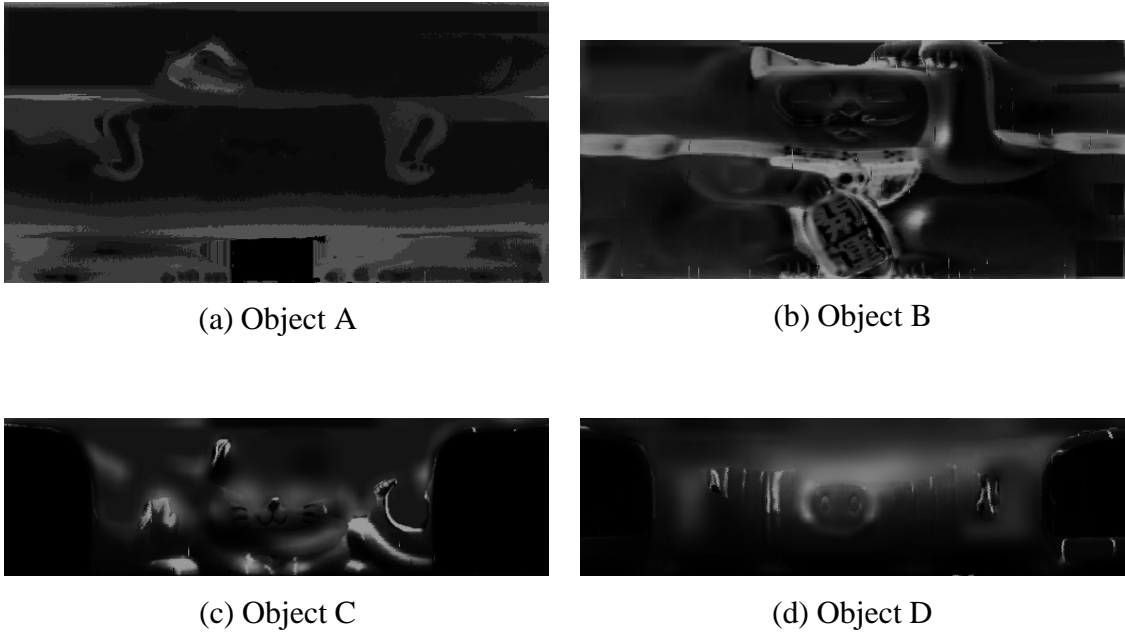


Figure 4.8. Difference between diffuse reflectance parameters estimated with inverse radiosity and those estimated with the method in Chapter 3.

#### 4.4.1 Estimated reflectance parameters

The following experiment was conducted in order to examine the effect of considering interreflections in reflectance parameter estimation of non-uniform objects, i.e., Objects A, B, C and D. Figures 4.8(a) ~ (d) illustrate the sum of the differences in RGB channels of the diffuse reflectance parameters between the previous and present methods. These images are shown in gray-scale using cylindrical coordinates having a maximum value of 255. The difference is large in areas in which interreflections occur, indicating that the present method is effective for objects that have non-uniform surface reflectance properties and exhibit interreflections. Some areas have larger differences than others. For example, the area of the beak of Object A and the arms and legs of Objects B and C have remarkable differences. In the inverse radiosity method, the diffuse reflectance parameter is calculated as the average of four patches, as explained for the preliminary experiments. Therefore, the diffuse reflectance parameter that includes the influence of specular interreflections is also smoothed, and this smoothing process causes a large difference, compared to the previous method.

#### **4.4.2 Rendering results using the radiosity method and the Torrance-Sparrow model**

Finally, the virtual relighting of virtualized objects is demonstrated. Figures 4.9 ~4.12 show the rendering results of virtualized objects (Objects A, B, C and D) under a virtual lighting condition. A virtual light source is rotated around the virtualized object, and the center of rotation is at the center of the object. Each figure shows the movement of the light source from right to left of the object. Each object is fairly rendered under arbitrary virtual illumination conditions without the influence of diffuse interreflections. However, because specular interreflections cannot be removed, complicated areas of Objects C and D contain some highlights compared with other areas. Areas that are surrounded by color squares in Figure 4.13 show different result between the inverse local rendering and the inverse rendering. For example, the diffuse reflection component differs between the left and right images in (a). The rendering result of inverse radiosity rendering shows a reduction in the influence of diffuse interreflections compared to the result of inverse local rendering, and (b) shows that the influence of diffuse interreflections is eliminated.



Figure 4.9. Rendering results for Object A with the Torrance-Sparrow model.



Figure 4.10. Rendering results for Object B with the Torrance-Sparrow model.

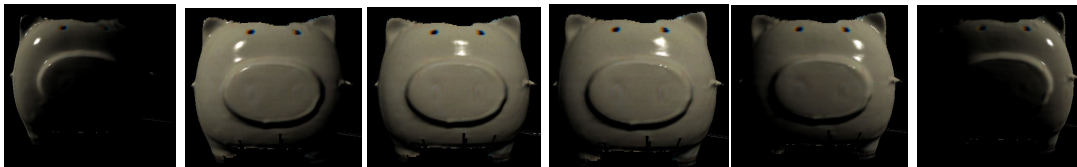


Figure 4.11. Rendering results for Object C with the Torrance-Sparrow model.

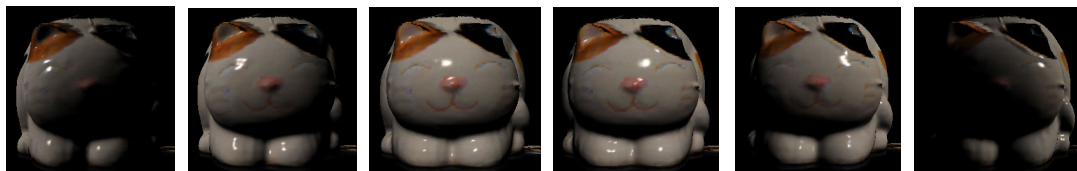
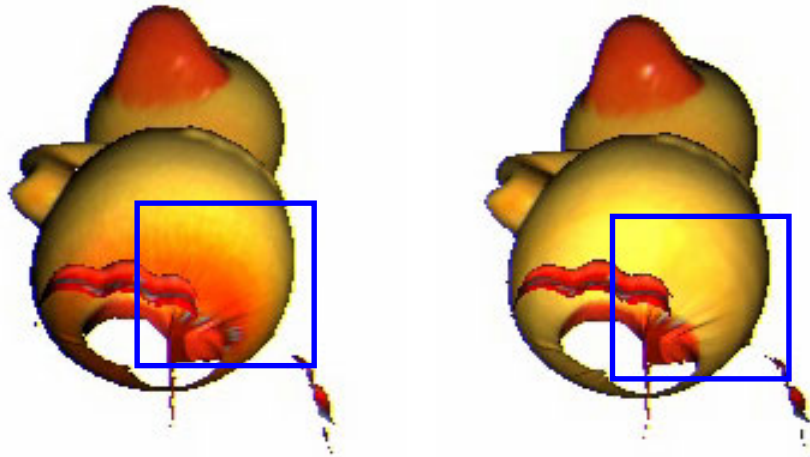


Figure 4.12. Rendering results for Object D with the Torrance-Sparrow model.



Inverse local rendering    Inverse radiosity rendering

(a) Object A



Inverse local rendering



Inverse radiosity rendering

(b) Object B

Figure 4.13. Difference between rendering results based on the inverse radiosity rendering and the inverse local rendering in Chapter 3.

## 4.5. Discussion

Again, the preliminary experiments are discussed, particularly Experimental Setup 2. In Setup 1, it is proved that the inverse radiosity method can remove the influence of diffuse interreflections because the radiosity rendering method can take the diffuse interreflections into account. However, it should be noted that the radiosity rendering method considers only diffuse interreflections. Due to this limitation, in Experimental Setup 2, some errors remain. There are two possible approaches by which to address this problem. The first is based on hybrid rendering, such as the combination of radiosity and ray tracing rendering methods [WCG87, Shi90, Arv86]. This method has a greater computational cost compared to single rendering methods. Therefore, the inverse hybrid rendering method is computationally very expensive for estimating surface reflectance properties and does not provide a solution to the above-mentioned problem. The second method is based on a more efficient rendering method, which can represent both diffuse and specular interreflections, that has recently been developed. The usefulness of such a rendering method has been proven in the field of computer graphics. This method, called the *photon mapping* rendering method [Jen01], is computationally less expensive than the hybrid rendering method.

Moreover, in the inverse radiosity method, the object must be separated into patches for calculation of the form factor. In order to address this problem, the hierarchical construction of patches has been proposed [WEH89]. This method reduces the computational cost by constraining the subdivision of patches according to surface normal. However, a limitation exists in the finite element separation, and the method becomes very costly for complex models and non-diffuse materials. The high cost of this method for complex models is due to the fact that the radiosity algorithm computes values for every patch in the model. Furthermore, the radiosity algorithms represent the solution in a finite mesh, a tessellated representation of the real geometry. The representation is inaccurate if the mesh is not carefully constructed, and, as a result, radiosity algorithms have problems computing sharp features in the illumination. For example, sharp shadow boundaries tend to be blurred. In contrast to radiosity, *photon mapping* rendering does not require the separation of an object into patches. This method is performed using a pixel in the scene image from the camera. Due the nature of this method, lighting effects are physically represented. If inverse photon mapping can be performed, more accurate surface reflectance parameters can be obtained.

## 4.6. Conclusions

In this chapter, a new surface reflectance modeling method was proposed that is based on densely estimating the non-uniform reflectance properties with diffuse interreflections for almost the entire surface of objects using a laser rangefinder in order to virtualize real objects. In this approach, the radiosity rendering method was employed so that diffuse interreflections can be considered when estimating surface reflectance properties. The present method was shown experimentally to be useful for estimating the reflectance parameters of objects with diffuse interreflections that exhibit non-uniform surface reflectance. However, a problem remains with respect to the influence of specular interreflections. Because the radiosity method considers only diffuse interreflections, the reflectance parameters may be influenced by specular interreflections. In order to investigate this possibility, a preliminary experiment was conducted using a simple object. It was confirmed experimentally that if specular interreflections occur, then the estimated parameter contains some errors. In the next chapter, a method for handling the problem of both diffuse and specular interreflections will be introduced. Specifically, a global illumination rendering method called *photon mapping* will be employed, in which all lighting effects in the real world are taken into account. Using this method, faithful diffuse reflectance, specular reflectance and surface roughness parameters will be obtained.

# Chapter 5

## Inverse Photon Mapping for Dense Reflectometry Estimation

### 5.1. Introduction

As described in the previous chapter, the radiosity algorithm is quite efficient at computing the lighting distribution with respect to a simple model with diffuse materials. However, because the radiosity rendering method considers only diffuse interreflections, when object reflectance properties are estimated using the *inverse radiosity rendering*, it is impossible to eliminate the influence of specular interreflections. In addition, computation becomes very costly for complex models and non-diffuse materials. The high computational cost for complex models is due to the fact that the radiosity algorithm computes values for every patch in the model. Furthermore, the radiosity algorithms represent the solution in a finite mesh, and a tessellated representation can be very inaccurate if the mesh is not carefully constructed. Therefore, accurate object geometry and efficient tessellation are required when using the radiosity to estimate surface reflectance properties.

In this chapter, the *photon mapping* rendering method is used to solve the problem with the inverse radiosity rendering method. Using the inverse photon mapping method, both diffuse and specular interreflections on the object surface can be taken into account. Because the photon mapping rendering method does not require tessellated patches, due to its pixel base calculations, the computational cost is low compared with the radiosity rendering method. The photon mapping method is introduced in the

following.

## 5.2. Photon mapping

For rendering both diffuse and specular interreflections, hybrid techniques exist that combine the radiosity and ray-tracing methods. Radiosity is good for treating diffuse reflections, whereas ray tracing is good for treating specular reflections. Hybrid methods use ray tracing to add specular reflections to radiosity [WCG87, Shi90, Arv86, CRMD91, RPV93, ZS95]. However, representing specular reflection requires more sampling rays after radiosity rendering has been applied to the object, which results in a large computational cost.

Photon mapping, on the other hand, involves a different approach from the hybrid techniques. The idea in photon mapping is to change the representation of illumination. Rather than tightly coupling lighting information with the geometry, the lighting information is stored in a separate independent data structure called the *photon map* [Jen01]. The photon map is constructed of photons emitted from the light sources and traced through the reflectance model (i.e. the Torrance-Sparrow model). The photon map contains information about all of the photon hits, and this information can be used to efficiently render the model in a manner similar to that in which the radiosity is used in hybrid techniques. The decoupling of the photon map from the geometry offers a significant advantage in that the representation is not only simplified, but it is also possible to use the structure to represent lighting in very complex models. The combination of photon mapping and a Monte Carlo ray-tracing based rendering algorithm results in an algorithm that is as general as pure Monte Carlo ray tracing but that is significantly more efficient [Kaj86]. In fact, the calculation cost of the Monte Carlo ray-tracing method grows exponentially with respect to the number of rays as the number of reflections increases. For example, if ten rays are used to compute irradiance, and each of these ten rays intersect another diffuse surface, which requires another ten rays to compute the irradiance, and as a result, 100 rays are required in order to compute the diffuse light reflected twice before being seen by the observer.

In the photon mapping rendering method [Jen01], an outgoing radiance  $L$  from a surface point  $x$  is calculated in order to decide the surface color. Figure 5.1 shows the geometrical arrangement for photon mapping rendering. The following equations

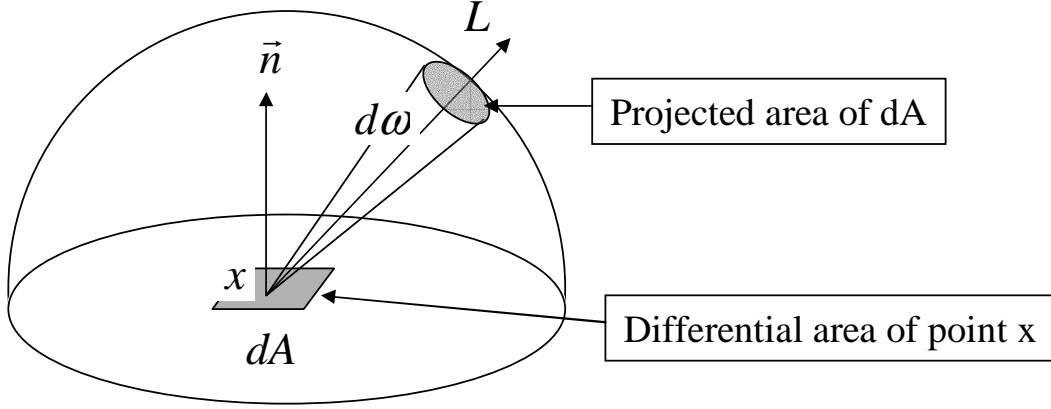


Figure 5.1. Geometrical arrangement for photon mapping rendering.

form the rendering equations in the photon mapping method.

$$L(x, \vec{\omega}) = L^e(x, \vec{\omega}) + L^r(x, \vec{\omega}), \quad (5.1)$$

$$L^r(x, \vec{\omega}) = \int_{\Omega} f(x, \vec{\omega}', \vec{\omega}) L^o(x, \vec{\omega}') (\vec{\omega}' \cdot \vec{n}) d\vec{\omega}', \quad (5.2)$$

$$f(x, \vec{\omega}', \vec{\omega}) = f_s(x, \vec{\omega}', \vec{\omega}) + f_d(x, \vec{\omega}', \vec{\omega}), \quad (5.3)$$

$$L^o(x, \vec{\omega}') = L_l(x, \vec{\omega}') + L_c(x, \vec{\omega}') + L_d(x, \vec{\omega}'), \quad (5.4)$$

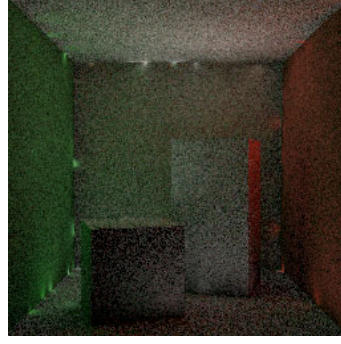
where  $L^e(x, \vec{\omega})$ ,  $L^r(x, \vec{\omega})$ ,  $L^o(x, \vec{\omega}')$  and  $f(x, \vec{\omega}', \vec{\omega})$  represent the emitted radiance, the reflected radiance, the incoming radiance, and a BRDF (i.e. the Torrance-Sparrow model), respectively.  $f_d(x, \vec{\omega}', \vec{\omega})$  and  $f_s(x, \vec{\omega}', \vec{\omega})$  denote the diffuse and specular terms in BRDF, respectively.  $L_l(x, \vec{\omega}')$  represents the direct illumination from the light sources.  $L_c(x, \vec{\omega}')$  is referred to as the *caustics*, which represent the indirect illumination from the light sources via specular reflection or transmission.  $L_d(x, \vec{\omega}')$  denotes the indirect illumination from light sources that have been reflected diffusely at least once. Equations (5.1) ~ (5.4) indicate that the reflected radiance has the following four components.

$$\begin{aligned} L^r(x, \vec{\omega}) &= \int_{\Omega} f(x, \vec{\omega}', \vec{\omega}) L^o(x, \vec{\omega}') (\vec{\omega}' \cdot \vec{n}) d\vec{\omega}' \\ &= \int_{\Omega} f(x, \vec{\omega}', \vec{\omega}) L_l(x, \vec{\omega}') (\vec{\omega}' \cdot \vec{n}) d\vec{\omega}' + \end{aligned} \quad (5.5)$$

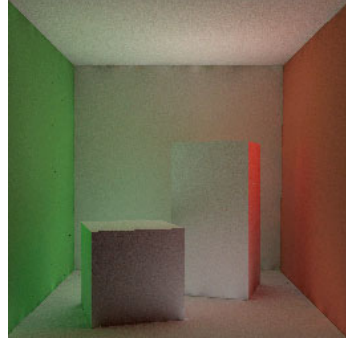
$$\int_{\Omega} f_s(x, \vec{\omega}', \vec{\omega}) (L_c(x, \vec{\omega}') + L_d(x, \vec{\omega}')) (\vec{\omega}' \cdot \vec{n}) d\vec{\omega}' + \quad (5.6)$$



(a) Monte Carlo ray tracing method



(b) Photon mapping method (10,000 photons)



(c) Photon mapping method (100,000 photons)



(d) Photon mapping method (1,000,000 photons)

Figure 5.2. Rendering results of photon mapping.

$$\int_{\Omega} f_d(x, \vec{\omega}', \vec{\omega}) L_c(x, \vec{\omega}') (\vec{\omega}' \cdot \vec{n}) d\vec{\omega}' + \quad (5.7)$$

$$\int_{\Omega} f_d(x, \vec{\omega}', \vec{\omega}) L_d(x, \vec{\omega}') (\vec{\omega}' \cdot \vec{n}) d\vec{\omega}', \quad (5.8)$$

where Equations (5.5)~(5.8) represent the direct illumination, specular and glossy reflection, caustics and multiple diffuse reflections terms, respectively. This equation is used whenever the reflected radiance from a surface is computed. Figure 5.2 shows the rendering results obtained using the Monte Carlo ray tracing method and the photon mapping method. In (a), the rendering result has some noise due to the small number of rays cast. On the other hand, in (b) ~ (d), the greater the number of distributed photons, the lower the sampling noise level. Based on these results, the photon mapping

method can efficiently render the virtual image.

### 5.3. Estimation of surface reflectance parameters considering both diffuse and specular interreflections

Here, the outgoing radiance  $L$  in Equation (5.1) is equivalent to the reflected radiance  $L^r$  due to the assumption that the underlying objects have no emissions. Equations (5.1) and (5.2) are theoretical models. Using Equation (2.9), the color  $\hat{i}_x$  at surface point  $x$  is represented by the following equation, which is referred to as the Ward reflectance model [War92]:

$$\begin{aligned}\hat{i}_x &= I_x \left\{ \frac{P_{dx}}{\pi} + P_{sx} \frac{\exp(-\tan^2 \theta_{rx} / \sigma_x^2)}{4\pi \sigma_x^2} \right\} \\ &= I_x \left\{ \frac{P_{dx}}{\pi} + P_{sx} K(\theta_{vx}, \theta_{rx}, \sigma_x) \right\},\end{aligned}\tag{5.9}$$

where  $I_x$  is the incoming radiance.  $K(\theta_{vx}, \theta_{rx}, \sigma_x)$  denotes the specular term in Equation (2.12), and the other parameters are the same as in Equation (2.12). In practice, the Ward model described above has five parameters for representing anisotropic object surface reflectance properties. Because the object is assumed to have isotropic reflectance properties, there are three unknown parameters: the diffuse reflectance, the specular reflectance and the surface roughness parameters.  $I_x$  is decided by counting the number of photons that arrive at the point  $x$ . The photon is specifically traced using a Monte Carlo ray tracing method [Kaj86]. In this case, the photon is reflected or absorbed according to the reflectance parameters, and only the photon that is reflected is traced iteratively.

Figure 5.3 shows the flow diagram of the present method. This figure illustrates process (D) in Figure 2.1 as described in Chapter 2. As an initial estimation, the reflectance parameters are obtained using a previous method based on *inverse radiosity rendering* [MY02b, MY02a] in Figure 5.3(a). In this preprocessing, the diffuse reflectance parameter is estimated based on the inverse radiosity in order to consider diffuse interreflections. The specular reflectance and the surface roughness parameters are estimated based on the inverse local rendering (i.e. the Torrance-Sparrow model) with no consideration of specular interreflections. Here, let  $P_{dx}^{init}$ ,  $P_{sx}^{init}$  and  $\sigma_x^{init}$  be the

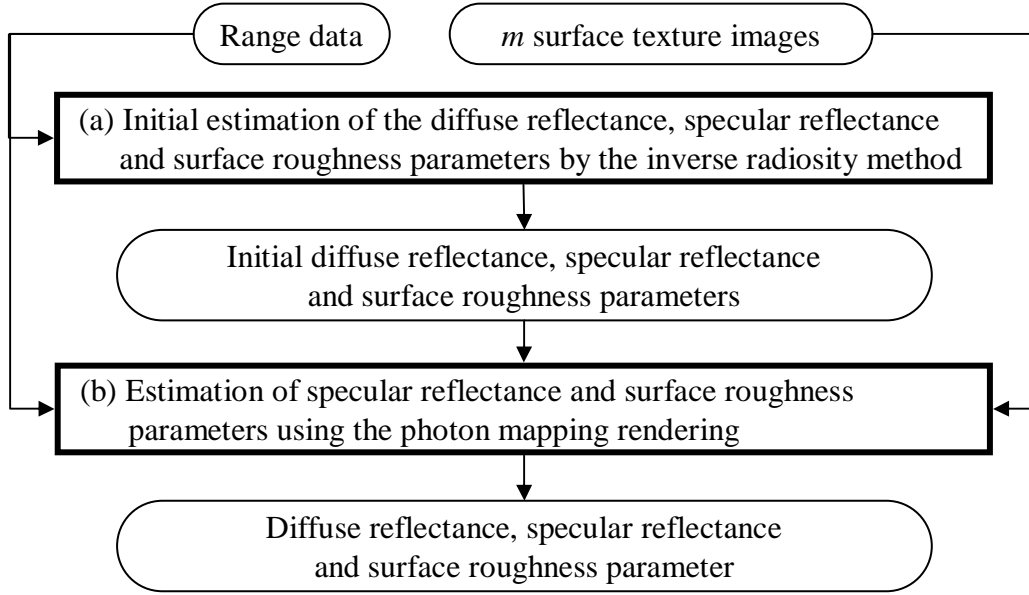


Figure 5.3. Flow diagram for the estimation of surface reflectance properties based on inverse photon mapping.

reflectance parameters obtained in this process. These parameters are used as initial parameters for the next process (b) in Figure 5.3.

Figure 5.4 illustrates the details of the iterative reflectance estimation process based on inverse photon mapping in Figure 5.3 (b). In the following, the details of reflectance parameter estimation are described.

The reflectance parameter estimation method based on inverse photon mapping is separated into two processes, (a) and (b), shown in Figure 5.4. The first process is for the diffuse reflectance parameter estimation ((a) in Figure 5.4), and the second process is for the estimation of the specular reflectance and surface roughness parameters ((b) in Figure 5.4). These processes are performed iteratively. In each process, the following equation, which is derived from Equation (5.9), is minimized at each pixel in the texture image:

$$E(P_{dx}, P_{sx}, \sigma_k) = \sum_{p=1}^j (i_{px} - \widehat{i}_{px})^2,$$

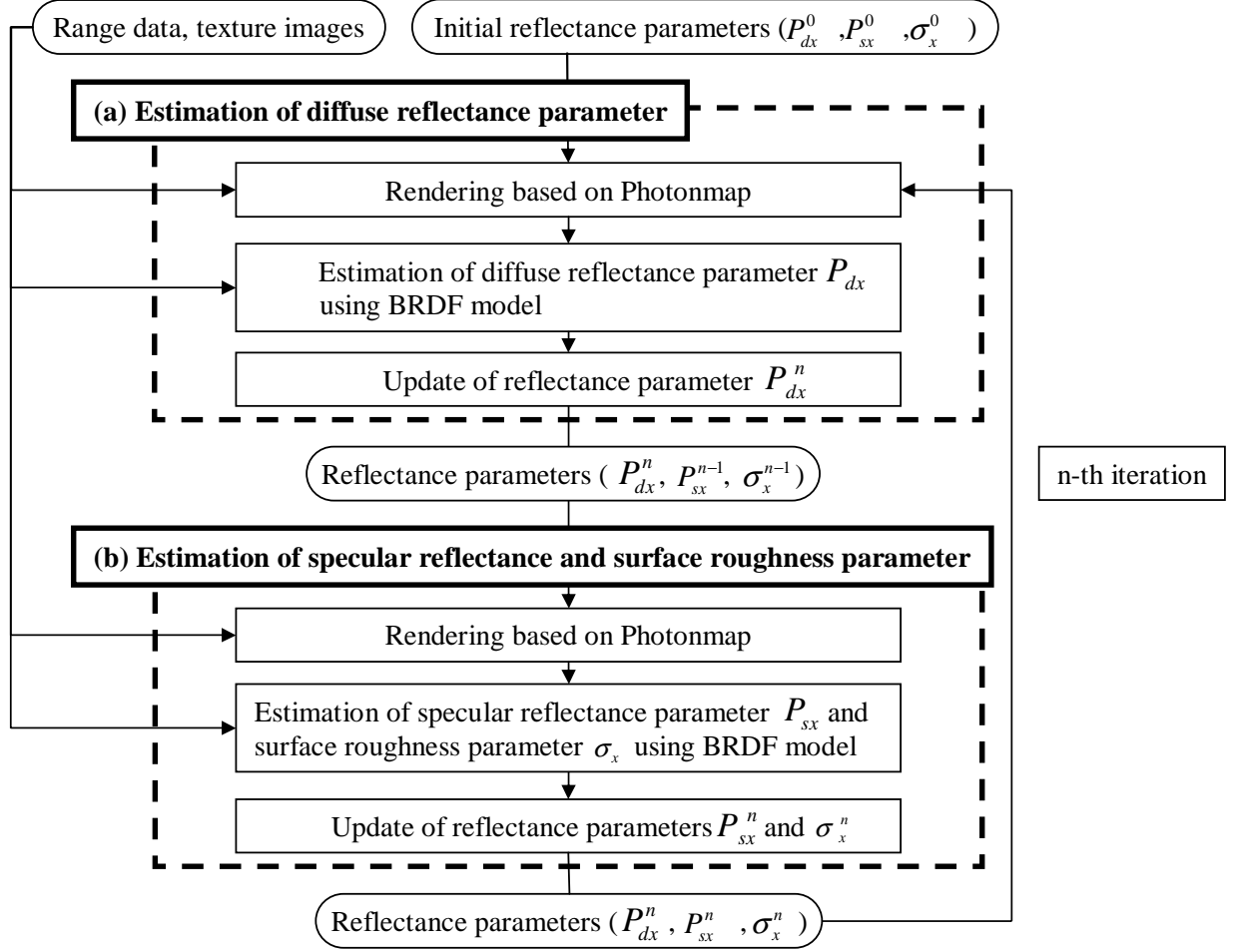


Figure 5.4. Detail of reflectance estimation process based on inverse photon mapping.

$$= \sum_{p=1}^j (L_x - \frac{P_{dx}}{\pi} I_x - P_{sx} K(\theta_{vx}, \theta_{rx}, \sigma_x) I_x)^2, \quad (5.10)$$

where  $i_{px}$  is the measured radiance (color intensity) at surface point  $x$  with light source position  $p$ ,  $\widehat{i_{px}}$  is the irradiance that is computed from Equation (5.9) at surface point  $x$  with light source position  $p$ , and  $j$  denotes the number of selected light positions at surface point  $x$  in categories  $T_{diff}$ ,  $T_{spec}$  and  $T_{none}$  among the selected light positions  $m$ .

In process (a), the diffuse reflectance parameter  $P_{dx}$  is estimated using a pixel that is categorized as  $T_{diff}$ .  $P_{dx}^{init}$ ,  $P_{sx}^{init}$  and  $\sigma_x^{init}$  are used to compute  $\widehat{i_{px}}$  only at the first

iteration. Here, the specular reflection term in Equation (5.9),  $I_x P_{sx} K(\theta_{vx}, \theta_{rx}, \sigma_x)$ , is set to be 0 because the specular reflection cannot be observed.

In process (b), the specular reflectance  $P_{sx}$  and the surface roughness  $\sigma_x$  parameters are estimated using only pixels that are categorized as  $T_{spec}$  or  $T_{none}$ .  $P_{sx}^{init}$  and  $\sigma_x^{init}$  are again used to compute  $\widehat{i_{px}}$  only at the first iteration. The  $P_{dx}$  estimated above is used in Equation (5.9). When  $P_{sx}$  and  $\sigma_x$  are estimated, the value of each reflectance parameter is updated, and processes (a) and (b) are iterated  $th_2$  times. The reflectance parameter is selected when differences between the real and synthetic images is the minimum value among  $th_2$  samples. Because this is a non-linear equation with unknown parameters, the photon mapping rendering and estimation of surface reflectance parameters is performed iteratively, and the difference between the real image and the synthesized image is minimized (Equation (5.10)). A number of methods can be used to minimize this equation, and the downhill simplex method is selected for this problem [BG01].

After the estimation process is complete, the specular reflectance and the surface roughness parameters may not be correct, if the specular reflection component is exceedingly small. Such parameters are interpolated linearly by scanning the texture image horizontally.

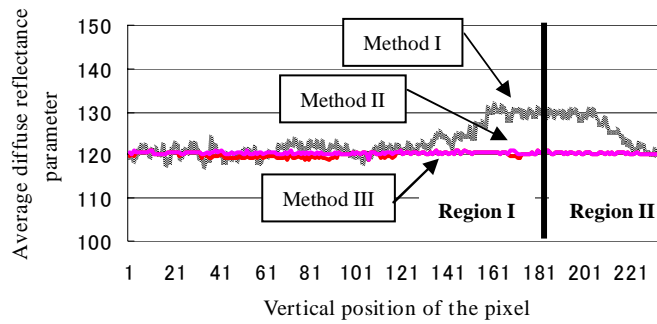
## 5.4. Experimental results

In Chapter 3 and 4, two methods of inverse reflectometry (hereinafter referred to as Method I and Method II) were proposed. In the following, using Object E, the reflectance parameters estimated using the present method (hereafter referred to as Method III) are compared with those obtained by Methods I and II. The effect of considering interreflections in surface reflectance parameter estimation is then examined using Objects A ~ D with uniform and non-uniform surface properties. Finally, rendered images are obtained based on reflectance parameters estimated using Method III. See Figure 2.11 and 3.12 for the test objects used in these experiments.

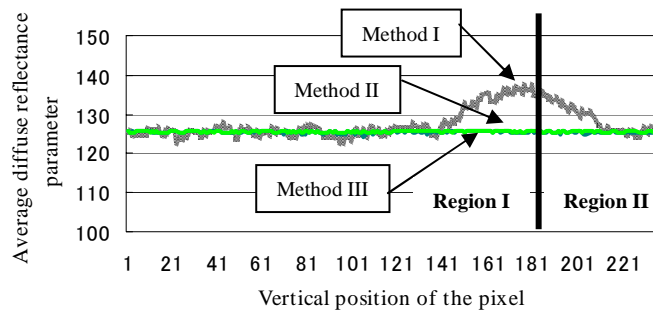
A standard PC (Pentium 4, 3.06 GHz, memory: 2 GB) is used in the following experiments. The number of photons is 2 million, and the proposed algorithm requires approximately four hours to estimate the reflectance parameters of each object. The threshold is fixed at  $th_2 = 50$ .

### 5.4.1 Preliminary experiments

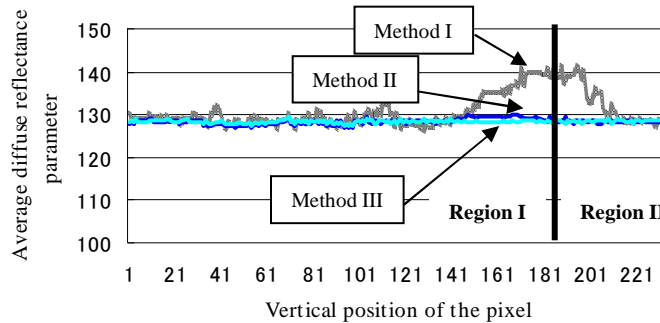
The performance of the present method was demonstrated in preliminary experiments using a simple object (Object E). In particular, Method III was compared with Methods I (which does not consider interreflections, as described as in Chapter 3) and II (which considers only diffuse interreflections, as described as in Chapter 4). Object E consists of two plates (Regions I and II) situated at a 90-degree angle with respect to each other. The same two experimental setups described in Section 3.4 were used, and the results are shown in Figure 5.5 for Setup 1 and in Figure 5.6 for Setup 2. Each graph represents the RGB channels of the diffuse reflectance parameter estimated by the three methods. The horizontal axis represents the position of the pixel along the vertical direction of the object, and the vertical axis represents the average diffuse reflectance parameter along the horizontal direction of the object. In Methods I and II, the value of the diffuse reflectance parameter is large around the boundary between Regions I and II due to the influence of interreflections. However, in Method III, the estimated parameter is more stable, indicating that Method III can eliminate the influence of both diffuse and specular interreflections.



(a) R channel

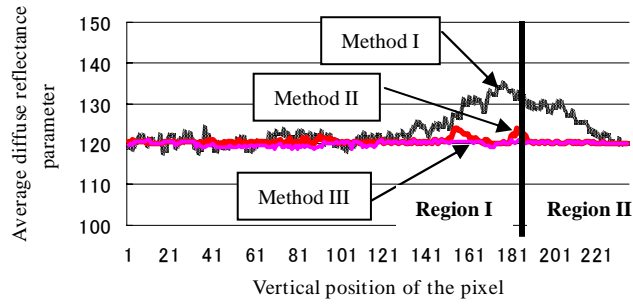


(b) G channel

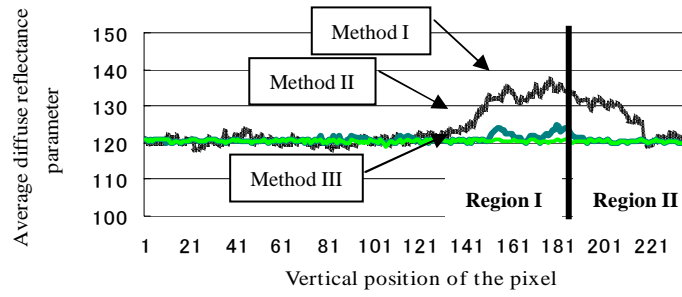


(c) B channel

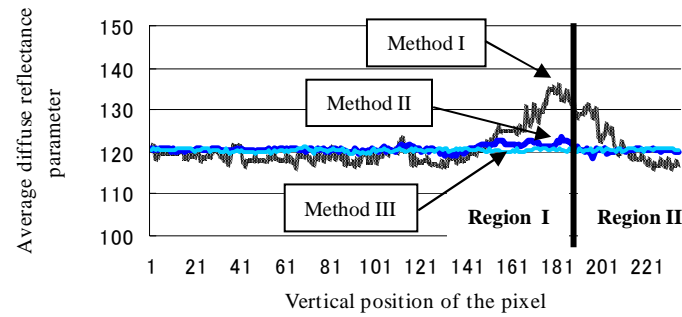
Figure 5.5. Comparison of the three proposed methods for Object E with diffuse surfaces.



(a) R channel



(b) G channel



(c) B channel

Figure 5.6. Comparison of the three proposed methods for Object E with glossy surfaces.

## 5.4.2 Estimated reflectance parameters

In the next experiment, Objects A ~ D, shown in Figures 2.11, were used. These objects have non-uniform or uniform diffuse and specular reflectance properties. The computational times for these methods are listed in Table 5.1. The *inverse photon mapping rendering* takes longer to estimate the surface reflectance properties than Methods I or II. This is because rendering the object image based on estimated reflectance parameters requires a great deal of time.

Table 5.1. Comparison of computational costs of the three proposed methods.

Object	Method	Computational Time [h:m]
A	Method I	0:20
	Method II	3:32
	Method III	4:39
B	Method I	0:26
	Method II	3:51
	Method III	4:58
C	Method I	0:23
	Method II	3:11
	Method III	4:43
D	Method I	0:18
	Method II	2:34
	Method III	4:21

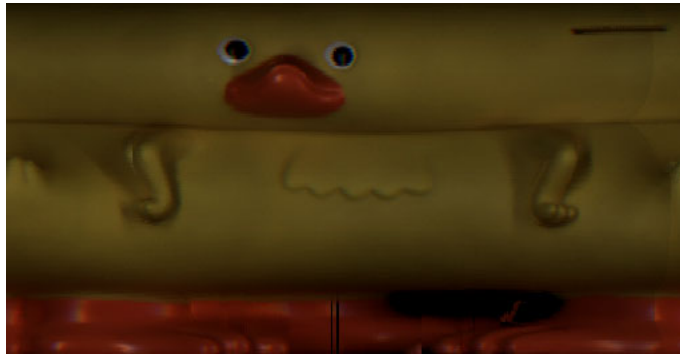
Figure 5.7 ~ 5.10 show the cylindrical images of real objects and the difference images between real and synthetic images (rendered by photon mapping) for Methods II and III for each test object (Objects A ~ D), respectively. The light position is located at the top of the rangefinder. Synthetic images are rendered using estimated reflectance parameters under the illumination conditions used for the real images. Note that linear interpolation is conducted when the specular reflectance and the surface roughness parameters cannot be estimated due to an exceedingly small specular reflection value. In Method II, the error due to the influence of specular interreflections is confirmed. In particular, Objects A and B exhibit large errors at the areas showing inequalities

Table 5.2. Average and variance of differences between real and synthetic images.

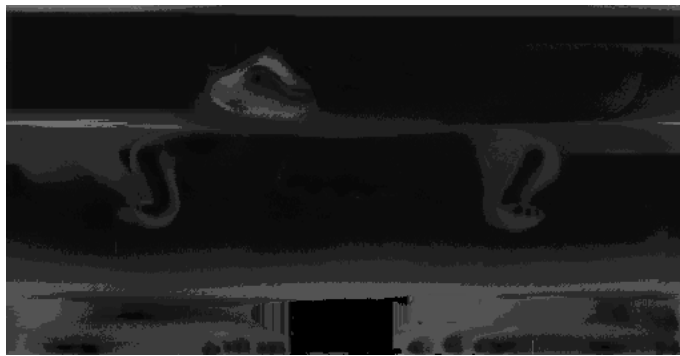
		Object A	Object B	Object C	Object D
Average	Method II	17.7	20.1	8.7	13.3
	Method III	1.11	1.06	0.51	0.92
Variance	Method II	501.9	485.4	493.3	375.2
	Method III	6.8	8.0	3.2	9.8

(i.e., the cat's leg and neck, and the pig's nose). Method III is not affected by such influences. In addition, Table 5.2 shows the variance of differences between real and synthetic images. Method III has much smaller variances than Method II for all of the objects. These results show that Method III can accurately estimate each reflectance parameter, even if diffuse and specular interreflections occur.

Figure 5.11 shows the relationship between the iterated process and the differences between real and synthetic images. The vertical axis indicates the sum of differences between the real and synthetic images, and the horizontal axis indicates the number of iterations. Each graph shows that the iterated estimation process decreases the difference between real and synthetic images. However, the minimum difference may not be the global minimum because the proposed iteration method ends when the number of iterations reaches 50. Therefore, each graph illustrates pulsation of the differences. In other words, the higher the number of iterations, the lower the differences. In this experiment, the reflectance parameters of each object is determined when the number of iterations are 34, 32, 39 and 35, respectively.



(a) Real image



(b) Difference between real and synthetic images for Method II



(c) Difference between real and synthetic images for Method III

Figure 5.7. Differences between real and synthetic cylindrical images for Object A.



(a) Real image



(b) Difference between real and synthetic images for Method II



(c) Difference between real and synthetic images for Method III

Figure 5.8. Differences between real and synthetic cylindrical images for Object B.



(a) Real image



(b) Difference between real and synthetic images for Method II



(c) Difference between real and synthetic images for Method III

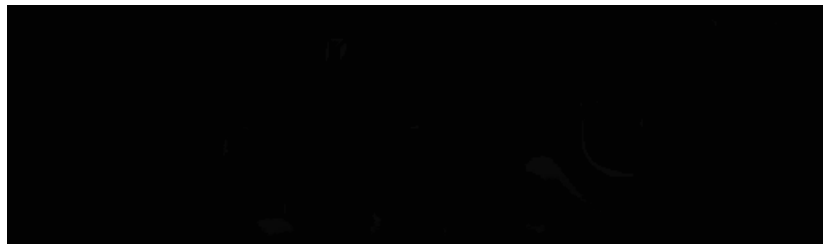
Figure 5.9. Differences between real and synthetic cylindrical images for Object C.



(a) Real image

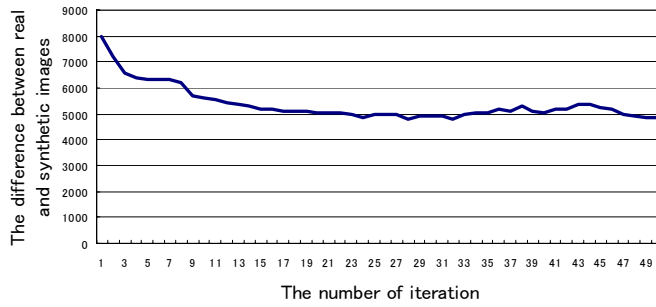


(b) Difference between real and synthetic images for Method II

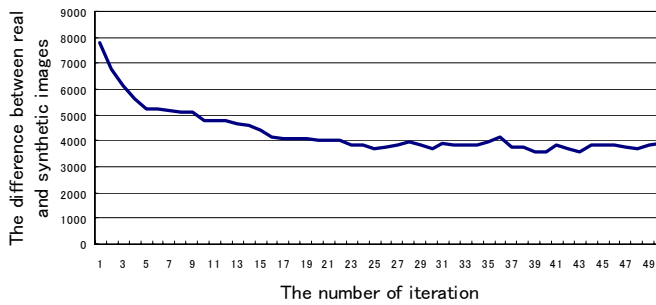


(c) Difference between real and synthetic images for Method III

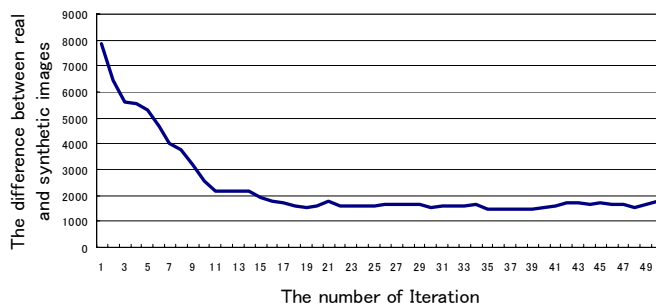
Figure 5.10. Differences between real and synthetic cylindrical images for Object D.



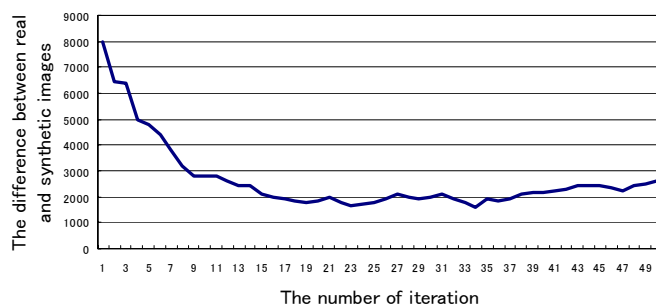
(a) Object A



(b) Object B



(c) Object C



(c) Object D

Figure 5.11. Relationship between the number of iterations and difference between real and synthetic images for Objects A ~ D.

### 5.4.3 Rendering results obtained using the photon mapping method

Figure 5.12 shows rendered images of Objects A ~ D based on reflectance parameters estimated using the *inverse photon mapping rendering*. Although these images are photorealistically rendered, some errors remain with respect to the geometry. For example, some areas of the duck's legs (a) are not rendered, and spike noise can be observed around the cat's legs (c). These errors are due to noise in the range images. In order to solve this problem, it is necessary to interpolate the range data using the data around these areas.



(a) Rendering results for Object A



(b) Rendering results for Object B



(c) Rendering results for Object C



(c) Rendering results for Object D

Figure 5.12. Rendering results for Object A ~ D under arbitrary illumination conditions.

## 5.5. Discussion

Inverse photon mapping rendering has efficiently estimated the object surface reflectance properties. However, the method has a problem with respect to computational time. This problem is due to the time consumed by the photon mapping rendering. Although photon mapping is faster than other global illumination rendering methods, the amount of time required is still too great for rendering images by a standard PC. There are two approaches by which to solve this problem.

The first involves simply implementing and calculating the photon mapping rendering algorithm on fast graphics hardware (GPU). Recently, the photon mapping rendering by such methods has been reported to be much faster than calculation by CPU[PDC<sup>+</sup>03, PBMH02]. Using these methods, the inverse photon mapping rendering will be efficiently calculated.

In the second approach, the photon map is rendered only at the areas in which the surface reflectance properties vary. In inverse photon mapping rendering, the entire object surface is rendered in each iteration process. However, the areas at which the reflectance parameters do not change need not be re-rendered. In order to address this problem, in areas where the photon map does not change, the radiance of the previously estimated area is used as a radiance cache. Although this algorithm causes some errors in the reflectance parameter, the degree of trade-off between accuracy and real-time calculation can be controlled.

## 5.6. Conclusions

In this chapter, a new method has been proposed for densely estimating the non-uniform reflectance properties of real objects based on the inverse global rendering technique. The photon mapping rendering method has been proposed in order to solve the inverse rendering equations. Using the proposed method, the reflectance parameters of objects having either uniform or non-uniform surface reflectance properties and both diffuse and specular interreflections can be estimated. In order to verify the present method, a preliminary experiment was conducted and the present method was shown to be able to remove the influence of both diffuse and specular interreflections. In addition, an experiment was conducted using real objects having uniform

or non-uniform reflectance properties and interreflections. The inverse photon mapping rendering was shown to be able to estimate object reflectance parameters with no influence due to either diffuse or specular interreflections. In future research, the proposed method will be improved in order to efficiently calculate the creation of the photon map, and the computational cost will be reduced by using a GPU. The present method can be applied to mixed-reality applications if it works in real time. In addition, the present method will be applied to an anisotropic surface. Although the objects examined herein had isotropic surface reflectance, applying the present method to an anisotropic surface reflectance should be possible by simply modifying the local illumination model used in this chapter.

# Chapter 6

## Conclusions

The objective of the present study was to develop a new surface reflectance modeling method that can densely estimate non-uniform reflectance properties for almost the entire object surface using a laser rangefinder for virtualizing real objects.

Multiple light source positions around the laser rangefinder were automatically selected, so that both diffuse and specular reflection components were observed densely. The proposed approach was shown experimentally to discriminately observe the diffuse and specular reflection components on the object surface. However, even when using the proposed approach, observing both reflection components over the entire surface of an object is difficult. Therefore, the lighting conditions in the scene must be planned in order to observe the reflection components densely.

Three methods were proposed for surface reflectance estimation based on the *inverse rendering* framework without the assumption of uniform object surface reflectance properties:

- the inverse local rendering method,
- the inverse radiosity method, and
- the inverse photon mapping method.

The first approach is based on the inverse local rendering method, in which the Torrance-Sparrow model is employed as a local illumination model, and the data of range and multiple images obtained by the proposed light selection method are fitted on the Torrance-Sparrow model. The surface reflectance parameters are then estimated.

In order to verify the applicability of the proposed inverse local rendering method, an experiment was conducted in order to show that the reflectance parameters can be estimated at each object point for objects with non-uniform reflectance properties. In addition, the influence of interreflections revealed the need for estimation considering interreflections.

The second and third approaches are based on the inverse global rendering method for solving the problem involved in the inverse local rendering (i.e. interreflections). In the second approach, the radiosity rendering method, which can represent diffuse interreflections, was employed. This method can also be used to estimate non-uniform surface reflectance properties using multiple images obtained based on the light selection method. The advantage of the proposed method is the elimination of diffuse interreflections. However, the problem concerning the influence of specular interreflections remains.

In the third approach, the photon mapping method, which can represent all of the lighting effects in the real world, is employed. This rendering method is rapid and has low memory cost compared to other global illumination rendering methods. Unlike the radiosity rendering method, this method is independent of the complexity of the object geometry. Therefore, the inverse photon mapping method can be applied to objects with various reflectance properties. Experiments have shown that the third method exhibits the best performance among the three methods proposed in this study. The advantage of the inverse photon mapping method is that not only diffuse interreflections but also specular interreflections are considered in reflectometry estimation. As a result, the estimated parameters can be obtained without the influence of both interreflections.

In future studies, the following items will be investigated further:

- Light planning in observing the object surface reflection component.
- Automatic estimation of scene lighting conditions.
- Real-time estimation using graphics hardware.

The first item can improve the light selection method so as to observe both object surface reflection components more accurately and densely. The second item helps to merge the virtual and virtualized objects into the real world. Because the proposed

method can be used to estimate object reflectance parameters, faithfully representing the object is easy if the lighting condition is known. The third item is concerned with rapid estimation by implementing the algorithm on high-speed graphics hardware (GPU). Photon mapping rendering has already been implemented on GPUs in other studies. Therefore, using these methods, the proposed estimation processes can be performed in real time. Real-time estimation is extremely useful in the fields of computer vision and graphics. If the three above-described items are achieved, the proposed technique can be practically applied to a number of fields, such as mixed reality.



# References

- [Arv86] J. Arvo, "Backward Ray Tracing," *Proc. ACM SIGGRAPH '86 Seminar Notes*, 1986.
- [Azu97] R. T. Azuma, "A Survey of Augmented Reality," *Presence*, Vol. 6, No. 4, pp. 355-385, 1997.
- [BG01] S. Boivin and A. Gagalowicz, "Image-Based Rendering of Diffuse, Specular and Glossy Surfaces from a Single Image," *Proc. ACM SIGGRAPH '01*, pp. 107-116, August 2001.
- [BH85] M. J. Brooks and B. K. P. Horn, "Shape and Source from a Single Image," *Proc. Int. Joint Conf. on Artificial Intelligence*, pp. 932-936, 1985.
- [BRG92] R. Baribeau, M. Rioux and G. Godin, "Color Reflectance Modeling Using a Polychromatic Laser Sensor," *IEEE Trans. on Pattern Analysis and Machine Intelligence*, Vol. 14, No. 2, pp. 263-269, 1992.
- [CG85] M. F. Cohen and D. P. Greenberg, "The Hemi-Cube: A Radiosity Solution for Complex Environments," *Proc. ACM SIGGRAPH '85*, pp. 31-40, 1985.
- [CGIB86] M. F. Cohen, D. P. Greenberg, D. S. Immel and P. J. Brock, "An Efficient Radiosity Approach for Realistic Image Synthesis," *IEEE Trans. on Computer Graphics and Application*, Vol. 6, No. 3, pp. 26-35, 1986.
- [Che95] E. Chen, "QuickTime VR - An Image-based Approach to Virtual Environment Navigation," *Proc. ACM SIGGRAPH '95*, 1995.

- [Coo86] R. L. Cook, "Stochastic Sampling in Computer Graphics," *ACM Trans. on Graphics*, Vol. 5, No. 1, pp. 51-72, 1986.
- [CPC84] R. L. Cook, T. Porter and L. Carpenter, "Distributed Ray Tracing," *Proc. ACM SIGGRAPH '84*, pp. 137-145, 1984.
- [CRMD91] S. E. Chen, H. E. Rushmeier, G. Miller and T. D. DeRose, "A Progressive Multipass Method for Global Illumination," *Proc. ACM SIGGRAPH '91*, pp. 165-174, 1991.
- [CSSD96] P. H. Christensen, E. J. Stollnitz, D. H. Salesin and T. D. DeRose, "Global Illumination of Glossy Environments Using Wavelets and Importance," *ACM Trans. on Graphics*, Vol. 15, No. 1, pp. 37-71, 1996.
- [DM96] P. E. Debevec and C. J. Malik, "Modeling and Rendering Architecture from Photographs: A Hybrid Geometry- and Image-based Approach," *Proc. ACM SIGGRAPH '96*, pp. 11-20, 1996.
- [DM03] D. Samaras and D. Metaxas, "Incorporating Illumination Constraints in Deformable Models for Shape from Shading and Light Direction Estimation," *IEEE Trans. on Pattern Analysis and Machine Intelligence*, Vol. 25, No. 2, pp. 247-264, 2003.
- [DYB98] P. Debevec, Y. Yu and G. Borshukov, "Efficient View-dependent Image-based Rendering with Projective Texture-mapping," *Proc. Eurographics Workshop on Rendering*, pp. 105-116, 1998.
- [FGR93] A. Fournier, A. S. Gunawan and C. Romanzin, "Interactive Common Illumination for Computer Augmented Reality," *Proc. Int. Conf. on Graphics Interface (GI1993)*, pp. 254-262, May 1993.
- [FvDFH93] James Foley, Andries van Dam, Steven Feiner and John Hughes, *Computer Graphics Principles and Practice*, Addison-Wesley Publishing Company, 2nd edition, 1993.
- [HA93] D. Hougen and N. Ahuja, "Estimation of the Light Source Distribution and Its Use in Integrated Shape Recovery from Stereo and Shading," *Proc. IEEE Int. Conf. Computer Vision (ICCV1993)*, pp. 148-155, 1993.

- [Hor90] B. K. P. Horm, "Height and Gradient from Shading," *Int. Journal of Computer Vision*, Vol. 5, No. 1, pp. 584-595, 1990.
- [ICG86] D. S. Immel, M. F. Cohen and D. P. Greenberg, "A Radiosity Method for Non-diffuse Environments," *Proc. ACM SIGGRAPH '86*, pp. 133-142, 1986.
- [IS91] K. Ikeuchi and K. Sato, "Determining Reflectance Properties of an Object Using Range and Brightness Images," *IEEE Trans. on Pattern Analysis and Machine Intelligence*, Vol. 13, No. 11, pp. 1139-1153, 1991.
- [Jen95] H. W. Jensen, "Importance Driven Path Tracing Using the Photon Map," *Proc. Eurographics Rendering Workshop*, pp. 326-335, 1995.
- [Jen01] H. W. Jensen, *Realistic Image Synthesis Using Photon Mapping*, A K Peters, Ltd, 1st edition, 2001.
- [Kaj86] J. T. Kajiya, "The Rendering Equation," *Proc. ACM SIGGRAPH '86*, pp. 143-150, August 1986.
- [KC94] G. Kay and T. Caelli, "Inverting an Illumination Model from Range and Intensity Maps," *CVGIP: Image Understanding*, Vol. 59, No. 2, pp. 183-201, 1994.
- [LDR00] C. Loscos, G. Drettakis and L. Robert, "Interactive Virtual Relighting of Real Scenes," *IEEE Trans. Visualization and Computer Graphics*, Vol. 6, No. 4, pp. 289-305, December 2000.
- [LF94] S. Laveau and O. Faugeras, "3-D Scene Representation as a Collection of Images," *Proc. Int. Conf. on Pattern Recognition (ICPR1994)*, pp. 689-691, 1994.
- [LH96] M. Levoy and P. Hanrahan, "Light Field Rendering," *Proc. ACM SIGGRAPH '96*, pp. 31-42, 1996.
- [LL95] J. Lu and J. Little, "Reflectance Function Estimation and Shape Recovery from Image Sequence of a Rotating Object," *Proc. 5th IEEE Int. Conf. on Computer Vision*, pp. 80-86, June 1995.

- [LL99a] S. Lin and S. W. Lee, "A Representation of Specular Appearance," *Proc. 7th IEEE Int. Conf. on Computer Vision*, Vol. 2, pp. 849-854, 1999.
- [LL99b] S. Lin and S. W. Lee, "Estimation of Diffuse and Specular Appearance," *Proc. 7th IEEE Int. Conf. on Computer Vision*, Vol. 2, pp. 855-860, 1999.
- [LLSS03] H. P. A. Lensch, J. Lang, A. M. Sa and H. P. Seidel, "Planned Sampling of Spatially Varying BRDFs," *Proc. Eurographics '03*, pp. 473-482, 2003.
- [LR85] C. H. Lee and A. Rosenfeld, "Improved Methods of Estimating Shape from Shading Using the Light Source Coordinate System," *Proc. Int. Joint Conf. on Artificial Intelligence*, Vol. 26, pp. 125-143, 1985.
- [LW95] E. P. Lafoune and Y. D. Willems, "A 5D Tree to Reduce the Variance of Monte Carlo Ray Tracing," *Proc. Eurographics Rendering Workshop*, pp. 11-20, 1995.
- [MB95] L. McMillan and G. Bishop, "Plenoptic Modeling: An Image-based Rendering System," *Proc. ACM SIGGRAPH '95*, 1995.
- [MMMS01] Y. Mukaigawa, H. Miyaki, S. Mihashi and T. Shakunaga, "Photometric Image-Based Rendering for Image Generation in Arbitrary Illumination," *Proc. 8th IEEE Int. Conf. on Computer Vision*, pp. 643-649, July 2001.
- [MTY01a] T. Machida, H. Takemura and N. Yokoya, "Dense Estimation of Surface Reflectance Parameters by Selecting Optimum Illumination Conditions," *Proc. 14th Int. Conf. on Vision Interface (VI2001)*, pp. 244-251, June 2001.
- [MTY01b] T. Machida, H. Takemura and N. Yokoya, "Dense Estimation of Surface Reflectance Parameters from Registered Range and Color Images by Determining Illumination Conditions," *Proc. SPIE Electronic Imaging*, pp. 127-134, January 2001.
- [MTY02] T. Machida, H. Takemura and N. Yokoya, "Dense Estimation of Surface Reflectance Properties for Merging Virtualized Objects into Real Images," *Proc. 5th Asian Conf. on Computer Vision (ACCV2001)*, pp. 688-693, January 2002.

- [MY02a] T. Machida and N. Yokoya, "Dense Estimation of Surface Reflectance Properties of Objects with Interreflections," *Proc. 16th IEEE Int. Conf. on Pattern Recognition (ICPR2002)*, pp. 348-351, August 2002.
- [MY02b] T. Machida and N. Yokoya, "Virtualizing Real Objects with Surface Interreflections," *Proc. IEEE Int. Conf. on Multimedia and Expo (ICME2002)*, pp. 833-836, August 2002.
- [MYT03] T. Machida, N. Yokoya and H. Takemura, "Surface Reflectance Modeling of Real Objects with Interreflections," *Proc. 9th IEEE Int. Conf. on Computer Vision (ICCV2003)*, pp. 170-177, October 2003.
- [PBMH02] T. J. Purcell, I. Buck, W. R. Mark and P. Hanrahan, "Ray Tracing on Programmable Graphics Hardware," *ACM Trans. on Graphics*, pp. 703-712, 2002.
- [PDC<sup>+</sup>03] T. J. Purcell, C. Donner, M. Cammarano, H. W. Jensen and P. Hanrahan, "Photon Mapping on Programmable Graphics Hardware," *Proc. Graphics Hardware*, pp. 265-272, 2003.
- [Pen82] A. P. Pentland, "Finding the Illuminant Direction," *Journal of the Optical Society of America*, Vol. 72, No. 4, pp. 448-455, 1982.
- [RH01a] R. Ramamoorthi and P. Hanrahan, "A Signal Processing Framework for Inverse Rendering," *Proc. ACM SIGGRAPH '01*, pp. 117-128, 2001.
- [RH01b] R. Ramamoorthi and P. Hanrahan, "On the Relationship Between Radiance and Irradiance: Determining the Illumination from Images of a Convex Lambertian Object," *Journal of the Optical Society of America*, Vol. 18, No. 10, pp. 2448-2459, 2001.
- [RH02] R. Ramamoorthi and P. Hanrahan, "Frequency Space Environment Map Rendering," *Proc. ACM SIGGRAPH '02*, pp. 517-526, 2002.
- [RPV93] H. Rushmeier, C. Patterson and A. Veerasamy, "Geometric Simplification for Indirect Illumination Calculations," *Proc. Int. Conf. on Graphics Interface (GI1993)*, pp. 227-236, 1993.

- [SAW91] F. X. Sillion, J. R. Arvo and S. H. Westin, "A Global Illumination Solution for General Reflectance Distributions," *Proc. ACM SIGGRAPH '91*, pp. 187-196, 1991.
- [SCH93] S. J. Gortler and P. Schroder, M. F. Cohen and P. Hanrahan, "Wavelet Radiosity," *Proc. ACM SIGGRAPH '93*, pp. 221-230, 1993.
- [SH81] R. Siegel and J. Howell, *Thermal Radiation Heat Transfer*, 2nd edition, 1981.
- [Shi90] P. Shirley, "A Ray Tracing Method for Illumination Calculation in Diffuse-Specular scene," *Proc. Int. Conf. on Graphics Interface (GI1990)*, pp. 205-212, 1990.
- [Shi91] P. Shirley, "Discrepancy as a Quality Measure for Sample Distributions," *Proc. Eurographics '91*, pp. 183-194, 1991.
- [SS97] R. Szeliski and H. Shum, "Creating Full View Panoramic Image Mosaics and Environment Maps," *Proc. ACM SIGGRAPH '97*, pp. 251-258, 1997.
- [SSI99] I. Sato, Y. Sato and K. Ikeuchi, "Acquiring a Radiance Distribution to Superimpose Virtual Objects onto a Real Scene," *IEEE Trans. on Visualization and Computer Graphics*, Vol. 5, No. 1, pp. 1-12, January 1999.
- [SSI03] I. Sato, Y. Sato and K. Ikeuchi, "Illumination from Shadows," *IEEE Trans. on Pattern Analysis and Machine Intelligence*, Vol. 25, No. 3, pp. 290-300, 2003.
- [SSS00] M. Stamminger, P. Slusallek and H. P. Seidel, "Density Control for Photon Maps," *Proc. Rendering Techniques '00*, pp. 23-34, 2000.
- [SWI97] Y. Sato, Mark D. Wheeler and K. Ikeuchi, "Object Shape and Reflectance Modeling from Observation," *Proc. ACM SIGGRAPH '97*, pp. 379-387, 1997.
- [TS67] K. E. Torrance and E. M. Sparrow, "Theory for Off-specular Reflection from Roughened Surfaces," *Journal of the Optical Society of America*, Vol. 57, No. 9, pp. 1105-1114, 1967.

- [VG95] H. Veach and L. J. Guibas, "Optimally Combining Sampling Techniques for Monte Carlo Rendering," *Proc. ACM SIGGRAPH '95*, pp. 419-428, 1995.
- [VG97] H. Veach and L. J. Guibas, "Metropolis Light Transport," *Proc. ACM SIGGRAPH '97*, pp. 65-76, 1997.
- [War92] G. J. Ward, "Measuring and Modeling Anisotropic Reflection," *Proc. ACM SIGGRAPH '92*, pp. 265-272, July 1992.
- [WCG87] J. R. Wallace, M. F. Cohen and D. P. Greenberg, "A Two-pass Solution to the Rendering Equation: A Synthesis of Ray Tracing and Radiosity Methods," *Proc. ACM SIGGRAPH '87*, pp. 311-320, 1987.
- [WEH89] J. R. Wallace, K. A. Elmquist and E. A. Haines, "A Ray Tracing Algorithm for Progressive Radiosity," *Proc. ACM SIGGRAPH '89*, pp. 315-324, 1989.
- [WF91] P. Whaite and F. P. Ferrie, "Autonomous Exploration: Driven by Uncertainty," *IEEE Trans. on Pattern Analysis and Machine Intelligence*, Vol. 13, No. 7, pp. 635-657, 1991.
- [YDMH99] Y. Yu, P. E. Debevec, J. Malik and T. Hawkins, "Inverse Global Illumination: Recovering Reflectance Models of Real Scenes from Photographs," *Proc. ACM SIGGRAPH '99*, pp. 215-227, August 1999.
- [YL89] N. Yokoya and M. D. Levine, "Range Image Segmentation Based on Differential Geometry: A Hybrid Approach," *IEEE Trans. Pattern Analysis and Machine Intelligence*, Vol. 11, No. 6, pp. 643-649, June 1989.
- [ZS95] K. Zimmerman and P. Shirley, "A Two-pass Realistic Image Synthesis Method for Complex Scenes," *Proc. Eurographics Rendering Workshop*, pp. 284-295, 1995.



# List of Publications

## Journal Papers

1. T. Machida, H. Takemura and N. Yokoya, "Dense Estimation of Surface Reflectance Property by Combining Multiple Illumination Conditions", *Transactions of the Institute of Electronics, Information and Communication Engineers of Japan*, Vol. J84-D-II, No. 8, pp. 1873-1881, Aug. 2001 (in Japanese). (Chapters 2 and 3).
2. B. Okumura, T. Machida and N. Yokoya, "Fast Rendering of Reflections in Non-uniform Surfaces Using a Multi-scale Environment Map", *Transaction of the Institute of Image Information and Television Engineers of Japan*, Vol. 57, No. 10, pp. 1300-1306, Oct. 2003 (in Japanese).
3. H. Fukutomi, T. Machida and N. Yokoya, "Virtual Relighting of a Virtualized Scene by Estimating Surface Reflectance Properties", *Transaction of the Institute of Image Information and Television Engineers of Japan*, Vol. 57, No. 11, pp. 1576-1582, Nov. 2003 (in Japanese). (Chapter 4).
4. K. Yoshikawa, T. Machida, K. Kiyokawa and H. Takemura, "A High Presence Shared Space Communication System Using 2D Background and 3D Avatar", *Transactions of the Institute of Electronics, Information and Communication Engineers*, Vol. E87-D, No. 12, pp. 2532-2539, Dec. 2004.
5. T. Machida, N. Yokoya and H. Takemura, "Surface Reflectance Modeling of Real Objects with Interreflections for Augmented Virtuality", *Color Research and Application* (accepted subject to minor revisions). (Chapters 2 and 4).

6. T. Machida, H. Takemura and N. Yokoya, "Inverse Reflectometry for Real Objects with Diffuse and Specular Interreflections", *Transactions of the Institute of Electronics, Information and Communication Engineers of Japan* (in Japanese). (accepted subject to minor revisions). (Chapter 5).
7. K. Uratani, T. Machida, K. Kiyokawa and H. Takemura, "A Study of Depth Visualization Techniques for Virtual Annotations in Augmented Reality Environments", *Transaction of the Virtual Reality Society of Japan*, (in Japanese). (submitted).

## International Conferences

1. T. Machida, H. Takemura and N. Yokoya, "Dense Estimation of Surface Reflectance Parameters from Registered Range and Color Images by Determining Illumination Conditions", *Proc. SPIE Electronic Imaging*, Vol. 4298, pp. 127-134, Jan. 2001 (Chapters 2 and 3).
2. T. Machida, H. Takemura and N. Yokoya, "Dense Estimation of Surface Reflectance Parameters by Selecting Optimum Illumination Conditions", *Proc. 14th Int. Conf. on Vision Interface 2001 (VI2001)*, pp. 244-251, Jun. 2001 (Chapters 2 and 3).
3. T. Machida and N. Yokoya, "Dense Estimation of Surface Reflectance Properties for Merging into Real Images", *Proc. 5th Asian Conf. on Computer Vision 2001 (ACCV2001)*, Vol. 2, pp. 688-693, Jan. 2002 (Chapters 2 and 3).
4. T. Machida and N. Yokoya, "Virtualizing real objects with surface interreflections", *Proc. IEEE Int. Conf. on Multimedia and Expo (ICME2002)*, Vol. 1, pp. 833-836, Aug. 2002 (Chapters 2 and 4).
5. T. Machida and N. Yokoya, "Dense estimation of surface reflectance properties of objects with interreflections", *Proc. 16th IAPR Int. Conf. on Pattern Recognition (ICPR2002)*, Vol. I, pp. 348-351, Aug. 2002 (Chapters 2 and 4).
6. H. Takemura, M. Maeda, T. Habara, T. Ogawa and T. Machida, "Indoor Localization using IR Markers for Augmented Reality", *Demonstration Booklet of Int.*

*Workshop on Man-Machine Symbiotic Systems (MMS-WS)*, p. 1, Nov. 2002.

7. B. Okumura, T. Machida and N. Yokoya, "Fast Rendering of Reflections in Non-uniform Surfaces Using a Multi-Scale Environment Map", *Proc. ACM SIGGRAPH 2003*, Jul. 2003.
8. T. Machida, N. Yokoya and H. Takemura, "Surface Reflectance Modeling of Real Objects with Interreflections," *Proc. 9th IEEE Int. Conf. on Computer Vision 2003 (ICCV2003)*, Vol. 1, pp. 170-177, Oct. 2003 (Chapters 2 and 4).
9. M. Maeda, T. Ogawa, T. Machida, K. Kiyokawa and H. Takemura, "Indoor Localization and Navigation using IR Markers for Augmented Reality", *Proc. Int. Conf. on Human-Computer Interaction (HCI International 2003)*, pp. 283-284, Jun. 2003.
10. K. Yoshikawa, T. Machida, K. Kiyokawa and H. Takemura, "A High Presence Shared Space Communication System Using 2D Background and 3D Avatar", *Proc. Int. Symp. on Applications and the Internet (SAINT2004)*, pp. 50-55, Jan. 2004 [Best Paper Award].
11. Y. Tomozoe, T. Machida, K. Kiyokawa and H. Takemura, "Unified Gesture-Based Interaction Techniques for Object Manipulation and Navigation in a Large-Scale Virtual Environment", *Proc. IEEE Virtual Reality (IEEE VR 2004)*, Mar. 2004.
12. Y. Tomozoe, T. Machida, K. Kiyokawa and H. Takemura, "A Software Approach to Improve VE Interfaces, Unification of Interaction Techniques for Object Manipulation and Navigation", *Proc. IEEE Workshop on Beyond Wand and Glove Based Interaction*, pp. 101-102, Mar. 2004.
13. T. Machida, H. Takemura and N. Yokoya, "Dense Estimation of Surface Reflectance Properties Based on Inverse Global Illumination Rendering", *Proc. 17th IAPR Int. Conf. on Pattern Recognition (ICPR2004)*, Vol. I, pp. 348-351, Aug. 2004 (Chapters 2 and 5).
14. M. Kanbara, R. Tenmoku, T. Ogawa, T. Machida, M. Koeda, Y. Matsumoto, K. Kiyokawa, H. Takemura, T. Ogasawara and N. Yokoya, "Nara palace site

navigator, A wearable tour guide system based on augmented reality”, *Proc. 3rd CREST/ISWC Workshop on Advanced Computing and Communicating Techniques for Wearable Information Playing*, pp. 7-14, Oct. 2004.

15. K. Nakashima, T. Machida, K. Kiyokawa and H. Takemura, ”A 2D-3D Integrated Environment for Cooperative Work”, *Proc. 14th Int. Conf. on Artificial Reality and Telexistence (ICAT2004)*, pp. 348-351, Nov. 2004.

## Domestic Conferences

1. T. Machida, H. Iwasa, H. Takemura and N. Yokoya, ”Estimation of Reflectance Parameters Using a Rangefinder under Multiple Illumination Conditions”, *Proc. 59th Information Processing Society of Japan, General Conference*, No. 2ZC-8, Sep. 1999 (in Japanese). (Chapters 2 and 3).
2. T. Machida, H. Iwasa, H. Takemura and N. Yokoya, ”Estimation of Reflectance Parameters Using Panoramic Range and Intensity Images under Multiple Illumination Conditions”, *Technical Report of the Institute of Electronics, Information and Communication Engineers of Japan, Pattern Recognition and Media Understanding (PRMU)*, PRMU99-162, Nov. 1999 (in Japanese). (Chapters 2 and 3).
3. K. Nakakita, T. Machida, H. Takemura and N. Yokoya, ”Presentation of Video Avatars Based on Following User’s Position Using Active Cameras”, *Technical Report of the Institute of Electronics, Information and Communication Engineers of Japan, Image Engineering (IE)*, IE2000-160, Jan. 2000 (in Japanese).
4. T. Machida, H. Iwasa, H. Takemura and N. Yokoya, ”Estimation of Reflectance Property with Considering the Self-Shadow”, *Proc. the 2000 Institute of Electronics, Information and Communication Engineers, General Conference*, No. D-12-176, Mar. 2000 (in Japanese). (Chapters 2 and 3).
5. T. Machida, H. Iwasa, H. Takemura and N. Yokoya, ”Estimation of Surface Reflectance Property by Combining 3D Rangefinder and Multiple Illumination Conditions”, *Proc. Meeting on Image Recognition and Understanding (MIRU2000)*, Vol. I, pp. 113-118, Jul. 2000 (in Japanese). (Chapters 2 and 3).

6. T. Machida, H. Takemura and N. Yokoya, "Estimation of Object Surface Reflectance Properties Using Multiple Illumination Conditions", *Proc. the 2000 Kansai-section Joint Convention of Institutes of Electrical Engineering of Japan*, No. G15-23, Aug. 2000 (in Japanese). (Chapters 2 and 3).
7. K. Nakakita, T. Machida, H. Takemura and N. Yokoya, "A Video Avatar Presentation for Cooperative-Work in a Shared Virtual Environment", *Proc. the 2000 Institute of Electronics, Information and Communication Engineers, Society Conference*, No. D-16-7, Sep. 2000 (in Japanese).
8. T. Machida and N. Yokoya, "Estimation of Object Surface Reflectance Properties with Considering Interreflection Based on Radiosity", *Proc. the 6th Virtual Reality Society of Japan, Annual Conference*, pp. 455-456, Sep. 2001 (in Japanese). (Chapters 2 and 4).
9. S. Kawano, T. Machida, K. Yamazawa and N. Yokoya, "An Interactive Creation of Human Animation by Combining Multiple Motion Data", *Proc. the 6th Virtual Reality Society of Japan, Annual Conference*, pp. 13-14, Sep. 2001 (in Japanese).
10. T. Machida and N. Yokoya, "Estimation of Object Surface Reflectance Properties Considering Interreflections", *Technical Report of the Institute of Electronics, Information and Communication Engineers of Japan, Multimedia and Virtual Environment (MVE)*, MVE2001-67, Oct. 2001 (in Japanese). (Chapters 2 and 4).
11. T. Machida and N. Yokoya, "Estimation of Object Surface Reflectance Properties with Interreflections", *Technical Report of the Institute of Electronics, Information and Communication Engineers of Japan, Pattern Recognition and Media Understanding (PRMU)*, PRMU2001-225, Feb. 2002 (in Japanese). (Chapters 2 and 4).
12. T. Habara, T. Machida, T. Ogawa and H. Takemura, "Evaluation of Indoors Position Detection Using Fiducial Markers", *Technical Report of the Institute of Electronics, Information and Communication Engineers of Japan, Image Engineering (IE)*, Vol. 102, No. 216, pp. 65-70, Jul. 2002 (in Japanese).

13. M. Maeda, T. Ogawa, T. Machida and H. Takemura, "Position Detection for a Navigation Support by Augmented Reality Using Infrared Identifications", *Technical Report of the Institute of Electronics, Information and Communication Engineers of Japan, Image Engineering (IE)*, Vol. 102, No. 216, pp. 59-64, Jul. 2002 (in Japanese).
14. B. Okumura, T. Machida and N. Yokoya, "A Real-Time Rendering Technique for Non-uniform Roughness Surfaces Using a Multi-Scale Environment Map", *Proc. the 7th Virtual Reality Society of Japan, Annual Conference*, pp. 381-382, Sep. 2002 (in Japanese).
15. H. Fukutomi, T. Machida and N. Yokoya, "Interactive Virtual Relighting of a Real Scene with Diffuse and Specular Surfaces", *Proc. the 7th Virtual Reality Society of Japan, Annual Conference*, pp. 375-376, Sep. 2002 (in Japanese). (Chapter 4).
16. S. Li, T. Machida and H. Takemura, "An IBR Method for Novel Viewpoint Image Synthesis Using Fractal Image Coding", *Proc. the 7th Virtual Reality Society of Japan, Annual Conference*, pp. 421-422, Sep. 2002 (in Japanese).
17. T. Habara, T. Machida, K. Kiyokawa and H. Takemura, "Indoors Position Detection Using Fiducial Marker for Wearable PC", *Proc. the 7th Virtual Reality Society of Japan, Annual Conference*, pp. 335-336, Sep. 2002 (in Japanese).
18. M. Maeda, T. Ogawa, T. Machida and H. Takemura, "Position Detection for a Wearable System Using Infrared Identifications", *Proc. the 7th Virtual Reality Society of Japan, Annual Conference*, pp. 333-334, Sep. 2002 (in Japanese).
19. T. Machida and N. Yokoya, "Estimation of Surface Reflectance Properties with Interreflections based on Radiosity", *Proc. Forum on Information Technology (FIT2002)*, Vol. 3, No. I-25, Sep. 2002 (in Japanese). (Chapters 2 and 4).
20. B. Okumura, T. Machida and N. Yokoya, "A Real-Time Rendering Technique for Non-uniform Surfaces Using a Multi-Scale Environment Map of a Real Scene", *Technical Report of the Institute of Electronics, Information and Communication Engineers of Japan, Pattern Recognition and Media Understanding (PRMU)*, PRMU2002-137, Dec. 2002 (in Japanese).

21. H. Fukutomi, T. Machida and N. Yokoya, "Virtualizing of a Real Scene for Interactive Virtual Relighting", *Technical Report of the Institute of Electronics, Information and Communication Engineers of Japan, Pattern Recognition and Media Understanding (PRMU)*, PRMU2002-136, Dec. 2002 (in Japanese). (Chapter 4).
22. K. Uratani, T. Machida, K. Kiyokawa and H. Takemura, "Displaying Annotations in Consideration of Depth Information", *Proc. the 2003 Institute of Electronics, Information and Communication Engineers, General Conference*, p. 304, Mar. 2003 (in Japanese).
23. K. Nakashima, T. Machida, K. Kiyokawa and H. Takemura, "A Cooperative Work Environment with Projection Images to an IllusionHole Mask", *Proc. the 2003 Institute of Electronics, Information and Communication Engineers, General Conference*, p. 310, Mar. 2003 (in Japanese).
24. T. Habara, T. Machida, K. Kiyokawa and H. Takemura, "Evaluation of Indoor Position Detection for Wearable PC Using Fiducial Markers", *Proc. 63th Information Processing Society of Japan, General Conference*, Vol. 5, pp. 199-202, Mar. 2003 (in Japanese).
25. K. Yamamoto, T. Machida, K. Kiyokawa and H. Takemura, "A Method of Polygon Conversion from Voxel Data", *Proc. the 2003 Institute of Electronics, Information and Communication Engineers, General Conference*, p. 302, Mar. 2003 (in Japanese).
26. K. Yoshikawa, T. Machida, K. Kiyokawa and H. Takemura, "High Presence Shared Space Communication Using 2D Background and 3D Avatar", *Technical Report of the Institute of Electronics, Information and Communication Engineers of Japan, Image Engineering (IE)*, IE2003-24, Jul. 2003 (in Japanese).
27. Y. Tomozoe, T. Machida, K. Kiyokawa and H. Takemura, "Unified Gesture Commands for Manipulation of Remote Virtual Objects and Navigation in a Large Scale Virtual Space", *Technical Report of the Institute of Electronics, Information and Communication Engineers of Japan, Image Engineering (IE)*, IE2003-39, Jul. 2003 (in Japanese).

28. K. Uratani, T. Machida, K. Kiyokawa and H. Takemura, "Evaluation for Virtualizing Depth Information of Annotations in Augmented Reality Environment", *Technical Report of the Institute of Electronics, Information and Communication Engineers of Japan, Image Engineering (IE)*, IE2003-40, Jul. 2003 (in Japanese).
29. K. Nakashima, T. Machida, K. Kiyokawa and H. Takemura, "An Integrated 2D and 3D Environment for Multi-User Cooperative Modeling", *Proc. the 8th Virtual Reality Society of Japan, Annual Conference*, pp. 513-514, Sep. 2003 (in Japanese).
30. K. Yoshikawa, T. Machida, K. Kiyokawa, H. Takemura and Hiroyuki Ohno, "High Presence Shared Space Communication Using Low Resolution Rangefinder and High Resolution Camera", *Technical Report of the Institute of Electronics, Information and Communication Engineers of Japan, Pattern Recognition and Media Understanding (PRMU)*, PRMU2003-197, Jan. 2004 (in Japanese).
31. K. Uratani, T. Machida, K. Kiyokawa and H. Takemura, "Evaluation for Virtualizing Depth Information of Annotations in Augmented Reality Environment", *Technical Report of the Institute of Electronics, Information and Communication Engineers of Japan, Intelligent Transport System (ITS)*, ITS2003-57, Feb. 2004 (in Japanese).
32. Y. Tomozoe, T. Machida, K. Kiyokawa and H. Takemura, "Unified Gesture-based Interaction Techniques for Manipulation of Remote Virtual Objects and Navigation", *Technical Report of the Institute of Electronics, Information and Communication Engineers of Japan, Intelligent Transport System (ITS)*, ITS2003-55, Feb. 2004 (in Japanese).
33. K. Nakashima, T. Machida, K. Kiyokawa and H. Takemura, "An Integrated 2D-3D Work Environment for Cooperative Modeling", *Technical Report of the Institute of Electronics, Information and Communication Engineers of Japan, Intelligent Transport System (ITS)*, ITS2003-56, Feb. 2004 (in Japanese).
34. T. Habara, T. Machida, K. Kiyokawa and H. Takemura, "Wide-Area Indoor Position Detection using Fiducial Markers for Wearable PC", *Technical Report of*

*the Institute of Electronics, Information and Communication Engineers of Japan, Intelligent Transport System (ITS), ITS2003-76, Feb. 2004 (in Japanese).*

35. D. Takada, T. Machida, K. Kiyokawa and H. Takemura, "A Development Toolkit for a Shared Wearable AR System", *Proc. the 2004 Institute of Electronics, Information and Communication Engineers, General Conference*, p. 345, Mar. 2004 (in Japanese).
36. T. Machida, N. Yokoya and H. Takemura, "Estimation of Surface Reflectance Properties of Real Objects with Interreflections for Augmented Virtuality", *Proc. Meeting on Image Recognition and Understanding (MIRU2004)*, Vol. I, pp. 113-118, Jul. 2004 [Best Paper Award] (in Japanese). (Chapters 2 and 5).
37. D. Takada, K. Uratani, T. Machida, K. Kiyokawa and H. Takemura, "Construction of a Development Toolkit for a Shared Wearable AR System", *Proc. the 9th Virtual Reality Society of Japan, Annual Conference*, pp. 333-334, Sep. 2004 (in Japanese).
38. S. Li, T. Machida and H. Takemura, "Object Shape and Reflectance Modeling from a Sparse Set of Images", *Technical Report of the Institute of Image Electronics Engineers of Japan*, pp. 57-62, Nov. 2004.

## **Awards**

1. Scientific Incentive Award of the 2000 Kansai-section Joint Convention of the Institutes of Electrical Engineering of Japan, 2001.
2. TELECOM System Technology Award for Student of the Telecommunications Advancement Foundation, 2002.
3. Best Paper Award of Meeting on Image Recognition and Understanding (MIRU2004), 2004.